Tectonic and Climatic controls on the Growth and Shape of the Himalayan Foreland Fold-and-Thrust Belt: A Numerical Study

Deirdre Mallyon

Dalhousie University, Halifax, Nova Scotia, Canada, B3H 2J1

Submitted in Partial Fulfillment of the Requirements for the Degree of Bachelor of Science, Honours, Department of Earth Science, Dalhousie University, Halifax, Nova Scotia, B3H 2J1

March 17, 2014

Distribution License

DalSpace requires agreement to this non-exclusive distribution license before your item can appear on DalSpace.

NON-EXCLUSIVE DISTRIBUTION LICENSE

You (the author(s) or copyright owner) grant to Dalhousie University the non-exclusive right to reproduce and distribute your submission worldwide in any medium.

You agree that Dalhousie University may, without changing the content, reformat the submission for the purpose of preservation.

You also agree that Dalhousie University may keep more than one copy of this submission for purposes of security, back-up and preservation.

You agree that the submission is your original work, and that you have the right to grant the rights contained in this license. You also agree that your submission does not, to the best of your knowledge, infringe upon anyone's copyright.

If the submission contains material for which you do not hold copyright, you agree that you have obtained the unrestricted permission of the copyright owner to grant Dalhousie University the rights required by this license, and that such third-party owned material is clearly identified and acknowledged within the text or content of the submission.

If the submission is based upon work that has been sponsored or supported by an agency or organization other than Dalhousie University, you assert that you have fulfilled any right of review or other obligations required by such contract or agreement.

Dalhousie University will clearly identify your name(s) as the author(s) or owner(s) of the submission, and will not make any alteration to the content of the files that you have submitted.

If you have questions regarding this license please contact the repository manager at dalspace@dal.ca.

Grant the distribution license by signing and dating below.

_____ _____

Name of signatory Date

DALHOUSIE UNIVERSITY
Inspiring Minds

Department of Earth Sciences
Halifax, Nova Scotia
Canada B3H 4R2
(902) 494-2358
FAX (902) 494-6889

DATE: April 29 /2014

AUTHOR: Deirdre Mallyon

TITLE: Tectonic and climatic controls on growth and shape of the Himalayan foreland fold-and-thrust belt: A numerical study

Degree: BSc Convocation: _____ Year: 2014

[redacted]
Signature of Author

Abstract

According to the critical taper model, there are three processes that determine the morphology of foreland fold-and-thrust belts: 1) the removal of material by erosion, 2) the accretion of material, determined by sedimentation and plate convergence rates, and 3) steady-state critical growth, determined by the mechanical properties of the materials that comprise the wedge. The Himalayan orogen provides a unique opportunity to study collisional orogens and active fold-and-thrust belts (FTB) in an environment where processes 1 and 2 (above) vary systematically along strike. The Siwalik Group consists of synorogenic sediments of Miocene to Pleistocene age, and constitutes the presently active foreland FTB of the Himalayan orogen. Recently constructed balanced cross-sections have revealed two important observations concerning foreland FTB morphology across the Himalayan arc: 1) west to east increase in strain and strain rate correlates with plate convergence rates, and 2) annual rainfall amounts are inversely correlated with FTB morphology. From these observations, it was proposed that surface processes exert greater control on wedge morphology than tectonic processes in the Himalayan FTB. In this study, the critical taper model is used to test the relative contribution of surface processes to the morphology of the present-day foreland FTB of the Himalaya. Internal parameters such as; friction, both along the wedge (μ) and décollement fault plane (μ_b); the Hubbert-Rubey pore fluid ratio, both within the wedge (λ) and along the basal décollement (λ_b); and the critical taper ($\alpha+\beta$) were held constant. Key parameters including: thickness of accreted foreland material (T), depth at which the décollement flattens (D), rock erodibility (K) and material flux into the wedge (vT) were varied within the range of observed values along-strike of the Himalayan FTB. Comparisons between experiments allow estimation of model sensitivity to each parameter individually. The calculated critical taper morphology and growth rate are consistent with those observed in the Himalayan FTB, indicating that the FTB developed in accordance with critical Coulomb wedge theory. Comparative analysis indicates that within a narrow range of parameters and high values of the erodibility factor K ($1\times10^{-5}\leq K \leq 1\times10^{-4}$), climatically induced erosion is the principal control on Himalayan foreland FTB morphology. Conversely, when the erodibility factor (K) is low, tectonic accretion of the material (vT) is the dominant parameter in controlling FTB morphology.

Key Words: critical taper, steady-state, FTB, surface processes, tectonic processes, critical Coulomb wedge

Table of Contents

Table of Figures

Table of Tables

Table of Abbreviations and Notation

Abbreviations

CCW	Critical Coulomb Wedge
FTB	Fold-and-Thrust
GHS	Greater Himalayan Sequence
ISM	Indian Summer Monsoon
ITSZ	Indus-Tzangpo Suture Zone
LHS	Lesser Himalayan Sequence
MBT	Main Boundary Thrust
MCT	Main Central Thrust
MFT	Main Frontal Thrust
MHT	Main Himalayan Thrust
SG	Siwalik Group
SHS	Sub Himalayan Sequence
STDS	South Tibetan Detachment System

Notation

α	Surface slope of the wedge (with respect to horizontal)
β	Angle of the decollement (with respect to horizontal)
λ	Hubbert-Rubey pore fluid pressure ratio within the wedge
λ_b	Hubbert-Rubey pore fluid pressure ratio along the decollement
μ	Coefficient of friction within the wedge
μ_b	Coefficient of friction along the decollement
D	Sole-out depth (units: L)
$\dot{e}$	Erosion rate (units: L/t)

h	Exponent in area-length relationship (reciprocal of Hack's exponent)
k_a	Area-length coefficient (units: L^{2-h})
K	Coefficient of erosion (units: L^{1-2m}/t)
m	Erosion rule area exponent
n	Erosion rule slope exponent
T	Thickness of material accreted from the foreland (units: L)
t	Time
v	Convergence velocity (units: L/t)

Acknowledgements

First and foremost, I would like to thank my supervisor Dr. Djordje Grujic, for giving me the opportunity to work on this fascinating project. It has been an absolute honour to work with you this year, I have learned more from you in eight months than I would have ever thought possible, and for that I am sincerely grateful. I want to thank you for your invaluable guidance and patience throughout the year, I could not have completed this project without you. Second I would like to thank Dr. George Hilley for supplying the necessary MatLab script, and also for his assistance throughout the course of the project. Third I would like to thank Dr. Martin Gibling for his abundant support and feedback throughout the term, I am truly in your debt. Lastly, I would like to thank the faculty, staff, and students of the Earth Science Department, I am honoured to have spent the last four years with you; you have made my experience at Dalhousie one I will cherish for a lifetime.

1.0 Introduction

Mountain belts are formed by interactions and feedbacks between tectonics and surface processes (Beaumont et al., 1992; Willett et al., 1993; Whipple, 2009) affecting crustal deformation. Since upper crustal deformation can be directly observed in active orogens and parameters controlling the deformation and morphology of a frictional tectonic wedge have been well established, this study will concentrate on the present-day foreland fold-and-thrust belt (FTB) of the Himalayan orogen to determine the relative contribution of surface processes to FTB morphology (Avouac, 2003).

There are three primary processes that control the geometry of a foreland fold-and-thrust belt (Dahlen, 1984; Whipple and Tucker, 1999; Hilley and Strecker, 2004; Hilley et al., 2004; Whipple, 2009): (1) steady-state critical growth, determined by the mechanical properties of the wedge; (2) the rate of frontal accretion, which depends on sedimentation and convergence velocity; (3) removal of material by erosion. Because the lithology which comprises the Himalayan FTB does not vary along the strike of the Himalayan arc, its mechanical properties can be considered nearly constant. Furthermore, India-Eurasia convergence rate has been steady during the development of the FTB. Conversely, it has been shown that the shortening rates across the FTB, and the annual rainfall amounts over the FTB, change systematically along the strike of the arc (Banerjee et al., 2008; Molnar and Stock, 2009; Burgess et al., 2012).

The steady-state width of a uniformly eroding critical Coulomb wedge (CCW) was defined by Dahlen (1990) as $\dot{e}W\sec(\alpha+\beta) \approx \dot{e}W = vT$ where $\dot{e}$ is the rate of erosion, W is the wedge width, α is the surface slope of the wedge, β is the dip of the basal décollement, T is the thickness of accreted material and v is the convergence velocity. From this definition it is apparent that

increased material flux (*vT*) into the wedge will result in a larger wedge, and thus greater surface slopes are required to remove the larger volume of material. The third process, material flux out of the wedge, may greatly affect the geometry of orogenic wedges (Dahlen and Barr, 1989). Erosion rates are controlled by the erodibility of the material as well as erosional surface processes, such as mean annual precipitation. In climates with low mean annual precipitation, steeper surface slopes are required to increase erosional efficiency. This implies that, if all other properties are fixed, critical Coulomb wedges in more arid climates will be wider than wedges located in regions that receive greater amounts of precipitation (Dahlen and Barr, 1989). In the Himalaya, the Indian Summer Monsoon (ISM) accounts for more than 80% of the mean annual rainfall (Bookhagen and Burbank, 2010). However, the mean annual rainfall received locally shows across- and along-strike variations, resulting in variable rates of sediment transport to, and erosion from, the Himalayan wedge (Bookhagen and Burbank, 2010; Hirschmiller et al., 2014).

A recent study in the Himalayan region showed a west to east variation in strain rate, shortening rate, and shortening amount (Hirschmiller et al., 2014). A correlation between FTB width and annual precipitation was observed, whereas an inverse correlation exists between FTB width and strain rate (Hirschmiller et al., 2014).The objectives of this research project are to quantify FTB geometry along the Himalaya in terms of spatial-temporal variations of erosion and convergence rates, in order to determine which of these parameters is exerting greater control on the regional morphology of the present-day Himalayan foreland FTB.

Following the approach developed by Hilley et al. (2004) and Hilley and Strecker (2004), realistic erosion models will be used in combination with simple kinematic models of wedge growth to evaluate the sensitivity of Himalayan wedge geometry to fluctuations in erosion rates and material accretion. This study differs from the results of Hilley and Strecker (2004) in two

important respects. First, the extent of the Himalayan critical Coulomb wedge will be limited to the active Himalayan foreland FTB (i.e. the Siwalik Group), as opposed to extending from the Main Frontal Thrust (MFT) to the suture zone (Hilley and Strecker, 2004). Second, wedge morphology and deformation parameters will be sytematically varied along- and across-strike of the foreland FTB, rather than assuming a narrow range of parameters to be representative of the entire orogenic wedge. These distinctions are important because the goal of the present study is to test the affects of local variations in erosion rate and convergence rate on FTB morphology, along-strike of the Himalayan arc. The model used in this study can also be applied to other orogenic wedges where steady-state critical Coulomb wedge growth can be demonstrated.

2.0 Geologic Setting and Theoretical Background

The following chapter presents the regional geology of the Himalayan orogen and the present-day Himalayan FTB, and concludes with a discussion of CCW theory. The former section will highlight the main tectonostratigraphic sequences within the Himalayan orogen and the major structural boundaries between them, as well as a detailed description of the Siwalik Group (i.e. the present-day Himalayan FTB). The latter section will describe the theoretical background of CCW theory and the mechanics of orogenic wedges, as well as the method for calculating the critical taper angle of a CCW.

2.1 Regional Geology

The formation of the Himalayan orogen began approximately 55 Ma, as a result of the closing of the Tethys Ocean and the collision of the Indian and Eurasian plates (Najman et al., 2004, and references therein). During convergence, sediments accumulated along the northern margin of the Indian Plate from the Early Proterozoic to the Eocene were detached from the basement of the Indian Plate along a décollement (Decelles, 1999). These detached sediments were deformed in different tectonic styles at upper and middle crustal levels. Consequently, the Himalayan mountain belt has been divided into four tectonostratigraphic sequences (Figure 2.1B); from south to north these are: (1) the Sub-Himalayan Sequence (SHS), (2) the Lesser Himalayan Sequence (LHS), (3) the Greater Himalayan Sequence (GHS), and (4) the Tethyan Himalayan Sequence (THS) (Gansser, 1964; Hodges, 2000). These sequences differ in lithologic, stratigraphic, tectonic, and metamorphic styles, and are structurally separated from one another by

normal and thrust geometry ductile shear zones as well as brittle faults (Gansser, 1964; Hodges

A)

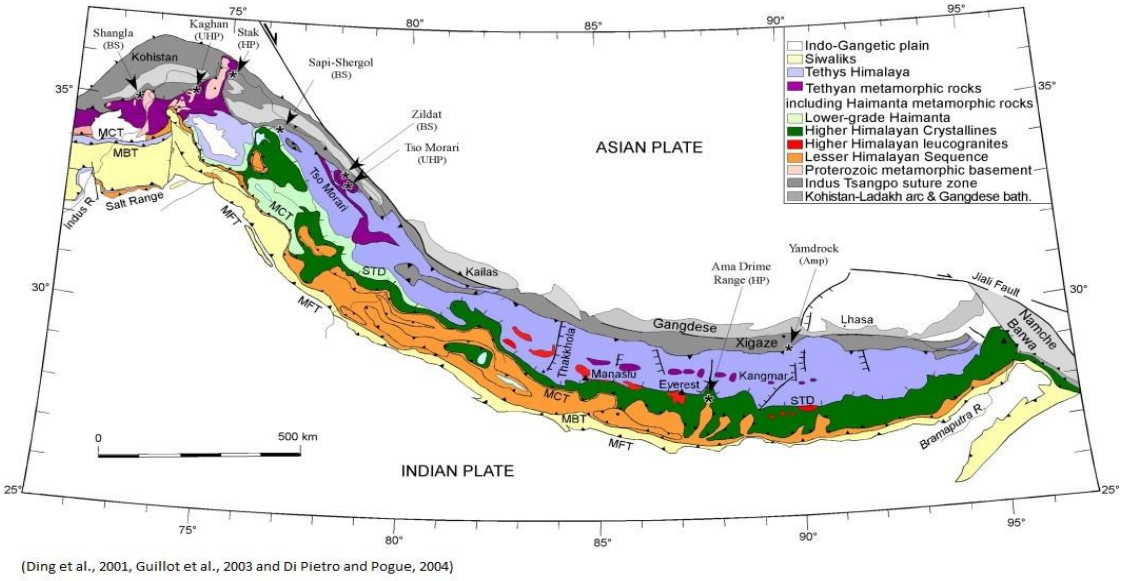

(Ding et al., 2001, Guillot et al., 2003 and Di Pietro and Pogue, 2004)

B)

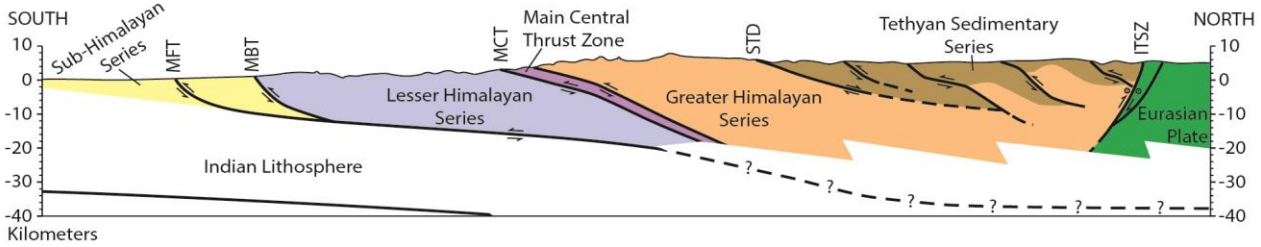

Figure 2.1: A) Geologic map of the Himalayas showing lithological units and major faults. The Siwalik Group is shown in light yellow .B) Cross-section through the Himalayan orogen showing the major tectonostratigraphic sequences and major structural boundaries. Image from Hauck (1998), Lave and Avouac (2001) and Jessup (2013).

2000).

The Main Frontal Thrust (MFT) separates the alluvial sediments of the present-day Himalayan foreland basin from the SHS, the Main Boundary Thrust (MBT) separates the SHS and the LHS, the Main Central Thrust (MCT) separates the LHS and the GHS, and the South Tibetan Detachment System (STDS) separates the GHS from the THS (Figure 2.1). The MFT, MBT and MCT are sub-parallel, with top-to-the south thrust geometry and low dip angles. The MFT and MBT are both brittle fault zones. Searle et al. (2008) defined the MCT as the base of a large-scale

zone of high strain and ductile deformation, corresponding to the base of the inverted metamorphic field gradient observed within the GHS. The MCT places the high-grade metamorphic rocks of the GHS over the low-grade metamorphic rocks of the LHS (Searle et al., 2008). The MFT, MBT and MCT all stem from the Main Himalayan Thrust (MHT), which is the Himalayan basal décollement (Nelson et al., 1996). The STDS is a system of low-angle normal faults and ductile shear zones that have a top-to-the north normal kinematic sense (Kellett and Grujic, 2012).

The SHS is located in the frontal part of the Himalayan range (Mugnier et al., 1999a) and consists of Middle- Miocene to Pleistocene foreland basin sediments (DeCelles et al., 2001). This sequence is bounded to the south by the currently active MFT and to the north by the MBT, with the LHS in the hanging wall (Ojha et al., 2009). The SHS consists primarily of the Siwalik Group (SG), an up to 2500 m thick sequence of upward coarsening sedimentary rocks, dominated by fluvial siltstone, sandstone, and conglomerate (DeCelles et al., 2001; Najman 2006). The SG is discussed in greater detail in Section 2.2.

The LHS is bounded to the south by the MBT, which was active during the Middle to Late Miocene (Robinson et al., 2001), and to the north by the MCT. The LHS consists of greenschist facies sedimentary rocks (DeCelles et al., 2001) of Early Proterozoic to Miocene age (Robinson et al., 2001; Long et al., 2011a). The lower portion of the LHS mainly consists of siliciclastic meta-sediment, while the upper portion contains both siliciclastic and carbonate sediment (DeCelles et al. 2001; Long et al., 2011a). The thickness of the LHS shows along-strike variation, ranging from 8 to 19 km (Hodges, 2000).

The GHS forms the metamorphic core of the Himalayan orogen. It consists of Middle Proterozoic to Ordovician meta-sedimentary and meta-igneous rocks, metamorphosed under amphibolite to granulite facies conditions and intruded by Miocene leucogranites (Long et al,

2011a; Hodges, 2000; Warren et al., 2011). The GHS is bounded to the south by the MCT and to the north by the STDS. The latter forms the boundary between the unmetamorphosed sediments of the THS and the high-grade metamorphic rocks of the GHS (Kellett and Grujic, 2012 and references therein).

The THS consists of unmetamorphosed sedimentary to low-grade metasedimentary rocks (Garzanti,1999), including sandstone, limestone, and slates to phyllites, deposited on the northern Indian continental margin. The sediments of the Cretaceous- Eocene syncollisional sequence mark the beginning of the continental collision between India and Eurasia (Hodges, 2000). The THS is bounded to the south by the STDS and to the north by the Indus-Tsangpo suture zone (ITSZ) (Hodges, 2000).

2.2 The Present-Day Himalayan Foreland Fold-and-Thrust Belt

The approach used to model the Himalayan FTB in this study differs from that previously undertaken by Hilley and Strecker (2004) because the extent of the Himalayan critical Coulomb wedge is limited to the actively deforming Himalayan foreland FTB (i.e. the Siwalik Group), as opposed to extending from the MFT to the ITSZ. This distinction is important because a CCW and an orogenic wedge are not synonymous. The critical taper angle of an accretionary wedge is achieved through continuous brittle frictional deformation; the state of stress at all points within a critically tapered wedge must be on the verge of Coulomb failure (Dahlen, 1990). The requirement for brittle frictional deformation is a crucial component in using CCW theory to model accretionary wedges, and is the basis for making an important distinction between the Himalayan orogenic wedge and the Himalayan foreland FTB (Davis et al., 1983; Dahlen et al., 1984; Dahlen, 1990). The scope of the model used in the present study is restricted to the latter, and thus define

the Himalayan foreland FTB as the actively deforming rocks of the SG, bounded to the south by the MFT and to the north by the MBT, which forms the rigid backstop to the wedge (Figure 2.2).

2.2.1 Stratigraphy, Sedimentology and Depositional Environment of the Siwalik Group

The SG consists of synorogenic sediments deposited in the Himalayan foreland basin from the Middle Miocene to the Pleistocene (Long et al., 2011a; Najman 2006; DeCelles et al 1998). Sediments of the SG consist of interbedded fluvial siltstone and sandstone with local conglomerate (Acharyya, 1994). These sediments are approximately uniform in type and facies across the Himalayan Arc, although there is some across-strike variation in thickness and depositional

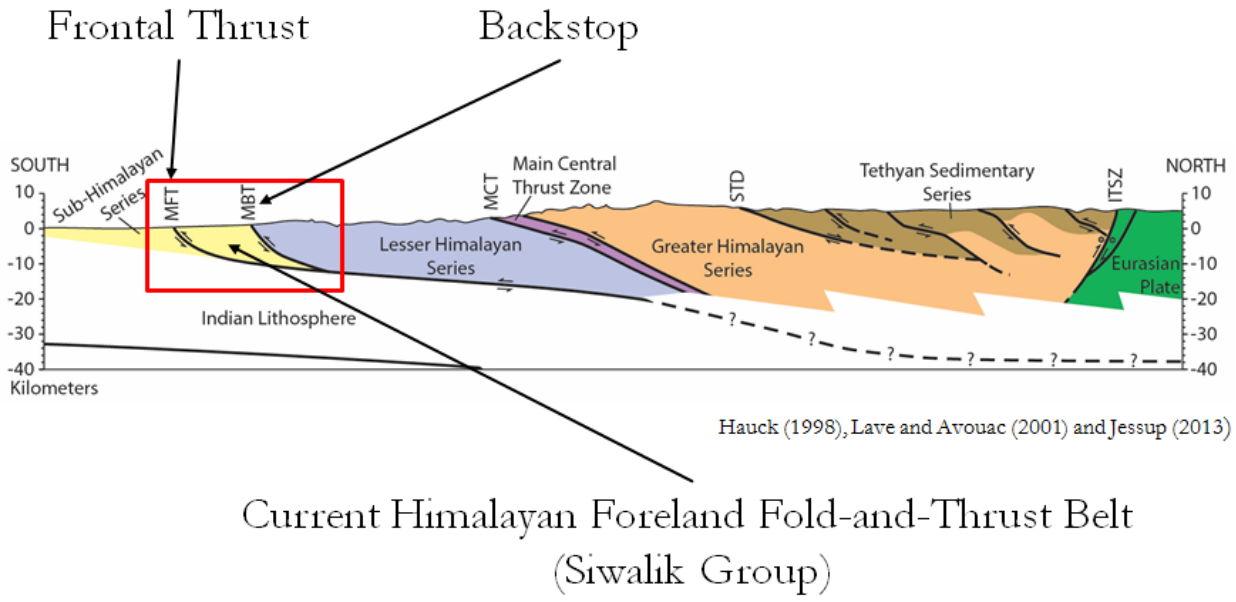

Figure 2.2 Cross-section of the Himalayan orogen, showing the Himalayan foreland FTB, which consists of the Siwalik Group, bounded to the south by the MFT and to the north by the MBT.

environments. Nakayama and Ulak (1999) identified five stages of fluvial evolution within the SG. Stage 1 is characterized by mudstones and very fine- to medium-grained sandstones, deposited in a meandering river system beginning around 15 Ma. Stage 2 is dominated by flood-flow and crevasse-splay systems, beginning around 10.5-9.5 Ma, and is contemporaneous with the onset of monsoon development which began around 10.5 Ma and was completely developed by 7.0 Ma.

Thus, stage 2 is probably climatically controlled. Stage 3 is characterized by the development of braided river systems between 9.0 and 6.5 Ma, probably as a result of regional tectonic uplift of the foreland and monsoon climate development. Stage 4 is characterized by a gravelly braided river system developed between 3.0 and 2.5 Ma, while stage 5 is dominated by debris flow deposits and began at approximately 1 Ma. Stages 4 and 5 are interpreted as tectonically controlled, resulting from thrusting along the MBT. Nakayama and Ulak (1999) noted that the evolution of fluvial style within the SG is reflected in its upward-coarsening sedimentary succession resulting from tectonic uplift of the Himalaya.

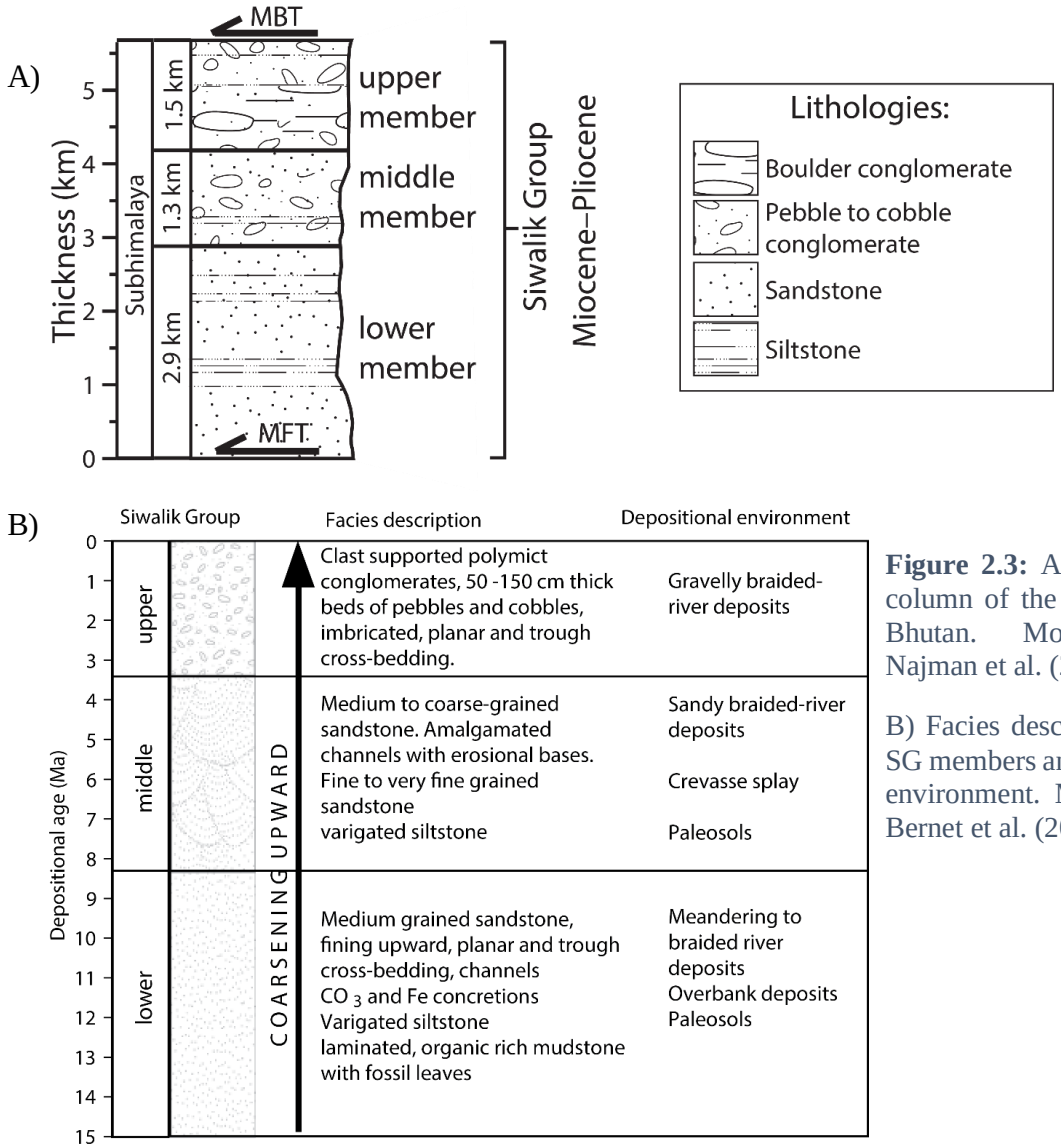

Figure 2.3: A) Stratigraphic column of the SG in eastern Bhutan. Modified from Najman et al. (2006).

B) Facies descriptions of the SG members and depositional environment. Modified from Bernet et al. (2006).

The SG has been broadly subdivided into *Lower*, *Middle* and *Upper* members (Auden, 1935). The *Lower Siwalik Member* is the most distal member relative to the Himalayan front, and consists of grey, blue and brown siltstone and shale interbedded with fine-grained sandstone with calcite concretions (Acharyya, 1994) and calcic paleosols (Ojha, 2009). The transition between the *Lower* and *Middle Siwalik Member* is conformable, and the latter member is composed of medium- to coarse-grained sandstone interbedded with siltstone and mudstone, with minor amounts of pebble conglomerate (Acharyya, 1994). The *Upper Siwalik Member* sits unconformably on top of the *Middle Siwalik Member* (Mugnier et al., 1999b) and is composed of medium to coarse-grained sandstone and conglomerate interbedded with minor amounts of siltstone (Acharyya, 1994).

The depositional age of the SG sediments was determined using magneto-stratigraphy in Nepal by Ojha et al. (2009) and in India by Chirouze et al. (2012). In Nepal, this method yielded ages ranging between 10.5 to 8 Ma for the boundary between the *Lower* and *Middle* members, whereas the boundary between the *Middle* and *Upper* members was dated between 4.6 and 3 Ma (Ojha et al., 2009). In India, this method yields an overall depositional age of between 13 and 2.5 Ma for the SG, 10.5 Ma for the boundary between the *Lower* and *Middle* SG, and 2.6 Ma for the boundary between the *Middle* and *Upper* SG (Chirouze et al., 2012).

2.2.2 Structures Within and Bounding the Siwalik Group

The SG, the deformed portion of the Himalayan foreland basin, is situated between the MFT and the MBT (Mugnier et al., 1999b; Ojha et al., 2009) (Figure 2.4B). Both the MFT and MBT are splays of the MHT. The MHT is located at the footwall of the *Lower* SG, which has a depositional age of 13 Ma in far western Nepal and 14.6 Ma in mid-western Nepal (Mugnier et al., 1999b). A system of northward-dipping thrusts, referred to as the Main Dun Thrusts (MDT), occur within the SG between the MFT and the MBT. The MDTs do not penetrate all of the SG, but either

dwindle into folds that propagate laterally or branch off into lateral transfer zones (Mugnier et al., 1999b). Mugnier et al. (1999a) identified a total of ten major thrusts within the SG in western Nepal; seven of these dip northward whereas the other three are back thrusts and dip southward (Figure 2.4A). Collectively, these thrust faults define thrust sheets within the SG, which have undergone displacement perpendicular to the trend of the FTB in Western Nepal since ~1.8 Ma (Mugnier et al., 1999a).

A)

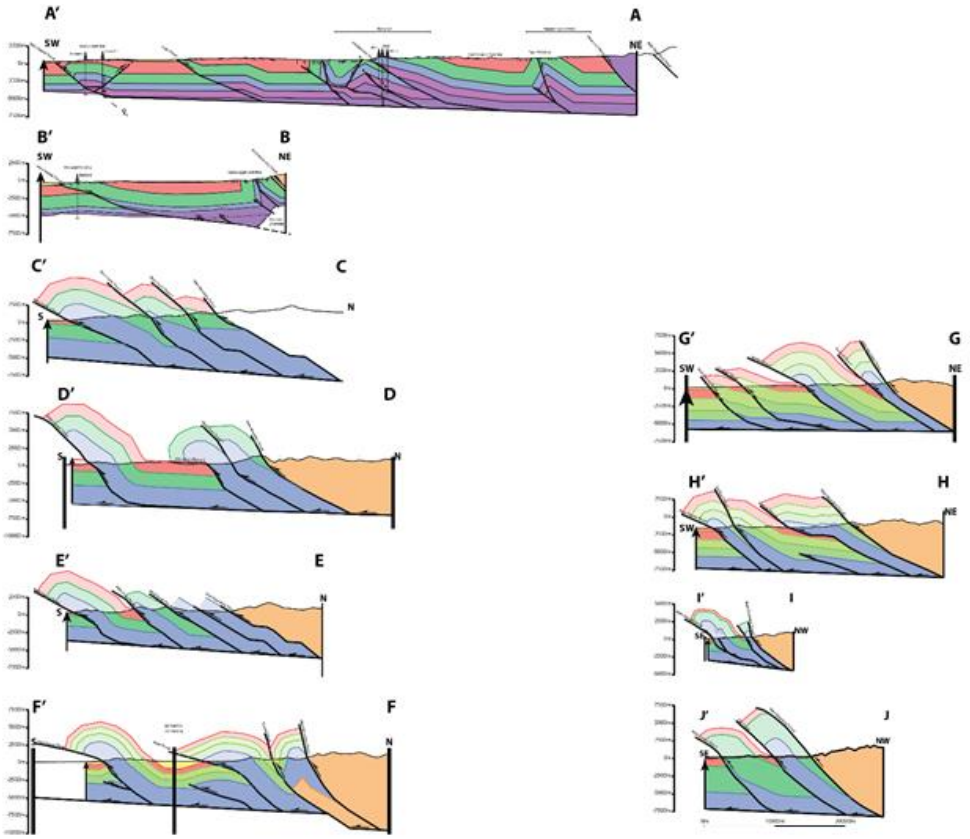

B)

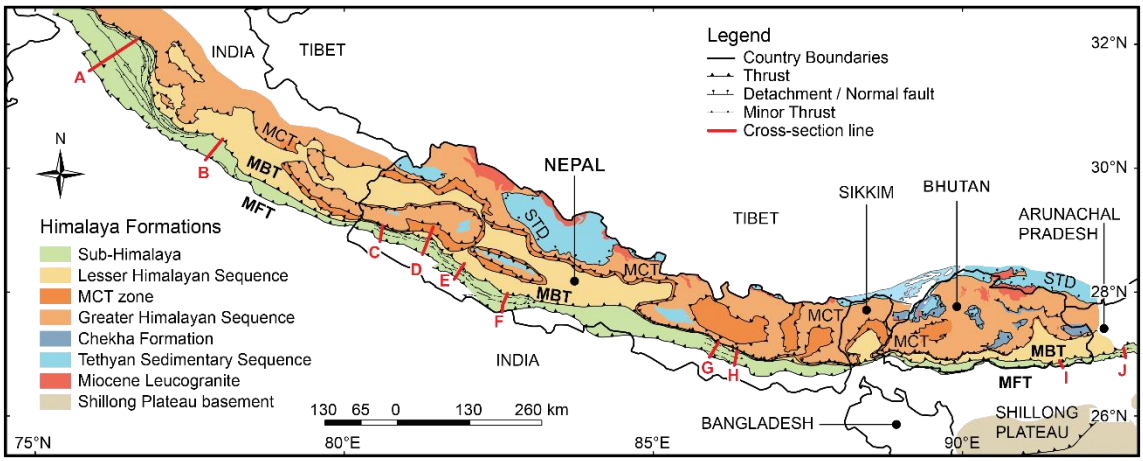

Figure 2.4: A) Cross-sections of the SG along-strike of the Himalayan arc, after Hirschmiller (2013). B) Map of the Himalayas showing the locations of cross-sections in red, after Hirschmiller et al. (2014).

2.3 Critical Taper Wedge Theory

Critical Coulomb wedge (CCW) theory describes the mechanics FTBs. In cross-section, CCWs have an overall wedge-shaped geometry; their formation has been described using the analogy of a bulldozer moving up a surface which is inclined at an angle β (with respect to horizontal), and covered in a uniform layer of sand of thickness T (Figure 2.3). As the bulldozer moves up the surface at a velocity v, sand begins to accumulate in a wedge-shape in front of the bulldozer. This wedge of sand deforms internally until it reaches an angle α (with respect to horizontal). The angle $\alpha+\beta$ is referred to as the critical taper, and remains constant for a CCW with constant material properties. Once the critical taper angle has been achieved, the wedge will slide stably over the surface, and widen or narrow in order to maintain its critical taper as material is accreted to or removed from its toe (Davis et al., 1983).

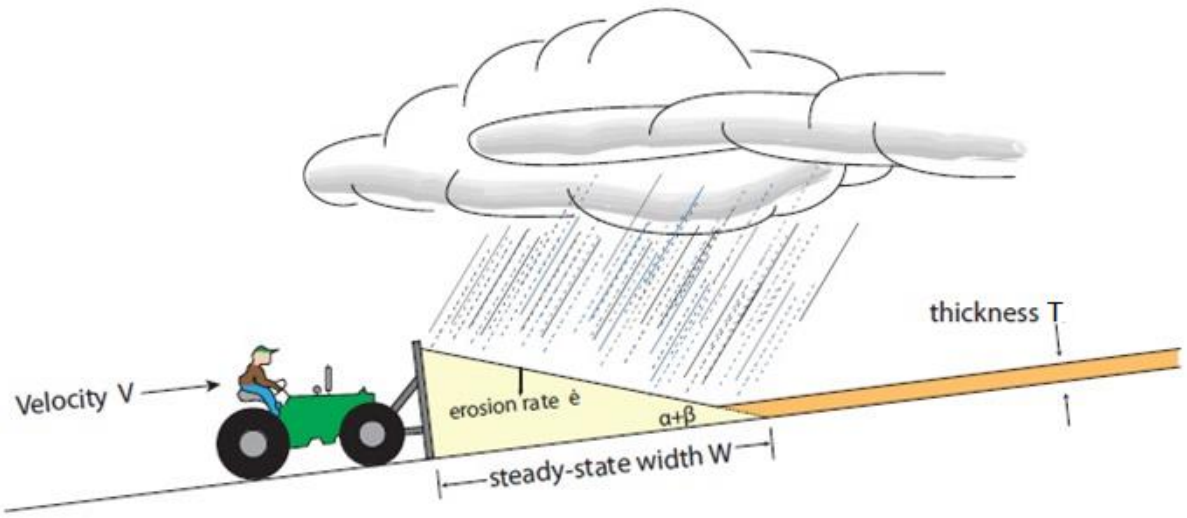

Figure 2.5: Cartoon illustrating the self-similar growth of a "bull-dozer wedge" which is analogous to steady-state CCW, after Dahlen (1990).

Assuming the density of the material (ρ) remains constant, the growth of the wedge with time can be described by the mass conversion law (Dahlen, 1990)

$$\frac{d}{dt}\left[\frac{1}{2}\rho W^2 \tan(\alpha+\beta)\right] = \rho v T \tag{2.1}$$

where W is the width of the wedge. Because the critical taper (α+β) remains constant, equation (2.1) can be reduced and solved to give the approximation

$$W = \left[\frac{2vTt}{\tan(\alpha+\beta)}\right]^{1/2} \approx \left[\frac{2vTt}{\alpha+\beta}\right]^{1/2} \tag{2.2}$$

which is valid provided the critical taper angle is narrow (i.e. $\alpha+\beta << 1$ radian). The wedge will grow in a self-similar manner, such that the both the height and width of the wedge will grow at a rate of $t^{1/2}$ (Dahlen, 1990).

The wedge will achieve dynamic steady-state growth when the accretionary flux of material into the wedge is balanced by the erosive flux of material out of the wedge. Dahlen (1990) defined the steady-state width of a uniformly eroding wedge as the flux balance condition:

$$\dot{e}W \sec(\alpha + \beta) \approx \dot{e}W = vT \tag{2.3a}$$

where $\dot{e}$ is the rate of erosion. This expression can be re-written in the form:

$$W = \frac{vT}{\dot{e}} \tag{2.3b}$$

The wedge will continuously deform internally in order to balance the flux of material into and out of the wedge and to maintain its critical taper angle.

2.4 Calculating the Critical Taper Angle

The derivation of the critical taper angle described here follows Dahlen (1990). The critical taper angle can be calculated by examining the balance of three forces on an infinitesimal segment of the wedge, located between *x* and *x* + *dx*; the force of gravity (F_g), the force along the base of the wedge (F_b), and the compressive forces (F_s) acting on the segment of the wedge (Dahlen, 1990). The force of gravity on the infinitesimal portion of the wedge is described by the equation:

$$F_g = -\rho g h \sin\alpha \, dx \tag{2.4}$$

where *g* is the acceleration due to gravity and *h* is the local thickness of the wedge. The force of gravity on the wedge acts in the negative *x* direction. Using the convention that compressive stress is negative, the compressive forces are described by the following equation:

$$F_s = \int_0^h [\sigma_{xx}(x + dx, z) - \sigma_{xx}(x, z)]dz \tag{2.5}$$

Lastly, the force acting on the base of the wedge is given by:

$$F_b = [\tau_b \cos(\alpha + \beta) - \sigma_n \sin(\alpha + \beta)]$$

(2.6)

where τ_b is the shear stress and σ_n is the normal stress. This normal force acts on the wedge in the positive *x* direction.

It is assumed that sliding friction along the base of the wedge is described by:

$$\tau_b = \mu_b \sigma_n$$

(2.7)

where μ_b is the coefficient of friction along the décollement. Equation 2.6 can be reduced to the form:

$$F_b = -\sigma_n[\mu_b \cos(\alpha + \beta) + \sin(\alpha + \beta)]dx$$

(2.8)

Therefore, the balance of forces is given by:

$$F_g + F_s + F_b = 0$$

(2.9)

The force of gravity (F_g) and the compressive force (F_s) act in the negative *x* direction, while the frictional force (F_b) acts in the positive *x* direction. If the limit is taken as $dx \rightarrow 0$, equation 2.9 reduces to:

$$-\rho g h \sin\alpha - \sigma_n[\mu_b \cos(\alpha + \beta) + \sin(\alpha + \beta)] + \frac{d}{dx}\int_0^h \sigma_{xx} dz = 0$$

(2.10)

Dahlen (1990) noted that the approximations $\sin\alpha \approx \alpha$, $\cos(\alpha + \beta) \approx 1$, $\sin(\alpha + \beta) \approx \alpha + \beta$, and $\sigma_n \approx -\rho g h$ can be employed to simplify equation 2.10, provided that $\alpha << 1$ and $\beta << 1$. Using these approximations, equation 2.10 can be written in the form:

$$\rho g h(\beta + \mu_b) + \frac{d}{dx}\int_0^h \sigma_{xx}\, dz \approx 0 \tag{2.11}$$

The failure criterion for non-cohesive dry sand is given by:

$$\frac{\sigma_1}{\sigma_3} = \frac{1 + \sin\phi}{1 - \sin\phi} \tag{2.12}$$

where σ_1 is the greatest principal compressive stress, σ_3 is the least principal compressive stress, and ϕ is the angle of internal friction (Jaeger and Cook, 1979). For a narrow taper, the principal stresses σ_1 and σ_3 can be assumed to be acting vertically and horizontally, respectively. Therefore, σ_{xx} and σ_{zz} can be expressed as follows:

$$\sigma_{xx} \approx \sigma_3 \approx -\rho g z \tag{2.13a}$$

$$\sigma_{zz} \approx \sigma_1 \approx -\left(\frac{1 + \sin\phi}{1 - \sin\phi}\right) \tag{2.13b}$$

The simplified version of compressive forced in equation (2.11) can then be reduced to:

$$\frac{d}{dx}\int_0^h \sigma_{xx} dz \approx -\left(\frac{1 + \sin\phi}{1 - \sin\phi}\right)\rho g z(\alpha + \beta) \tag{2.14}$$

If equation 2.14 is substituted into equation 2.11, the equation for the approximate critical taper of dry sand being pushed by a bulldozer, as described in the previous section:

$$(\alpha + \beta) \approx -\left(\frac{1 + \sin\phi}{1 - \sin\phi}\right)(\beta + \mu_b) \tag{2.15}$$

Upon examining equation 2.15 it becomes evident that increasing the angle of internal friction (ϕ) will decrease the critical taper angle, while increasing the friction (μ_b) along the décollement will increase the critical taper angle.

In order for a wedge to be considered critical, $\sigma_{xx} \approx \sigma_{zz}$ (Figure 2.6). These two stresses can be related using the following Coulomb failure law:

$$\sigma_{xx}^{failure} \approx -\left(\frac{1+\sin\phi}{1-\sin\phi}\right)\rho g z \tag{2.16}$$

A wedge with $\sigma_{xx} > \sigma_{xx}^{failure}$ is considered subcritical, and the taper will continue to increase until it reaches its critical taper value (Figure 2.6). Conversely, a wedge with $\sigma_{xx} < \sigma_{xx}^{failure}$, is considered supercritical, and will not deform internally unless more material is accreted at the toe of the wedge (Figure 2.6). This is achieved by propagation of the décollement into the foreland (Dahlen, 1990).

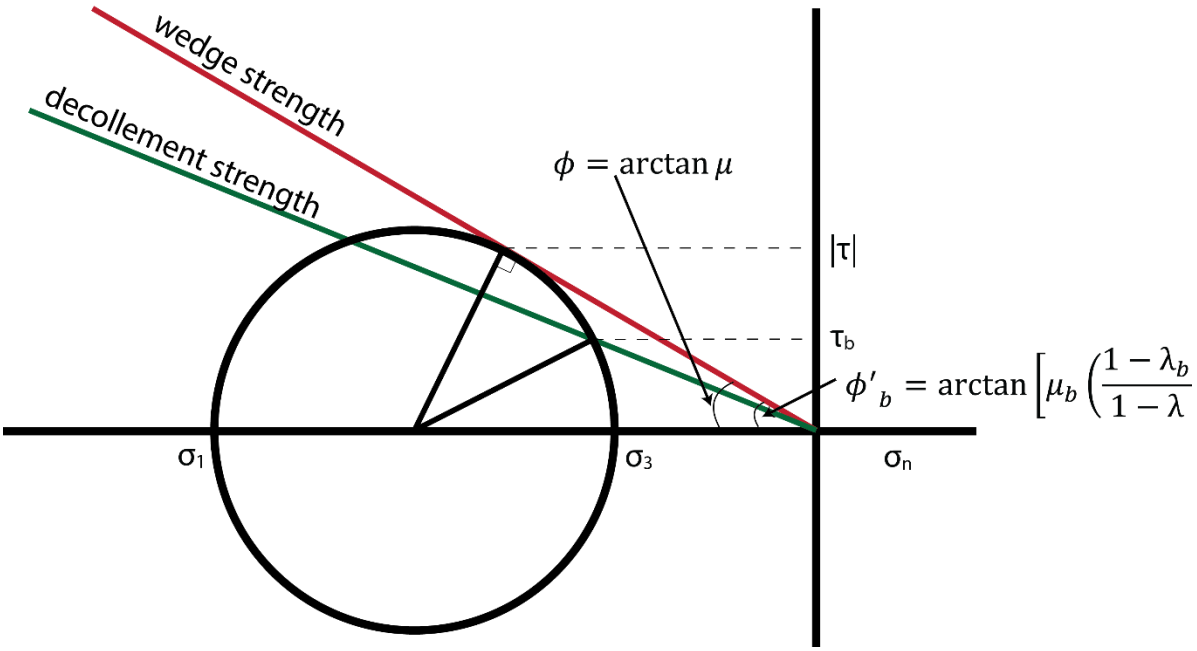

Figure 2.6: Mohr circle illustrating the state of stresses within a critical Coulomb wedge and along its décollement. The maximum and least principle stresses within the wedge are given by σ_1 and σ_3 respectively, ϕ and ϕ'_b are the angle of internal friction and along the décollement, τ_b represents shear traction along the décollement, and is given by the intersection of the frictional failure law $|\boldsymbol{\tau}| = \boldsymbol{\mu_b \sigma_n}$ and the Mohr circle, and μ and μ_b are the coefficients of friction within the wedge and along the décollement respectively, after Davis et al. (1983).

3.0 Experimental Methods and Results

Hilley and Strecker (2004) and Hilley et al. (2004) developed an analytical solution that allows for the rate of change of the average décollement angle (β) to be expressed as a function of both the mechanical and erosional properties of the wedge (Figure 3.1). The mechanical properties of the wedge are given by the coefficient of friction within the wedge (μ) and along the décollement (μ_b), as well as the pore fluid pressure ratio within the wedge (λ) and along the décollement (λ_b). The parameters representing surface processes are given by the rock erodibility constant (K), the area-length coefficient (k_a), the exponent in the area-length relationship (h), and the area exponent (m) and the slope exponent (n) in the erosion rule. The parameter K represents the effects of lithology and climate, the parameters k_a and h depend on the catchment geometry, and the exponents in the erosion rule (m and n) represent physical processes that erode the channel bed.

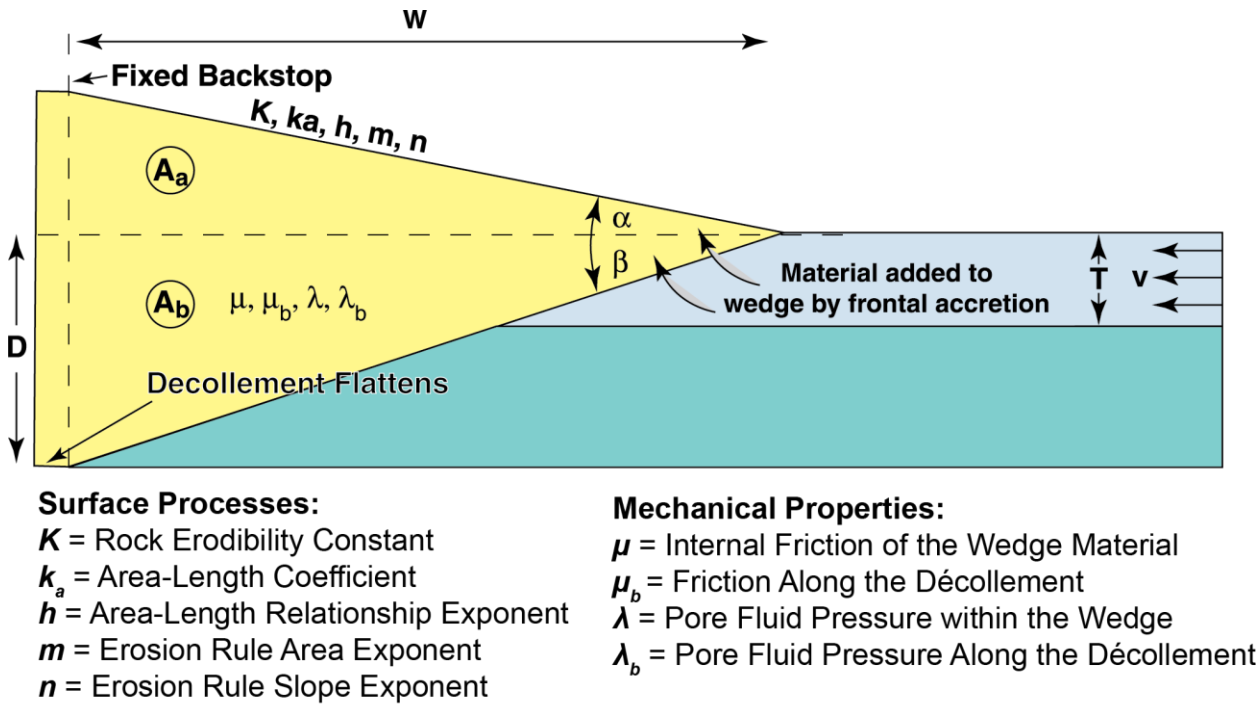

Figure3.1: Diagram of a critical Coulomb wedge showing parameters used in numerical experiments. The wedge has a critical taper angle of $\alpha+\beta$, a width of W, a décollement that flattens at a depth of D, and frontally accretes material of a thickness T, the plate convergence velocity is given by v. Surface processes are reflected in the parameters K, k_a, h, m and n; whereas the mechanical properties are given by μ, μ_b, λ and λ_b.Image modified from Hilley and Strecker (2004).

3.1 Model Formulation

The analytical solution developed by Hilley et al. (2004) assumes that: 1) material is added to the wedge exclusively through frontal accretion of foreland sediments; 2) the wedge loses material through erosion and transport of sediment to the foreland; 3) the wedge continuously adjusts its cross-sectional area through time by internal, brittle deformation in order to maintain its critical taper angle; and 4) the density of both the material comprising the wedge and the material accreted to the wedge remains constant. Hilley et al. (2004) described the mass balance of the wedge in terms of the following volume balance:

$$\frac{dA}{dt} = F_a - F_e \tag{3.1}$$

where *dA/dt* is the change in cross-sectional area of the wedge with time, F_a is the volume flux of material added to wedge through frontal accretion, and F_e is the volume flux of material out of the wedge through erosion.

The upper (i.e. internal) portion of an orogen acts as a rigid backstop against which material is added to the wedge through frontal accretion of foreland material. Therefore, growth of an orogenic wedge is accomplished through the accretion of foreland sediments during continued plate convergence (Hilley et al., 2004). DeCelles and DeCelles (2001) described the volume flux of material into the wedge as the product of the plate convergence velocity (v) and the thickness of the foreland material accreted to the wedge (T):

$$F_a = vT \tag{3.2}$$

Erosion will remove a portion of the material that is frontally accreted to the wedge. The rate of fluvial incision into bedrock will limit both the slope and relief of the surface of an orogenic wedge (Whipple and Tucker, 1999). The rate of fluvial incision into bedrock has been described by Howard et al. (1994) as the change in elevation over time:

$$\frac{dz}{dt_b} = -KA^m S^n \tag{3.3}$$

where A represents the catchment area, used as a proxy for discharge (Howard et al., 1994), S represents the channel slope, and K is a constant that represents the erodibility of the rocks as well as the erosive effectiveness of climate (Howard et al., 1994; Stock and Montgomery, 1999). In this case the subscript b is used to indicate that this eroded material is derived from the portion of the orogenic wedge above the foreland. The power law exponents, m and n are experimentally derived

constants which represent physical processes that erode the channel bed, such as plucking and scouring (Howard et al., 1994).

Following the work of Hack (1957), Hilley et al. (2004) expressed the catchment area as:

$$A = k_a x^h \tag{3.4}$$

where x is the downstream profile position, and k_a and h are constants which are determined by the geometry of the catchment (Hilley et al., 2004).

Hilley et al. (2004) combined equations 3.3 and 3.4 to use the downstream profile position (x) to express the rate of change in elevation of the channel:

$$\frac{dz}{dt_b} = -K{k_a}^m x^{hm} S^n \tag{3.5}$$

The volume flux of material out of the wedge (F_e) through erosion is then given by integrating equation 3.5 with respect to the width of the wedge (W) (Hilley et al., 2004):

$$F_e = -\int_0^W \frac{dz}{dt_b} dx = \frac{K{k_a}^m x^{(hm+1)}}{hm+1} S^n \Big|_0^W \tag{3.6}$$

To estimate the effects on wedge geometry of the material flux into and out of the wedge, Hilley et al. (2004) treated the rate of change of the wedge's cross-sectional area (dA/dt) as the sum of the rate of change of the area above (dA/dt_a) and below (dA/dt_b) the foreland surface:

$$\frac{dA}{dt} = \left[\frac{dA}{dt}\right]_a + \left[\frac{dA}{dt}\right]_b \tag{3.7}$$

Consistent with DeCelles and DeCelles (2001), Hilley et al. (2004) related the rate of change in the wedge cross-sectional area below the foreland surface (dA/dt_b) to the rate of change in the décollement angle (β) and the width of the wedge (W) as follows:

$$\left[\frac{dA}{dt}\right]_b = \left(W \tan\beta \frac{dW}{dt} + \frac{W^2}{2cos^2\beta}\frac{d\beta}{dt}\right) \tag{3.8}$$

Hilley et al. (2004) related the wedge width (W) to the décollement dip (β) by assuming that the décollement flattens at a depth D (hereafter referred to as the sole-out depth), and treated this depth as the brittle-plastic transition. The location of D is also treated as the rigid backstop to the wedge because beyond the brittle-plastic transition the assumption of brittle-frictional deformation is no longer valid. Therefore, the relationship between the wedge width and its rate of change over time may be expressed in terms of the décollement angle (β) as:

$$W = D \cot\beta \tag{3.9}$$

and

$$\frac{dW}{dt} = -D\csc^2\beta \frac{d\beta}{dt} \tag{3.10}$$

Substituting equation (3.9) and (3.10) into equation (3.8) gives the change in wedge cross-sectional area exclusively in terms of the décollement angle (β) and its rate of change:

$$\left[\frac{dA}{dt}\right]_b = -\frac{D^2\csc^2\beta}{2}\frac{d\beta}{dt} \tag{3.11}$$

Similarly, the change in cross-sectional area of the wedge above the foreland surface (dA/dt_a) is a function of both the wedge width (W) and surface slope (α), and can be expressed as (Hilley et al., 2004):

$$\left[\frac{dA}{dt}\right]_a = W \tan\alpha \frac{dW}{dt} + \frac{W^2}{2\cos^2\alpha}\frac{d\alpha}{dt} \tag{3.12}$$

Substituting equation (3.10) into equation (3.12) yields:

$$\left[\frac{dA}{dt}\right]_a = -\frac{D^2 \tan\alpha \csc^2\beta}{\tan\beta}\frac{d\beta}{dt} + \frac{D^2\cot^2\beta}{2\cos^2\alpha}\frac{d\alpha}{dt} \tag{3.13}$$

Hilley et al. (2004) related the surface slope (α) to the décollement angle (β) using CCW theory (Chapter 2.3), which allows the change in cross-sectional area of the wedge (dA/dt) to be expressed as a function of the décollement angle (β) and the sole-out depth (D). Using equation 3.1, Hilley et al. (2004) combined this result with equations 3.2, 3.3 and 3.7 to establish a relationship between wedge geometry and material flux into the wedge via frontal accretion, and material flux out of the wedge via erosion:

$$\frac{d\beta}{dt} = \left[\frac{-D^2 \tan\alpha\, csc^2\beta}{\tan\beta} + \frac{D^2 cot^2\beta g(\beta)}{2cos^2 f(\beta)} - \frac{D^2 cot^2\beta}{2}\right]^{-1}\left[vT - \frac{K{k_a}^m D^{(hm+1)} cot^{(hm+1)}\beta S^n}{hm+1}\right] \tag{3.14}$$

At the outset of this thesis George Hilley found an error in the originally published equation 3.14; which he promptly revised the equation and the related MatLab scripts. This study uses the corrected version of both the equation and related MatLab scripts to determine the effects of varying parameters individually on wedge width (W), propagation rate (dW/dt), and the critical taper ($\alpha+\beta$). Parameters were chosen to approximate observed properties of the Himalayan

foreland FTB. To begin the process of modeling the Himalayan FTB, calculations presented in Hilley and Strecker (2004) and Hilley et al. (2004) were re-run in order to benchmark new experiments. After benchmarking was completed, a range of values was chosen for each variable in the experiments based on the range of observed values in the Himalayan FTB.

3.2 Constant Parameter Values

This investigation focuses on the effects of varying surface erosional parameter (K) and tectonic controls (v); therefore, the mechanical properties of the wedge (μ, μ_b, λ, λ_b) were not varied. The values for the coefficient of friction within the wedge (μ) and along the décollement (μ_b) were held constant, and both were assigned a value of 0.85 in accordance with Byerlee's law. The values of the erosion power law exponents (m and n) were assigned values of m = 1/3 and n = 2/3 (Hilley and Strecker, 2004), based on the work of Whipple et al. (2000) and Stock and Montgomery (1999). The experiments presented here were completed in two sets. The first set investigates sensitivity of wedge width (W) and wedge propagation rate (dW/dt) to the surface parameters (K) décollement depth (D), sediment thickness (T) and the convergence rate (v). To allow comparison with the equivalent work Hilley et al. (2004), the Hubbert-Rubey pore fluid pressure ratio within (λ) and outside (λ_b) the wedge were both assigned a value of λ=λ_b=0, although it was clear that this does not represent the Himalayan FTB. Catchment geometry parameters, k_a and h, were assigned values of 4 and 1.4 respectively for the benchmark experiments (Hilley and Strecker, 2004). The second set of experiments investigated the influence of the ratio between material flux into the wedge and the rock erodibility constant (vT/K) as a function of the erosional parameters of the wedge. The Hubert-Rubey pore fluid pressure ratios within (λ) and outside (λ_b) of the wedge were estimated from the current geometry of the Himalayan FTB, based on recently constructed cross-sections of the Himalayan FTB (Figure 2.4) (Hirschmiller et al., 2014). The

angle α was found to vary between 0.3° and 2.6° (with an average of 1.5°), whereas β was found to vary between 0.5° and 7° (with an average of 3.5°), indicating pore fluid pressure ratios ranging between $\lambda = 0.5$ and $\lambda = 0.97$. The parameters k_a and h were assigned values of 9.4 and 1.65 respectively, in accordance with Hilley and Strecker (2004), who compared topographic data obtained using a digital elevation model (DEM) and river flow direction grids with values predicted by equation 3.5, which describes the catchment area (A) in terms of position along the downstream profile (x). Hilley and Strecker (2004) compared RMS misfits of measured and predicted values from equation 3.5 to constrain k_a and h for the Himalayan orogen.

3.3 Varied Parameter Values

Varied parameters included rock erodibility (K), volume flux per unit width of material (vT), and the sole-out depth of the décollement (D) (Figure 3.1). The experimental range of values for vT and D were based on the results of the balanced and retro-deformed cross-sections constructed by Hirschmiller et al. (2014), vT was varied over four values between 10 m^2/yr and 70 m^2/yr, and D was varied over four values ranging between 4000 m and 10,000 m (Figure 2.4). Experiments were also conducted in which T was varied separately from v, in order to establish the effect of varying T for constant v for different values of K. The range of values for T, also taken from Hirschmiller et al. (2014), varied between 2000 m and 8000 m (Figure 2.4). Table 3.1 shows the reference values used for the model parameters, which represent the averages of the observed values reported by Hirschmiller et al. (2014). The experiments were conducted so that each parameter was varied individually while the other parameters were held constant and assigned their corresponding reference values (Table 3.1).

Table 3.1: Reference values used in model experiments. Parameters shown without units are dimensionless.

Parameter	Reference Value
K ($m^{(1-2m)}/yr$)	5×10^{-5}
D (m)	8000
vT (m^2/yr)	50
v (m/yr)	0.0083
T (m)	6000
k_a (m^{2-h})	9.4
h	1.65
m	1/3
n	2/3

3.3.1 Methods for Varying Pore Fluid Pressure (λ and λ_b)

Pore fluid pressure ($\lambda=\lambda_b$) was varied over four values ranging between 0 and 0.9 (Table 3.3). Previous models of the Himalayas (Hilley and Strecker, 2004, and references therein) estimated pore fluid pressure ratios ranging between 0.6 and 0.8. However, in the study by Hilley et al. (2004), pore fluid pressure was assigned a value of zero. Therefore, for direct comparison to the equivalent study, a pore fluid pressure ratio of zero was also used for all other experiments in the current study, except those shown in Figure 3.2.

3.3.2 Methods for Varying Thickness (T)

In order to test the effect of varying the thickness (T) of accreted foreland material on the growth of the Himalayan FTB, thickness had to be varied separately from velocity, as the two

parameters occur as a product in all model calculations. The base value vT = 50 m^2/yr was chosen for the experiments, as this is the average value of accreted sediment flux calculated from balanced and retro-deformed cross-sections (Hirschmiller et al., 2014). The thickness of the SG (i.e. the Himalayan FTB) varies from 2950 m to 7550 m (Hirschmiller et al., 2014). The average thickness of ~ 6000 m was used as a reference value when varying other parameters in our experiment. The parameter T was varied over four values, and in each case a velocity was chosen such that their product would be equal to the average observed accreted sediment flux (i.e. vT = 50 m^2/yr). The velocity corresponding to each experimental value of T is also shown in Table 3.2 in red.

Table 3.2: Experimental runs for varying thickness of accreted sediments (T). Individual experiments were conducted using four different K values (Table 3.3), all other parameters were assigned values shown in Table 3.1.

T = 2000 m	T = 4000 m	T = 6000 m	T = 8000 m
v = 0.025 m/yr	v = 0.025 m/yr	v = 0.025 m/yr	v = 0.025 m/yr
v = 0.0125 m/yr	v = 0.0125 m/yr	v = 0.0125 m/yr	v = 0.0125 m/yr
v = 0.0083 m/yr	v = 0.0083 m/yr	v = 0.0083 m/yr	v = 0.0083 m/yr
v = 0.00625 m/yr	v = 0.00625 m/yr	v = 0.00625 m/yr	v = 0.00625 m/yr

3.3.3 Methods for Varying Accreted Sediment Flux (vT)

The range of values used to model the effects of changing accreted sediment flux (vT) were also taken from the range of values estimated by Hirschmiller et al. (2014) from their balanced and retro-deformed cross-sections. The range of calculated values varied between 9.4 ± 2.0 m^2/yr and 64.3 ± 12.1 m^2/yr, with a median value of approximately 50 m^2/yr (Figure 2.4); therefore we chose vT = 50 m^2/yr as our reference value for all other experiments where vT was held fixed. Table 3.3

shows the range of *vT* values used in experiments to test the effect of varying *vT* on wedge width and wedge propagation rates.

3.3.4 Methods for Varying Sole-Out Depth (D)

The range of values chosen to test the effect of varying the sole-out depth (*D*) on wedge width and propagation rate in the Himalayan FTB were based on the observed range of values reported by Hirschmiller et al. (2014) in their balanced and retro-deformed cross-sections of the Himalayan FTB (Figure 2.4). The sole-out depth (*D*) was varied over four different values that were representative of the total range presented by Hirschmiller et al. (2014). The average value of *D* was found to be approximately 8000 m, so this was used as the reference value of *D* for all other experiments where *D* was held constant. Table 3.3 shows the range of values used for the experiments that tested the effects of varying *D* on wedge width (*W*) and wedge propagation rate (*dW/dt*).

Table 3.3: Range in experimental values for sole-out depth (*D*), sediment flux (*vT*), and rock erodibility (*K*).

Sole-out Depth (*D*) (m)	**Sediment Flux (*vT*) (m^2/yr)**	**Rock Erodibility (*K*)**	**Pore Fluid Pressure (*λ*)**
4000	10	1×10^{-7}	0
6000	30	1×10^{-6}	0.5
8000	50	1×10^{-5}	0.8
10000	70	1×10^{-4}	0.9

3.3.5 Methods for Varying Rock Erodibility (K)

Howard et al. (1994) recognized that in regions like the Himalayan FTB, where bedrock incision is the primary means of fluvial erosion, climatic variation plays an important role in quantifying erosion rates, as bedrock incision is affected by the amount of discharge in a fluvial system. Our model assumes that, because rocks of the Siwalik Group have constant lithology along- and across-strike of the Himalayan arc, their erodibility along the arc is also constant. Therefore, the modelled variation in *K* represents variation in mean annual precipitation along the Himalayan arc, rather than variation in the erodibility of the rocks themselves.

Variation of *K* for different lithologies was explored by Stock and Montgomery (1999). It was found that *K* varies over three orders of magnitude for different lithologies in humid regions; $K=1\times10^{-4}$ for mudstones and volcanoclastic rocks, $K=6\times10^{-6}$ for basalt flows and $K=1\times10^{-6}$ for granitoid and metasedimentary rocks (Stock and Montgomery, 1999). Thus, rocks that are more easily eroded will have a higher *K* value, while more resistant rocks will have a lower *K* value. Experimental values of K were varied over four orders of magnitude: 1×10^{-7}, 1×10^{-6}, 1×10^{-5} and 1×10^{-4}. The alluvial sediments of the Late Miocene-Pliocene Siwalik Group are weakly consolidated and have not been heated above 100 °C (Bernet et al., 2006), and therefore can be reasonably assumed to have high *K* values.

3.4 Experimental Results

The experimental results for varying each parameter individually are discussed below; for values of constant parameters see Table 3.1 and for all experimental model outputs see Appendices A, B and C.

3.4.1 Variation in Pore Fluid Pressure (λ and λ_b)

The results for varying pore fluid pressure (λ and λ_b) are shown in Figure 3.2. When all other parameters are held fixed, higher values of pore fluid pressure result in wider wedges than lower values (Figure 3.2A). The initial propagation rate is independent of the pore fluid pressure; however, the propagation rate decays more slowly for wedges with high pore fluid pressure compared to a wedge with low pore fluid pressure (Figure 3.2B).

A)

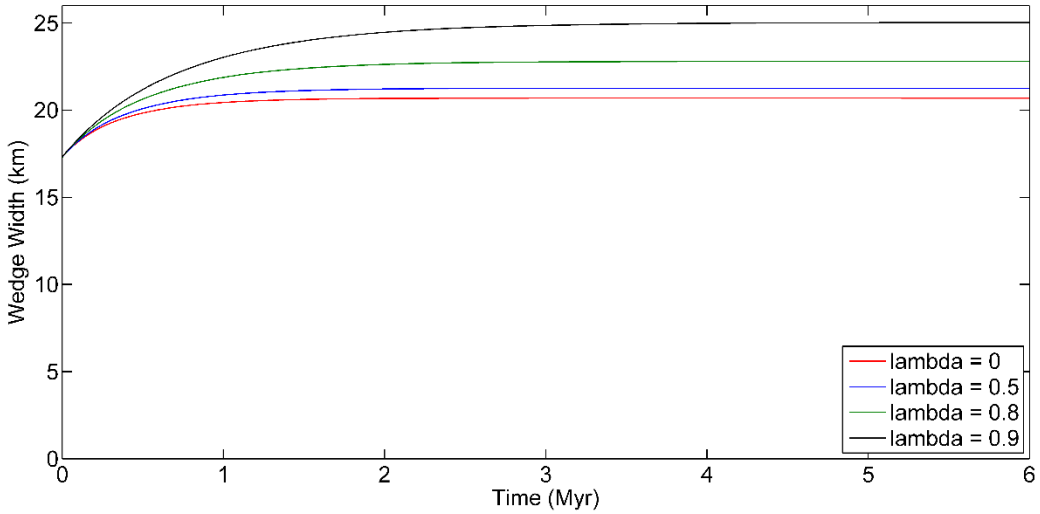

B)

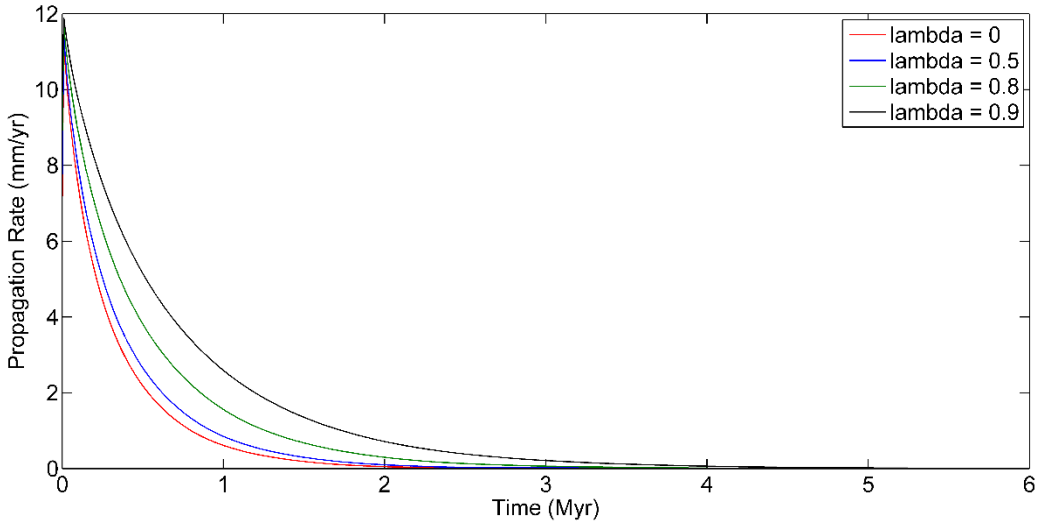

Figure 3.2: The effects of varying pore fluid pressure (λ and λ_b) on; A) wedge width (W), and B) wedge propagation rate (dW/dt).

3.4.2 Variation in Thickness (T)

Figure 3.3 shows an example of an experimental run for varying *T*; each curve on the graphs corresponds to a different value of *T*. In total, sixteen experimental runs were completed to test the effect of varying *T* on wedge width (*W*) and wedge propagation rate (*dW/dt*). Large values of *T* produce wedges that are wider after 6 Ma than small values of *T* (Figure 3.3A). Large values of *T* also produce wedges that have high initial propagation rates which decay quickly, whereas small values of *T* produce wedges with lower initial propagation rates which decay more slowly (Figure 3.3B).

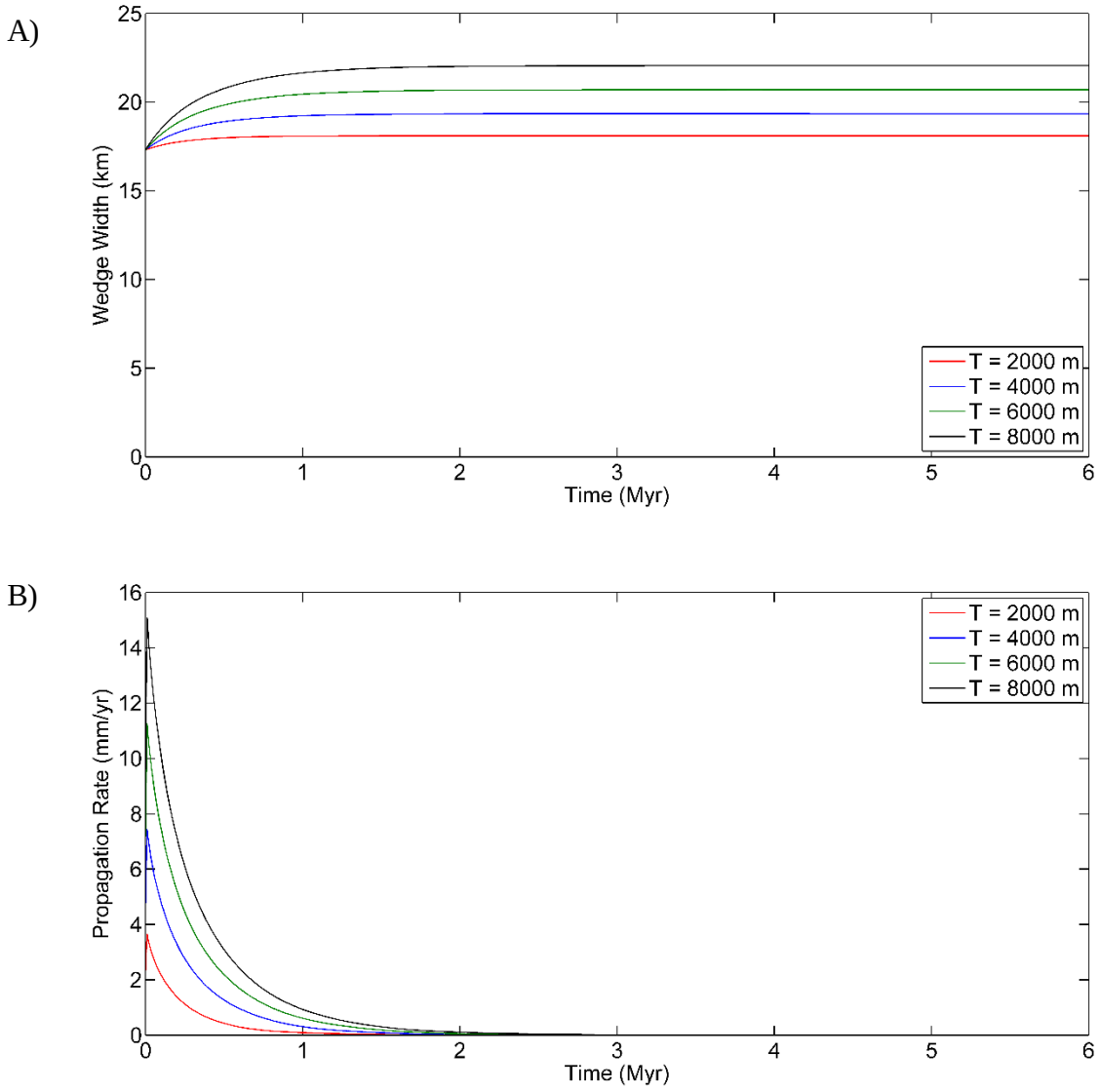

Figure 2.3: The effects of varying thickness (*T*) of accreting foreland sediment on; A) wedge width (*W*), and B) wedge propagation rate (*dW/dt*).

3.4.3 Variation in Sole-Out Depth (D)

The value of *D* is independent of the tectonic parameters in our model calculations (i.e. *v* and *T*), thus, the base value of the accreted sediment flux (vT = 50 m^2/yr) was used with *T* = 6000 m. An experimental run was completed for each value of *D* for four different *K* values. When *D* is shallow (i.e. 4000 m), the initial width of the wedge is narrower than for larger values of *D* (i.e. 10,000m). Furthermore, when all other parameters are held fixed, a wedge with a greater value of

D will become wider over time than a wedge with a smaller value of *D* (Figure 3.4A). The initial propagation rate for small values of *D* is much higher than for large values of *D*, and decays more slowly over time (Figure 3.4B).

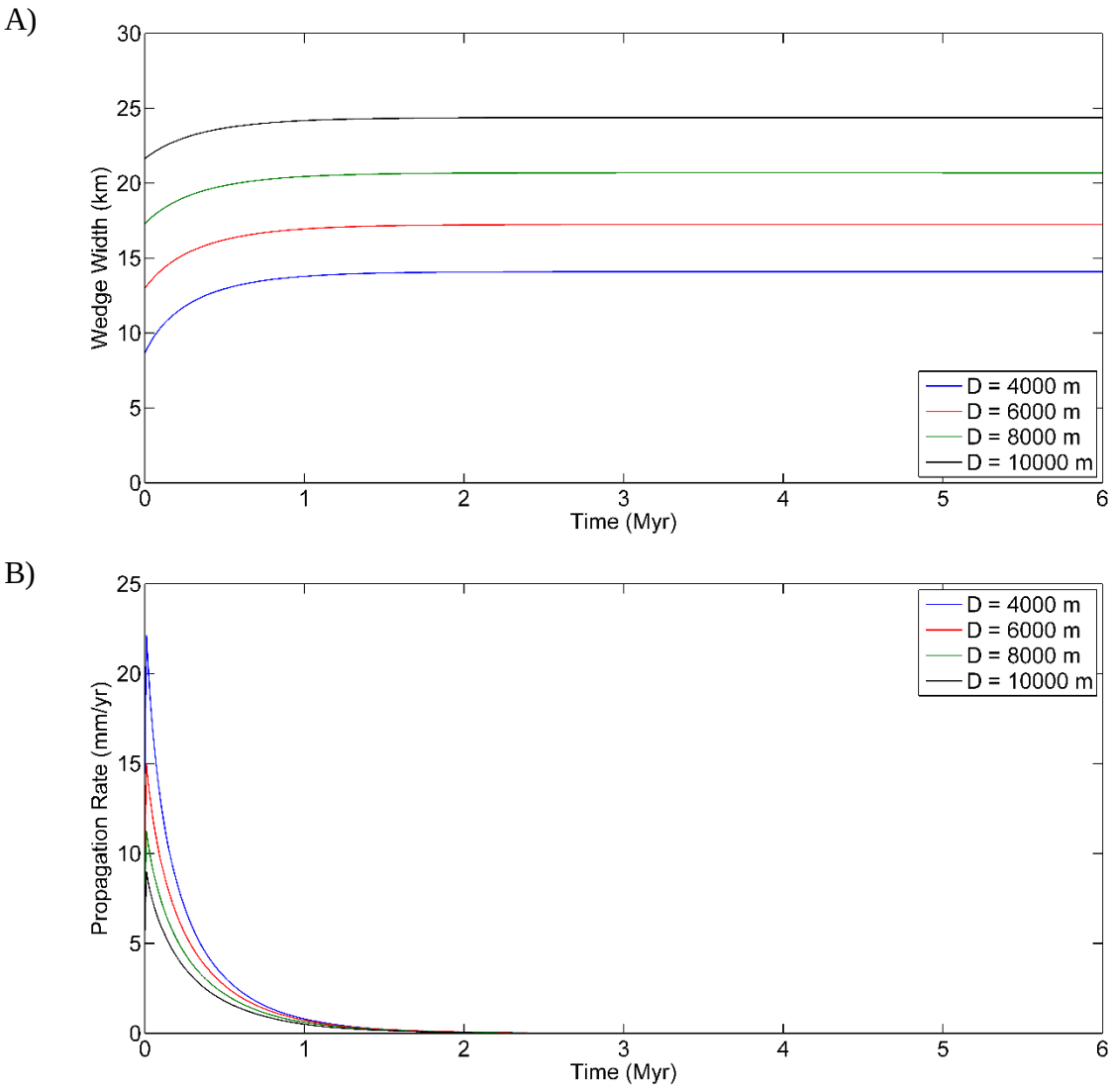

Figure 3.4*:* The effects of varying sole-out depth (*D*) on; A) wedge width (*W*), and B) wedge propagation rate (*dW/dt*).

3.4.4 Variation in Sediment Flux (vT)

The product of the convergence velocity (v) and the thickness of foreland material (T) represents the flux of material accreted to the wedge per unit wedge width (vT), therefore it is expressed in m^2/yr. When all other parameters are held fixed, large values of vT result in wider wedges after 6 Ma compared to small values of vT (Figure 3.5A). Similarly, large values of vT result in high wedge propagation rates, as material is quickly added to the wedge by frontal accretion. Conversely, small values of vT result in smaller wedge propagation rates, as the rate at which material is frontally accreted to the wedge is slower (Figure 3.5B).

A)

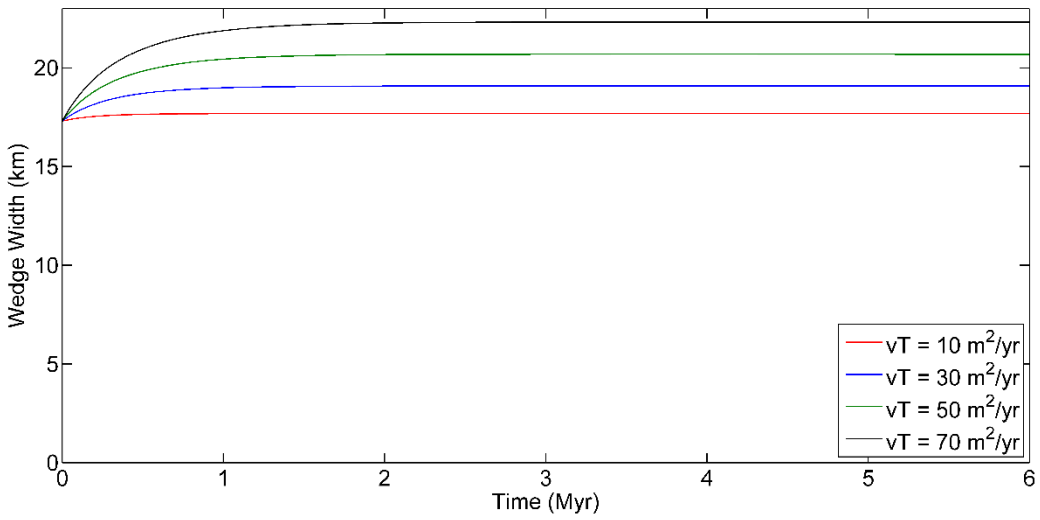

B)

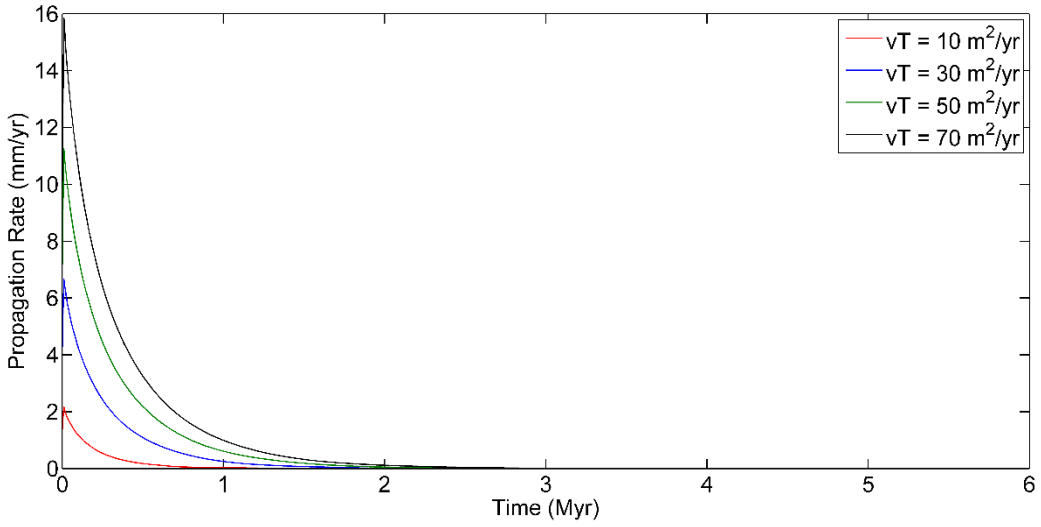

Figure 3.5: The effects of varying sediment flux (*vT*) on; A) wedge width (*W*), and B) wedge propagation rate (*dW/dt*).

3.4.5 Variation in Rock Erodibility (K)

The effects of varying *K* on wedge width (*W*) and propagation rate (*dW/dt*) for a wedge with no initial topography (i.e. $\alpha = 0$) are shown in Figure 3.6. When all other parameters are held fixed, a wedge with a high *K* value will have an initially high propagation rate, which decreases quickly. The wedge will undergo very little growth and achieve a steady state width of ~19 km after 2 Ma for the highest value of *K* (i.e. high precipitation rate). Conversely, the wedge will continue to grow, without reaching a steady state width, for more than 6 Ma in the case where *K* is low. As *K* is lowered by an order of magnitude, the difference in wedge width between *K* values rapidly decreases. For example; after 6 Ma the wedge will obtain a width of 49.27 km for $K = 1.0\times10^{-7}$ and a width of 47.45 km for $K = 1.0\times10^{-6}$, which is a difference in width of 1.82 km for one order

of magnitude increase in *K*. However, this difference is increased to 13.02 km if *K* is increased from K = 1.0×10^{-6} to 1.0×10^{-5}, and 15.54 km if K is increased from K = 1.0×10^{-5} to 1.0×10^{-4}.

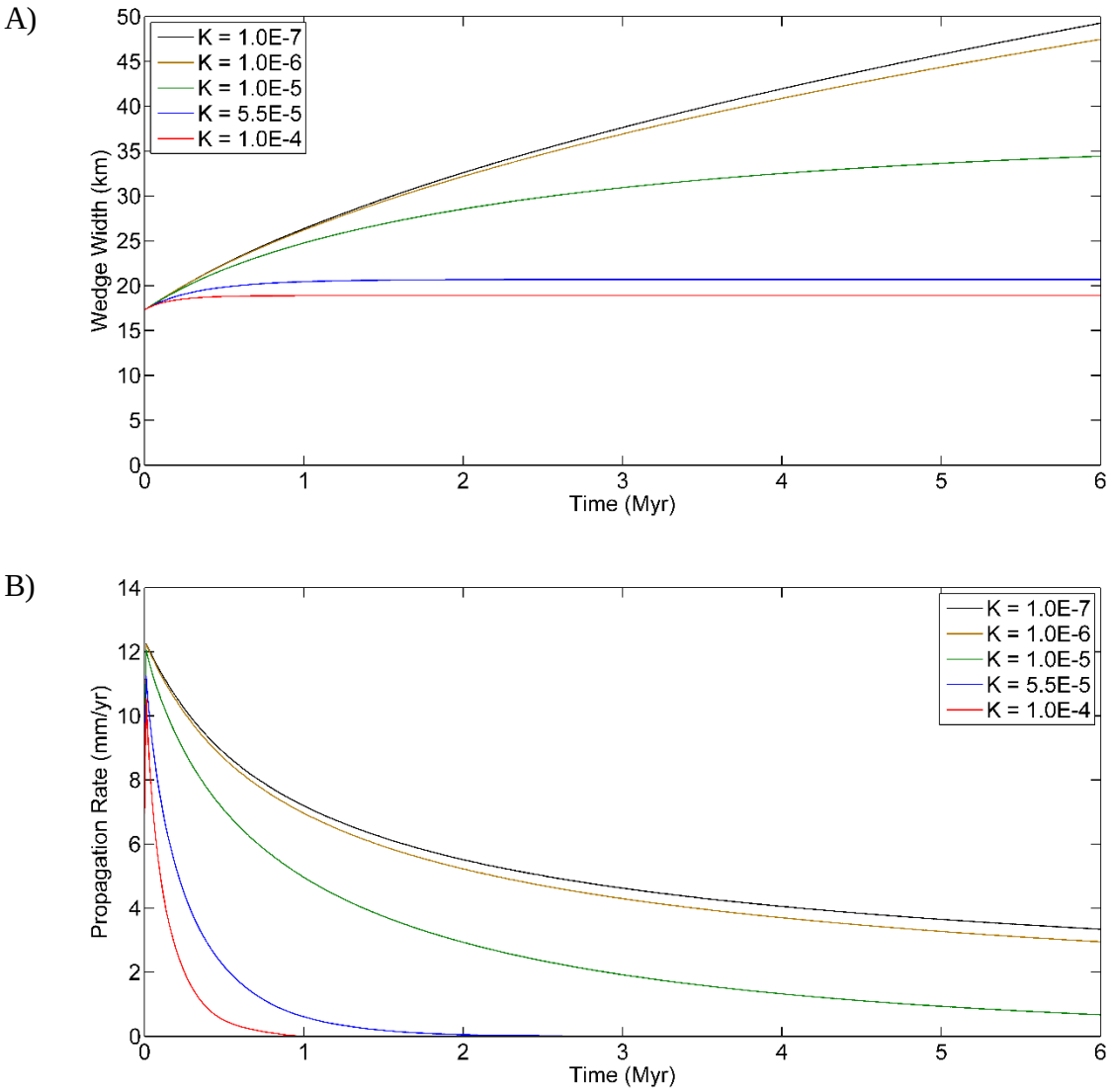

Figure 3.6: The effects of varying rock erodibility (*K*) on; A) wedge width (*W*), and B) wedge propagation rate (*dW/dt*).

4.0 Discussion

Two important observations arose from the work of Hirschmiller et al. (2014). First, there is a west to east increase in strain and strain rate across the Himalayan arc (Figure 4.1A), which is positively correlated with increasing convergence velocities between the Asian and Indian plates. Second, a west to east increase in mean annual precipitation is inversely correlated with FTB width (Figure 4.1B). Recall that the steady-state width of a CCW is given by the expression (Dahlen, 1990):

$$W = \frac{vT}{\dot{e}} \tag{4.1}$$

Equation 4.1 predicts that an increase in convergence velocity should result in an increase in the width of the wedge. However, this prediction does not match observations for the Himalayan foreland FTB, as the width of the FTB decreases from west to east along-strike of the arc (Figure 4.1). Equation 4.1 also predicts that if the rate of erosion is increased, the width of the wedge should decrease. This prediction matches observations from the Himalayan FTB, which led Hirschmiller et al. (2014) to propose that surface processes exert greater control than tectonic processes on the morphology of the Himalayan FTB. The goal of this study is to use a quantitative approach to determine whether surface processes can dominate over tectonic processes, and to determine which combinations of the model parameters K and vT would predict that surface processes dominate in the Himalayan FTB.

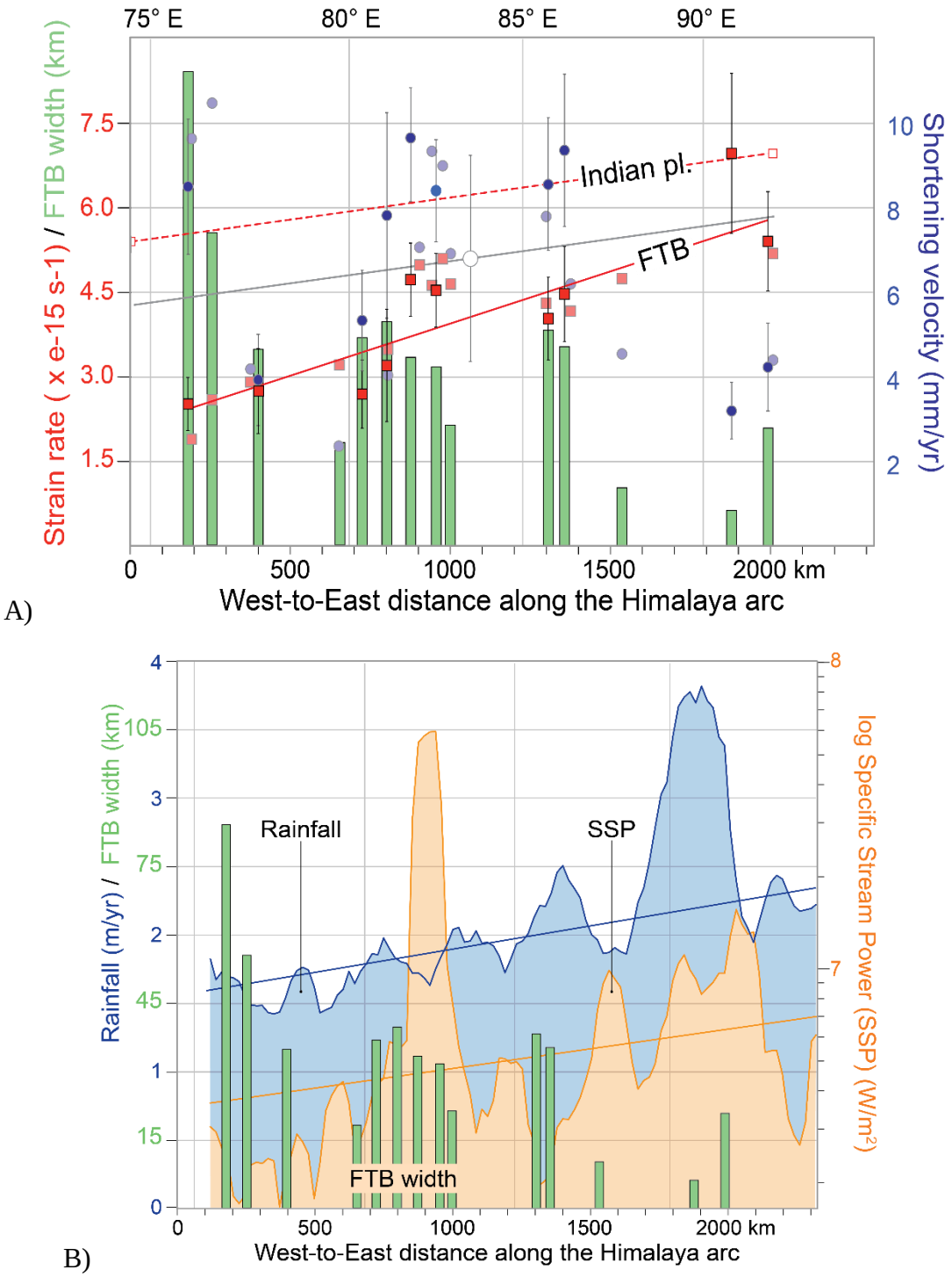

Figure 4.1: A) Graph of strain rate (red squares), shortening velocity (blue circles) and FTB width (green bars) plotted against distance along the Himalayan arc .B) Graph of mean annual rainfall (blue background), specific stream power (orange background) and FTB width (green bars) plotted against distance along the Himalayan arc. The blue and orange lines represent the lines of best fit for mean annual precipitation and specific stream power (SSP), respectively. Image modified from Hirschmiller et al. (2014).

Based on field observations of structures, balanced cross-sections, fluvial terrace deposits and GPS geodetic studies, Mugnier et al. (2004) have concluded that thrusting along the MFT began at ~ 2.4-1.8 Ma in central Nepal. Furthermore, using detrital apatite fission-track thermochronology, van der Beek et al. (2006) dated the onset of exhumation of the Siwalik Group as beginning ~ 2 Ma in western and central Nepal, while Chirouze et al. (2013) dated the onset of exhumation, and thus slip on the MFT, as beginning ~ 1 Ma in Arunachal Pradesh. Based on this information, data obtained from the model experiments in this study were analyzed at t = 2 Ma to determine under which conditions erosion rate can dominate over tectonic processes in controlling the width of the Himalayan FTB.

This study has shown that it is indeed possible for surface processes to dominate over tectonics, and has established threshold relationships between plate convergence velocity (v) and climate (K). However; the exact combination of parameters required to produce model output FTB widths consistent with those observed in the Himalayan FTB has not yet been obtained. Through writing this discussion and carefully analyzing data obtained from experimental models, it has become clear that further work is required to accurately constrain the erosional parameters affecting the Himalayan FTB in order to produce numerical models that match what is observed in nature.

4.1 Geometry of the Himalayan FTB

4.1.1 Mass Removal (K)

The model results obtained from this study show that a wedge with no initial topography and a large K value will have an initially high propagation rate (dW/dt), which decreases to zero within ~1 Ma (Figure 3.6B). Furthermore, the wedge will attain a stable geometry within ~1 Ma, as the initial geometry will be approximately equivalent to the stable geometry (Hilley and

Strecker, 2004). Conversely, a wedge with initially flat topography and lower *K* values will take longer to achieve a stable geometry because erosion is not efficient enough to remove excess material accreted to the wedge. Therefore, the propagation rate for a wedge with lower *K* values will remain relatively high for longer periods of time (Hilley and Strecker, 2004). In regions like the Himalayas, where precipitation rates and rock erodibility are high, *K* values will be high, which allows erosion to keep pace with frontal accretion. The results obtained so far from this study suggest that the Himalayan FTB may have obtained a steady-state geometry near the onset of deformations ~2 Ma.

4.1.2 Frontal Accretion (vT)

The model results obtained from this study show that large values of *vT* result in large initial propagation rates, as frontal accretion quickly adds material to the wedge. Therefore, a larger surface slope (α) is required to remove this accreted material. If the surface slope (α) increases, the décollement angle (β) must decrease in order to maintain the critical taper angle ($\alpha+\beta$), this is achieved by foreland propagation of the wedge (Hilley and Strecker, 2004). Conversely, wedges with smaller *vT* values will have much lower initial propagation rates which decay slowly, as frontal accretion adds material to the wedge at a slower rate (Hilley and Strecker, 2004). If the material flux into the wedge is low enough, the décollement angle may increase in order to maintain the critical taper angle. However, increasing precipitation rates (*K*), and thus erosional efficiency, will also lower the surface slope and will either allow the décollement angle (β) to remain relatively stable, or to decrease for larger values of *vT*. The angle of the décollement (β) and the surface slope (α) of the foreland Himalayan FTB (i.e. the SG) were measured in cross-sections (Hirschmiller, 2013); β was found to range between ~0.5° and ~6.25°, whereas α was found to range between ~0.25° and ~3°. These values differ markedly from β values ranging

between 2° and 4°, and α angles ranging between 3.5° and 4.5°, as previously reported for the entire Himalayan orogen (Hilley and Strecker, 2004, and references therein). This suggests that within the Himalayan FTB the basal décollement angle may be larger and more variable than was previously estimated, this high variability may be a response to variable precipitation rates along-strike of the Himalayan arc.

4.1.3 Sole-Out Depth (D)

A wedge with a smaller value of *D* will have a smaller cross-sectional area, and will respond more quickly to changes in erosion/precipitation rates or accretion flux. Conversely, a wedge with a larger value of *D* will have a larger cross-sectional area, and will take longer to respond to changes in erosion/precipitation rate or accretion flux. Furthermore, a wedge with a large value of *D* will have a lower initial propagation rate that decays slowly over time relative to a wedge with a smaller value of *D*. Therefore, when all other parameters are held fixed, a wedge with a greater sole-out depth is able to become wider over time than a wedge with a shallower sole-out depth (Hilley et al., 2004). Thus, the calculated values of D for the Himalayan FTB could account for scattered variations in wedge geometry, yet the west-to-east trend in FTB geometry is still evident. Almost all cross-sections of the Himalayan FTB were constructed without geophysical data, thus decreasing the accuracy in estimates of *D* and β. Geophysical data on *D* and β have been obtained by the oil and gas industry, and have only recently been made available to researchers; their analysis is in progress (Laurent Godin, personal communication 2014).

4.2 Estimating Pore Fluid Pressure Ratios within the Himalayan FTB

The surface slope (α) and décollement (β) angles of the Himalayan FTB (i.e. the SG) obtained from published balanced cross-sections allow us to estimate the range of pore fluid pressure ratios within the Himalayan FTB (Figure 4.2, field b). The range of α-β pairs resulting

from these new data implies that the Himalayan FTB has extremely high values of pore fluid pressure ratios, ranging between 0.5 and 0.97, with the majority of the data requiring pore fluid pressure values greater than 0.7. This result is consistent with the requirement of a high pore fluid pressure ratio ($\lambda \geq 0.4$, i.e., over pressure) for large overthrusts (Bilotti and Shaw, 2005; Hubert and Rubey, 1959), and also with the lithology of the FTB, which contains young, partially consolidated rocks with many mudstone layers, which are conducive with high overpressure. The grey field labelled "a" in Figure 4.2 is the range of pore fluid pressure ratios predicted by Hilley and Strecker (2004), and shows that when the entire orogenic wedge is modelled, predicted pore fluid pressure ratios will be considerably lower than those within the current FTB is alone.

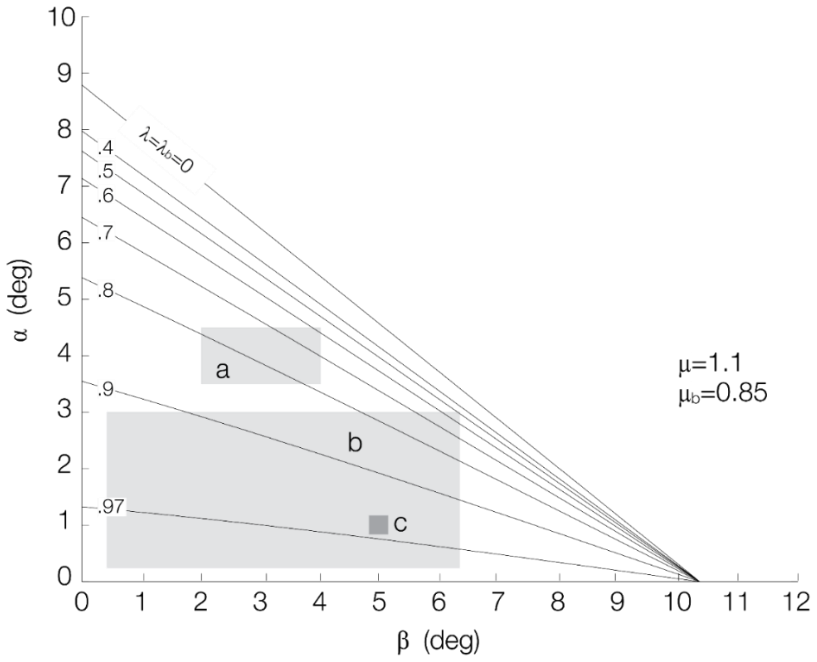

Figure 4.2: Pore fluid pressure ratios predicted for the Himalayan foreland FTB based on measurements of *α-β* pairs from published cross-sections. Values in the grey box, labelled (b) were estimated for the Himalayan FTB by Hirschmiller et al. (2014), the darker box, labelled (c) represents the average value of the *α-β* pairs. The *α-β* pairs presented by Hilley and Strecker (2004) are shown in the grey box, labelled (a), for comparison. Image modified from Hilley and Strecker (2004).

Values of *vT*/*K* were calculated to investigate situations in which the cross-sectional area of the wedge does not change with time. Under such conditions all material frontally accreted to

the wedge is removed by erosion, and the wedge will be in both a mechanical and erosional steady-state (Hilley and Strecker, 2004). These calculations were repeated for two different values of k_a and h; first for k_a = 4, h = 1.4, then for k_a = 9.4, h = 1.65. The first set of values was used to be consistent with Hilley et al. (2004), but are not realistic for the Himalayan FTB (Figure 4.3A). The second set of values were calculated by Hilley and Strecker (2004) for the Himalayan orogen, using a digital elevation model (DEM) (Figure 4.3B). For a wedge that has obtained a mechanical and erosional steady-state, $d\beta/dt$ = 0. If we set the channel slope (S) equal to $S = \tan\alpha$, equation 3.14 reduces to:

$$\frac{vT}{K} = \frac{k_a^{hm} D^{hm+1} \cot^{hm+1}\beta \tan^{n}\alpha}{hm+1} \tag{4.2}$$

which gives the ratio of the material flux into the wedge and the rock erodibility constant (vT/K) as a function of the erosional parameters acting on the wedge (Hilley and Strecker, 2004). Equation 4.2 states that there is a single vT/K value, for a given pair of α and β angles and for a constant set of erosional and catchments geometry constants, which will result in a wedge that maintains a constant cross-sectional area; values of vT/K that are greater or smaller correspond to growing and shrinking wedges, respectively (Hilley and Strecker, 2004). Therefore, the mechanical and erosional steady-state of a wedge with constant D can be determined from the graphical intersection of the calculated CCW function (equation 3.14) and the vT/K value calculated from equation 4.2 (Hilley and Strecker, 2004).

An increase in vT/K may result from a larger convergence velocity (v), increased thickness of frontally accreting sediments (T), or a decrease in K due to increased resistance of the material and/or a reduction in erosional efficiency resulting from a reduction in precipitation rate (Hilley

and Strecker, 2004). For fixed values of α and β, increasing the value of k_a and h (Figure 4.3B) requires lower values of vT/K in order for the wedge to maintain a steady-state geometry (Hilley and Strecker, 2004). Conversely, decreasing the values of k_a and h (Figure 4.3A) requires larger values of vT/K to maintain a steady-state geometry. The set of k_a and h values calculated for the entire Himalayan orogen may not be accurate for the FTB alone; DEM analysis of data for the FTB is required in order to estimate more precisely the values of k_a and h. Constraining the parameters k_a and h exclusively for the FTB is important for calculating vT/K contours and for graphically determining pore fluid pressure ratios.

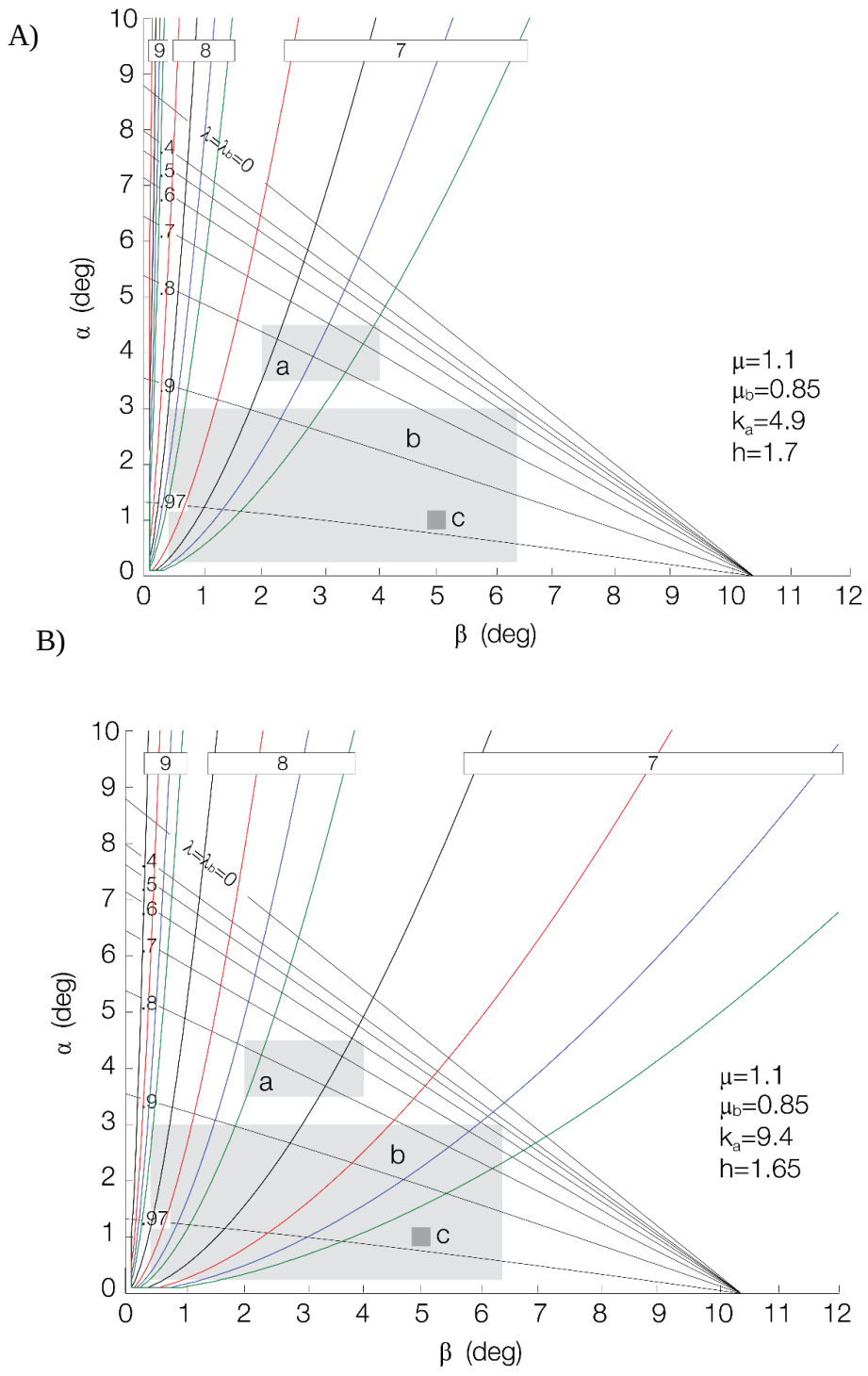

Figure 4.3: Calculated *vT/K* contours (coloured lines) for the Himalayan FTB, superimposed on the estimated range of the pore fluid pressure ratio, for (A) model output with k_a = 4, *h* = 1.4, and (B) model output with *ka* = 9.4 , *h* = 1.65. Values in the grey box, labelled (b), were collected in the Himalayan FTB for this study, the darker box, labelled (c), represents the average value of the *α-β* pairs. The *α-β* pairs presented by Hilley and Strecker (2004) are shown in the grey box, labelled (a), for comparison. Image modified from Hilley and Strecker (2004)

4.3 The Effects of Climate on Erosion Rate ($\dot{\varepsilon}$)

Our model has shown that, for the observed range of values of *D*, *T*, and *vT* in the Himalayan FTB, high precipitation rates can result in a FTB that progressively narrows along-strike, despite the concomitant increase in convergence rate (and thus *vT*). This result can only be achieved for $1\times10^{-5} \leq K \leq 1\times10^{-4}$. High *K* values are consistent with those reported by Stock and Montgomery (1999) for lithologies equivalent to the Siwalik Group sediments, thus we decided to also include an intermediate value of 5×10^{-5} to estimate its influence more precisely.

Bookhagen and Burbank (2010) showed that the rainfall gradient over the Himalayan foreland, related to the Indian summer monsoon, increases six-fold from west to east at elevations < 500 m asl (Figure 4.3). These precipitation data were refined by Hirschmiller et al. (2014), who calculated the precipitation rate exclusively for the foreland FTB (Figure 4.1B). Hirschmiller et al. (2014) estimated that precipitation rates increase by ~40 to 45 % along the strike of the Himalayan arc. This increase in rainfall, and resulting runoff, exerts primary control on removal of material from the wedge by erosion. Whipple and Tucker (1999) argued that erosion rates ($\dot{\varepsilon}$) are controlled by the following stream power erosion law:

$$\dot{\varepsilon} = -KA^m S^n \tag{4.3}$$

where *A* is the catchment area, *S* is the channel slope, *m* and *n* are power law exponents, and *K* is a constant which reflects the erosional efficiency of precipitation as well as the resistance of the material to fluvial incision. Therefore, because the lithology of the SG does not vary along or across the strike of the Himalayan arc, it is assumed that variation in *K* reflects variation in climatically controlled erosional efficiency, and not variation in the erodibility of the rocks themselves.

A)

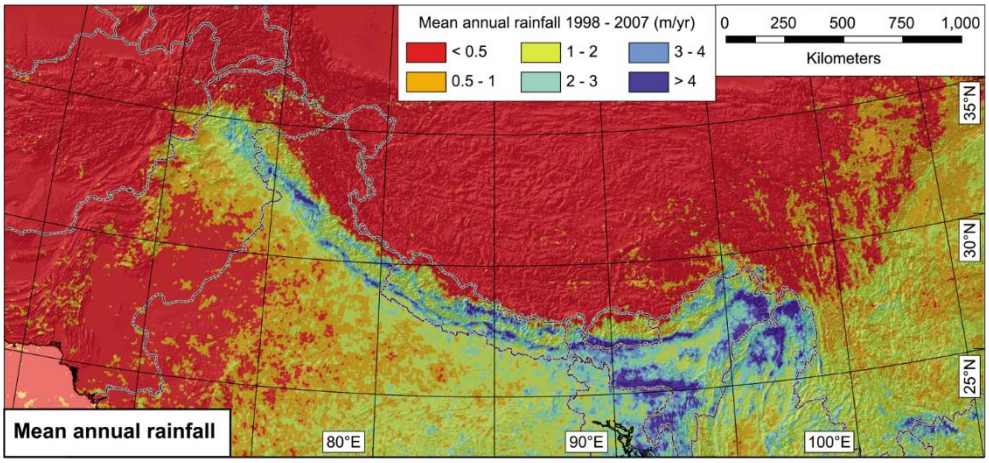

B)

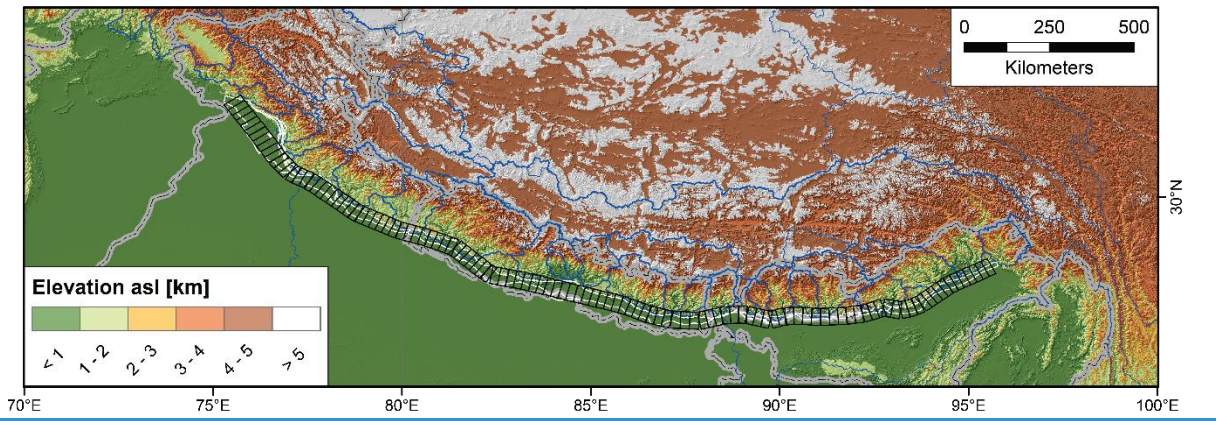

Figure 4.4: A) Mean annual rainfall received in the Himalayas. Note the eastwardly increasing rainfall gradient over the Himalayan foreland. B) Location of 25 km wide, 50 km long swaths used by Hirschmiller (2013) to calculate rainfall, specific stream power, and topography. The Sub-Himalaya is outlined by a white polygon. Images modified from Bookhagen and Burbank (2010)

4.3 Surface Processes Dominate Over Tectonic Processes

It was found that within the model time-frame (i.e. 2 Ma), for a narrow range of parameters, a lateral change in vT and K can result in a wedge that progressively narrows, despite an increasing convergence rate. However, this result can only be achieved for high values of K, such that $1 \times 10^{-5} \leq K \leq 1 \times 10^{-4}$ (Figure 4.4), which is valid for the range of values observed in the Himalayas for D, T and vT (Hirschmiller et al., 2014). Two cases are discussed below; the first

case involves an increase in *K* by a factor of 5, whereas the second case involves an increase in *K* by a factor of 10.

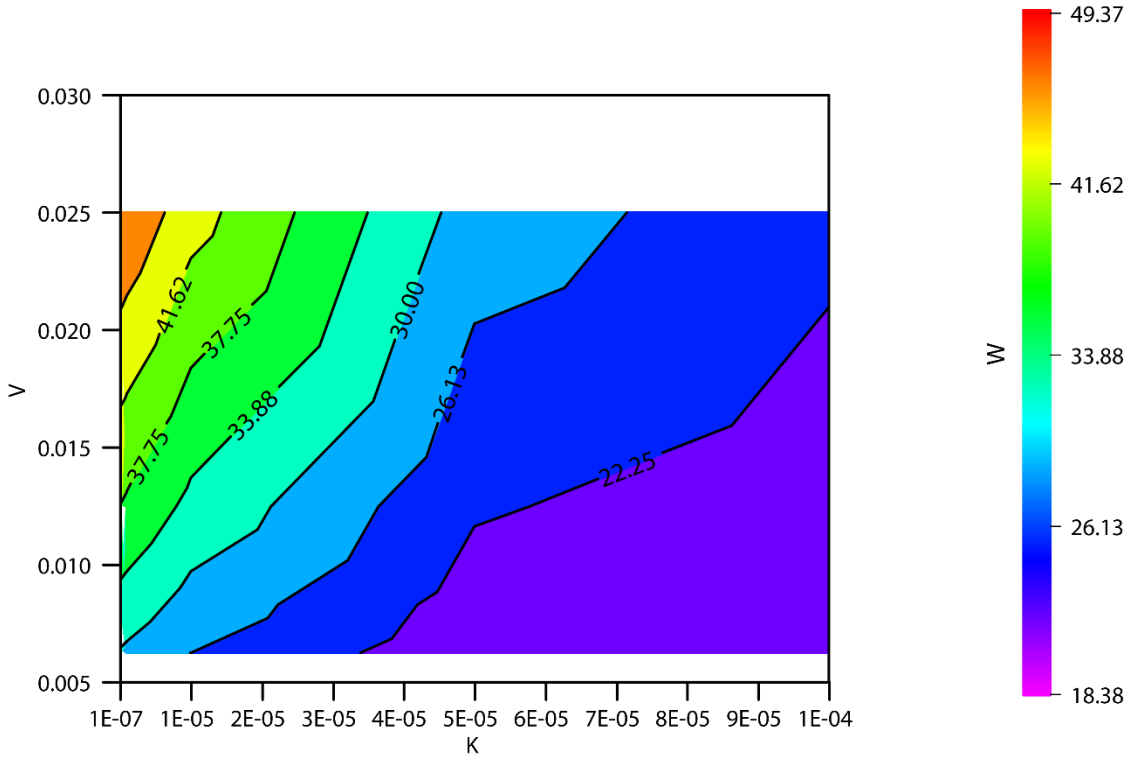

Figure 4.5: Plot of velocity (*v*) versus rock erodibility (*K*). For a given combination of *v* and *K*, expected wedge width (*W*) is shown as coloured zones. For a given velocity, wedge width decreases with increasing *K* along a polynomial function. For very high *K*, the velocity has little influence, whereas for low *K*, the change in velocity dominates, wedge width increases.

4.3.1 Increasing K by a factor of 5

Regardless of the initial velocity, increasing K from 1.0×10^{-5} to 5.0×10^{-5} will result in a FTB that progressively narrows for an increase in velocity by a factor of two (Figure 4.5A and Table 4.1). An increase in velocity by a factor of three also results in a decrease in FTB width, but only for intermediate velocity values (i.e. *v* = 0.0083 m/yr) and the change in width was minor, -0.31 km or -1.9%. With low initial velocity (i.e. v = 0.00625 m/yr), increasing the velocity by a factor of four resulted in an increase in FTB width. This suggests that a threshold value is expected

to be between a factor of 3 and 4, although these preliminary results do not yield an exact threshold value.

Regardless of the initial velocity, an increase in K from $K = 5\times10^{-5}$ to $K = 1.0\times10^{-4}$ produces FTB widths that progressively decrease, provided the velocity increase is less than a factor of two (Figure 4.5A and Table 4.1). If K is increased by a factor of two or more, the wedge will progressively widen. Interestingly, when v = 0.0125 m/yr, doubling the velocity results in a change in width of +0.66 km or 2.91%, whereas when v = 0.00625 m/yr, doubling the velocity results in a change in width of +0.32 km or 1.63%. Furthermore, increases in velocity by a factor of 1.3 and 1.5 also yield progressively narrower FTB widths. This result suggests that a threshold value is expected to lie between a 1.5 and 2. However, more experimental data for a larger range of velocities would need to be collected to test this result.

Table 4.1: Change in FTB width (ΔW) for increasing v and increasing K by a factor of 5.

Increasing K from 5×10^{-5} to 1×10^{-4}			
Velocity Increase (m/yr)	**Factor**	**ΔW (km)**	**ΔW (%)**
From 0.0125 to 0.025	2.0	0.66	2.91
From 0.0083 to 0.0125	1.5	-0.68	-3.29
From 0.0083 to 0.025	3.0	2.66	12.7
From 0.00625 to 0.0083	1.3	-0.78	-3.97
From 0.00625 to 0.0125	2.0	0.32	1.63
From 0.00625 to 0.025	4.0	3.66	18.6
Increasing K from 1×10^{-5} to 5×10^{-5}			
From 0.0125 to 0.025	2.0	-4.64	-14.1

From 0.0083 to 0.0125	1.5	-5.78	-20.3
From 0.0083 to 0.025	3.0	-0.31	-1.09
From 0.00625 to 0.0083	1.3	-5.44	-20.8
From 0.00625 to 0.0125	2.0	-3.44	-13.2
From 0.00625 to 0.025	4.0	2.12	8.12

4.3.2: Increasing K by One Order of Magnitude

For the range of experimental velocity values, increasing *K* by one order of magnitude (from 1×10^{-5} to 1×10^{-4}) results in a wedge that progressively narrows. This was true, regardless of the initial velocity or the factor increase in velocity within the range of values being tested (Table 4.2). For example, for high initial velocity (v = 0.0125 m/yr) an increase in v by a factor of 2 produced a decrease in FTB width of -9.54 km or -29.0%, likewise, an increase in velocity by a factor of 4 produced a decrease in width of -2.78 km or -10.6%.

Table 4.2: **Change in FTB width (Δ*W*) for increasing *v* and increasing *K* by one order of magnitude.**

Increasing K from 1×10^{-5} to 1×10^{-4}			
Velocity (m/yr)	**Factor**	**Δ*W* (km)**	**Δ*W* (%)**
From 0.0125 to 0.025	2.0	-9.54	-29.0
From 0.0083 to 0.0125	1.5	-8.55	-29.9
From 0.0083 to 0.024	3.0	-5.21	-18.3
From 0.00625 to 0.0083	1.3	-7.22	-27.7
From 0.00625 to 0.0125	2.0	-6.12	-23.4
From 0.00625 to 0.025	4.0	-2.78	-10.6

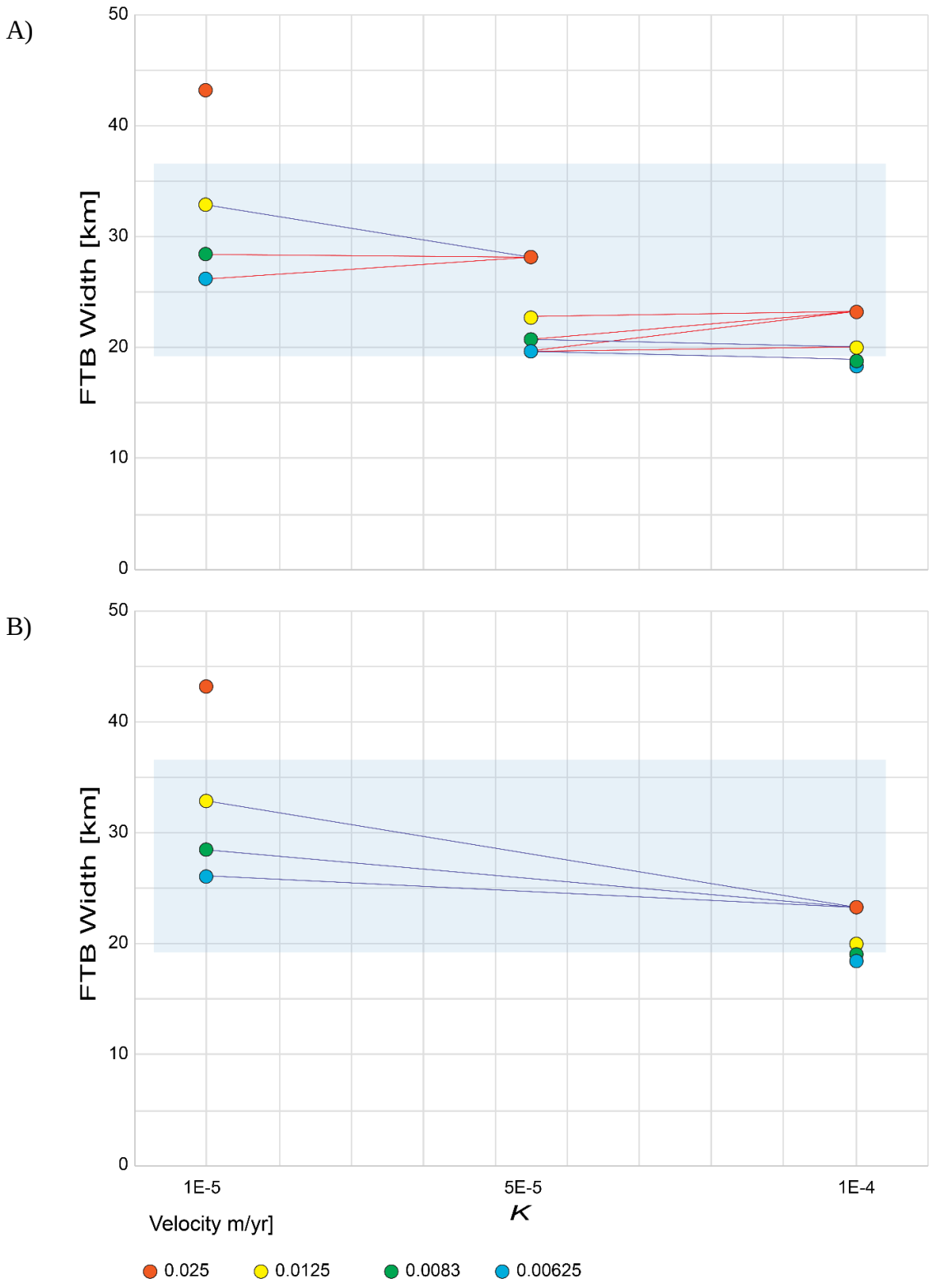

Figure 4.6: Plots of FTB width (*W*) versus the rock erodibility constant (*K*) for A) an increase in *K* by a factor of 5, and B) and increase in *K* by one order of magnitude. Coloured dots correspond to different velocity values (*v*), red lines indicate combinations of *v* and *K* that result in an increase in wedge width, whereas black lines correspond to combinations of *v* and *K* that result in a decrease in wedge width.

5.0 Conclusions

The numerical experiments performed in this study have reproduced the key morphological parameters of the Himalayan FTB, within the range of the controlling parameters observed in nature. For the mean accreted sediment thickness (T) of 6000 m, sole-out depth (D) of 8000 m, convergence rate (v) of 0.0083 m/yr, accretion flux (vT) of 50 m^2/yr, and rock erodibility constant (K) of 5×10^{-5}, the models yield a width (W) of the Himalaya FTB in the range of 19.7 km to 28.4 km within a duration of 2-3 Ma. Analysis of the critical taper angles suggest that the pore fluid pressure ratio within the Himalayan FTB ranges between $\lambda = 0.5$ and $\lambda = 0.97$.

These results are in accord with the generic conclusions of Hilley and Strecker (2004) and Hilley et al. (2004). However, this study argues that the Himalaya FTB (i.e. the active segment of the Himalaya) is not equivalent to the Himalayan orogenic wedge. The latter has evolved over 50 Ma, through a combination of different crustal processes, and therefore its finite geometry cannot be assumed to have evolved solely through the mechanics of a Coulomb frictional wedge. As a result, the absolute values of the parameters differ from those used in previously published experiments.

This study suggests that for a narrow range of parameter values, orogen-parallel variations in erosion rate can dominate over orogen-parallel variations in accretion flux in controlling CCW width. Convergence rates and shortening rates both increase from west to east along-strike of the Himalayan FTB by a factor of approximately 2. The experimental results obtained from this study suggest that along the strike of the Himalayan FTB, the value of K varies by approximately one order or magnitude of less. Keeping other parameters constant (D and T), the numerical

experiments from this study yield FTB widths that decrease from west to east within the range of observed widths in the Himalayan FTB

Although we can use K to approximate climatically controlled erosion rate in the Himalayan FTB, a mathematical relationship between mean annual precipitation (MAP) or specific stream power (SSP) and K needs to be established in order to convert MAP and/or SSP directly to K. Establishing such a mathematical relationship will verify how well this numerical model is able to quantify the interactive relationship between tectonic and surface processes in the Himalayan FTB. Furthermore, parameters representing surface processes (k_a, h, m and n) need to be determined for the Himalayan FTB, as opposed to the Himalayan orogenic wedge, as is currently the case in the literature. Finally, geophysical data must be analysed to directly constrain the décollement angle (β) and the sole-out depth (D) for the Himalayan FTB.

References

Acharyya, S.K., 1994, The Cenozoic foreland basin and tectonics of the eastern Sub-Himalaya: Problems and prospects. *Him. Geol*.; v. 15; p. 3-21.

Auden, J.B., 1935. Traverses in the Himalaya. Geological Survey of Indian Record; v. 69, p. 123-167

Avouac, J.P., 2003, Mountain building, erosion, and the seismic cycle in the Nepal Himalaya. *Advances in Geopgysics*; v. 46; p. 1-80; doi: 10.1016/S0065-2687(03)46001-9

Beaumont, C., Fullsack, P., Hamilton, J., 1992, Erosional control of active compressional orogens. *In* McClay, K.R., ed., Thrust tectonics: New York, Chapman and Hall, p. 1-18.

Bernet, M., van der Beek, P., Pik, R., Huyghe, P., Mugnier, J.L., Labrin, E, Szulc, A., 2005, Miocene to recent exhumation of the central Himalaya determined from combineddetrital zircon fission-track and U/Pb analysis of Siwalik sediments, western Nepal. *Basin Res.*; v. 18;no. 4; p. 393-412.

Bilotti, F., Shaw, J.H., 2005, Deep-water Niger Delta fold-and-thrust belt modeled as a critical-taper wedge; the influence of elevated basal fluid pressure on structural styles. *AAPG Bulletin*; v. 89; no. 11; pp. 1475–1491.

Bookhagen, B., Burbank, D.W., 2010, Toward a complete Himalayan hydrological budget: Spatiotemporal distribution of snowmelt and rainfall and their impact on river discharge. *J. Geol. Res.*; v. 115, F03019, doi: 10.1029/2009JF001426.

Chirouze, F., Huyghe, P., van der Beek, P., Chauvel, C., Chakraborty, T., Dupont-Nivet, G., Bernet, M., 2013, Tectonics, exhumation, and drainage evolution of the eastern Himalaya since 13 Ma from detrital geochemistry and thermochronology, Kameng River Section, Arunachal Pradesh. *Geol. Soc. Am. Bull.*; v. 125; no. 3-4; p. 523-538; doi: 10.1130/B30697.1

Chirouze, F., Dupont-Nivet, G., Huyghe, P., van der Beek, P., Chakraborti, T., Bernet, M., and Erens, V., 2012, Magnetostratigraphy of the Neogene Siwalik Group in the far eastern Himalaya: Kameng section, Arunachal Pradesh, India: *J. Asian Earth Sci.*; v. 44; no. C; p. 117–135; doi: 10.1016/j.jseaes.2011.05.016.

Dahlen, F.A. (1990), Critical Taper Model of Fold-and-Thrust Belts and Accretionary Wedges, *Annu. Rev. Earth Planet Sci*., 18:55-99.

Dahlen, F.A., Barr, T.D., 1989, Brittle frictional mountain building 1. Deformation and mechanical energe budget. *J. Geophys. Res.*; v. 94; no. B4; p. 3906-3922.

Dahlen, F. A., 1984, Noncohesive critical Coulomb wedges: An exact solution. *J. Geophys. Res.*; v. 89, no. B12, p. 10125.

Davis, D., Suppe, J., Dahlen, F.A., 1983, Mechanics of fold-and-thrust belts and accretionary wedges. *J. Geophys. Res*.; v. 88; no. B2; p. 1153-1172.

DeCelles, P.G., DeCelles, P.C., 2001, Rates of shortening, propagation, underthrusting and flexural wave migration in continental orogenic systems, *Geology*; v. 29; p. 135-138

DeCelles, P.G., Robinson, D.M., Quade, J., Ojha, T.P., 2001, Stratigraphy, structure and tectonic evolution of the Himalayan fold-thrust belt in Western Nepal: *Tectonics*, v. 20, p. 487-509.

DeCelles, P.G., Cavazza, W., 1999, A comparison of fluvial megafns in the Cordilleran (Upper Cretaceous) and modern Himalayan foreland basin systems. *Geol. Soc. Am. Bull.*; v. 111; no. 9; p. 1315-1334; doi: 10.1130/0016-7606(1999)111.

DeCelles, P.G., Gehrels, G.E., Quade, J., Ojha, T.P., 1998, Eocene-early Miocene foreland basin development and the history of Himalayan thrusting, western and central Nepal. *Tectonics*; v. 17; no. 5; p. 741-765.

Gansser, A, 1964, Geology of the Himalayas, London: Wiley Interscience Publishers

Garzanti, E., 1999, Stratigraphy and sediment history of the Nepal Tethys passive margin. *J. Asian Earth Sci.*; v. 17; p. 805-827.

Hack, J.T., 1957, Studies of longitudinal stream profiles in Virginia and Maryland. *U.S. Geol. Surv. Prof. Pap.*; p. 47-97.

Hilley, G. E., and Strecker, M. R., 2004a, Growth and erosion of fold-and-thrust belts with an application to the Aconcagua fold-and-thrust belt, Argentina: *J. Geophys. Res.*; v. 109, B01410, doi: 10.1029/2002JB002282.

Hilley, G. E., and Strecker, M. R., 2004b, Steady state erosion of critical Coulomb wedges with application to Taiwan and the Himalya. *J. Geophys. Res.*; v. 109, no. B01411, p. doi: 10.1029/2002JB002284.

Hirschmiller, J., Grujic, D., Bookhagen, B., Coutand, C., Huyghe, P., Mugnier, J. L., and Ojha, L., 2014. What controls the growth of the Himalayan foreland fold-and-thrust belt? *Geology*; doi: 10.1130/G35057.1

Hirschmiller, J, 2013, Pliocene to recent shortening of the Siwalik Group in the Himalayan foreland belt (Unpublished honours thesis). Dalhousie University, Canada.

Hodges, K.V., 2000, Tectonics of the Himalaya and southern Tibet from two perspectives. *Geol. Soc. Am. Bull.*; v. 112; no. 3; p. 324-350

Howard, A.D., Dietrich, W.E., Seidl, M.A., 1994, Modeling fluvial erosion on regional to continental scales. *J. Geophys. Res.*; v. 99; no. B7; p. 13,971-13,986.

Hubbert, M. King, and William W. Rubey. 1959, Role of fluid pressure in mechanics of overthrust faulting I. Mechanics of fluid-filled porous solids and its application to overthrust faulting, *Geol. Soc. Am. Bull.*; v. 70; no. 2; p. 115-166.

Jaeger, J.C., Cook, N.G.W., 1979, Fundamentals of rock mechanics, third edition, London: Chapman and Hall Ltd.

Kellett, D.A., Grujic, D., 2012, New insight into the South Tibetan detachment system: not a single prrgressive deformation. *Tectonics*; v. 31, TC2007; doi: 10.1029/2011TC002957.

Kellett, D.A., Grujic, D., Warren, C., Cottle, J., Jamieson, R., Tenzin, T., 2010, Metamorphic history of a syn-convergent orogen-parallel detachment: The South Tibetan detachment system, Bhutan Himalaya. *J. Metamorph. Geol.*; v. 28; p. 785-808; doi: 10.1111/j.1525-1314.2010.00893.x.

Long, S., McQuarrie, N., Tobgay, T., Grujic, D., 2011a, Geometry and crustal shortening of the Himalayan fold-thrust belt, eastern and central Bhutan. *Geol. Soc. Am. Bull*; v. 123; no. 7-8; p. 1427-1447

Long, S., McQuarrie, N., Tobgay, T., Rose, C., Gehrels, G., Grujic, D., 2011b, Tectonostratigraphy of the Lesser Himalaya of Bhutan: Implications for the along-strike tratigraphic continuity of the northern Indian margin. *Geol. Soc. Am. Bull;* v. 123; no. 7-8; p. 1406-1426; doi: 10.1130/B30202.1

Mugnier, J.L., Huyghe, P., Leturmy, P., Jouanne, F., 2004, Episodicity and rates of thrust sheet motion in Himalaya (western Nepal). *In* McClay, K.R., ed., Thrust tectonics and hydrocarbon systems; *Mem. Am. Assoc. Pet. Geol.*; v. 82; p. 91-114.

Mugnier, J.L., Leturmy, P., Mascle, G., Huyghe, P., Chalaron, E., Vidal, G., Husson, L., and Delcaillau, B., 1999a, The Siwaliks of western Nepal: I. Geometry and kinematics. *J. Asian Earth Sci.*; v. 17, no. 5, p. 629–642.

Mugnier, J.L., Leturmy, P., Huyghe, P., Chalaron, E., 1999b, The Siwaliks of western Nepal II. Mechanics of the thrust wedge. . *J. Asian Earth Sci.*; vol. 17; p. 643-657.

Najman, Y., 2006, The detrital record of orogenesis: A review of approaches and techniques used in the Himalayan sedimentary basins. *Earth Sci. Rev.*; v. 74; p. 1-72; doi: 10.1016/j.earscirev.2005.04.004.

Najman, Y., Johnson, K., White, N., and Oliver, G., 2004, Evolution of the Himalayan foreland basin, NW India. *Basin Res.*, v. 16, p. 1-24, doi: 10.1111/j.1365-2117.2003.00223.x.

Nakayma, K., Ulak, P.D., 1999, Evolution of fluvial style in the Siwalik Group in the foothills of the Nepal Himalaya. *Sediment. Geol.*; v. 125; p. 205-224.

Nelson, K.D., Zhao, W., Brown, L.D., Kuo, J., Che, J., Liu, X., Kind, R., Wenzel, F., Ni, J., Nabelek, J., Leshou, C., Tan, H., Wei, W., Jones, A.G., Booker, J., Unsworth, M., Kidd, W.S.F., Hauck, M., Alsdorf, D., Ross, A., Cogan, M., Wu, C., Sandvol, E., Edwards, M., 1996, Partially molten middle crust beneath southern Tibet: Synthesis of project INDEPTH results. *Science*; v. 274; p. 1684-1688.

Ojha, T.P., Butler, R.F., DeCelles, P.G., and Quade, J., 2009, Magnetic polarity Stratigraphy of the Neogene foreland basin deposits of Nepal. *Basin Res.*; v. 21; no. 1; p. 61–90; doi: 10.1111/j.1365U2117.2008.00374.x.

Robinson, D.M., DeCelles, P.G., Patchett P.J., Garzione, C.N., 2001, The kinematic evolution of the Nepalese Himalaya interpreted from Nd isotopes. *Earth Planet. Sci. Lett.*; v. 192, p. 507-521

Searle, M.P., Law, R.D., Godin, L., Larson, K.P., Streule, M.J., Cottle, J.M., Jessup, M.J., 2008, Defining the Himalayan Main Central Thrust in Nepal. *J. Geol. Soc. London*; v. 165; p. 523-534: doi: 10.1144/0016-76492007-081.

Stock, J.D., Montgomery, D.R., 1999, Geologic constraints on bedrock river incision using the stream power law. *J. Geophys. Res.*; v. 104; no. B3; p. 4983-4993.

van der Beek, P., Robert, X., Mugnier, J.L., Bernet, M., Huyghe, P., Labrin, E., 2006, Late Miocene- recent exhumation of the central Himalaya and recycling in the foreland basin assessed by apatite fission-track thermochronology of Siwalik sediments, Nepal. *Basin Res.*; v. 18; p. 413-434; doi: 10.1111/j.1365-2117.2006.00305.x.

Warren, C.J., Grujic, D., Kellett, A., Cottle, J., Jamieson. R.A., Ghalley, K.S., 2011, Probing the depths of the India-Asia collision: U-Th-Pb monazite chronology of granulites from NW Bhutan. *Tectonics*; v. 30; TC2004; doi: 10.1029/2010TC002738.

Whipple, K. X., 2009, The influence of climate on the tectonic evolution of mountain belts. *Nat. Geosci.*; v. 2, no. 2, p. 97-104.

Whipple, K.X., Tucker, G.E., 2002, Implications of sediment-flux-dependent river incision models for landscape evolution. *J. Geophys. Res.*; v. 107; no. B2; doi: 10.1029/2000JB000044.

Whipple, K.X., Hancock, G.S., Anderson, R.S., 2000, River incision into bedrock: Mechanics and relative efficacy of plucking abrasion, and cavitation. *Geol. Soc. Am. Bull.*, v. 112; p. 490-503.

Whipple, K. X., and Tucker, G. E., 1999, Dynamics of the stream-power river incision model: Implications for height limits of mountain ranges, landscape response timescales, and research needs. *J. Geophys. Res.*; v. 104, no. B8, p. 17,661-617,674.

Willett, S., Beaumont, C., Fullsack, P., 1993, Mechanical model for the tectonics of doubly vergent compressional orogens. *Geology*; v. 21; p. 371-374; doi: 10.1130/0091-7613(1993)021<0371:MMFTTO>2.3.CO;2.

Yin, A., 2006, Cenozoic tectonic evolution of the Himalayan orogen as constrained by along-strike variation of structural geometry, exhumation history, and foreland sedimentation. *Earth Sci. Rev.*; v. 76; p. 1-131; doi: 10.1016/j.earscirev.2005.05.004.

Appendices

Appendix A: Experiments for k_a = 4, h = 1.4

Variation in Sole-Out Depth (D)

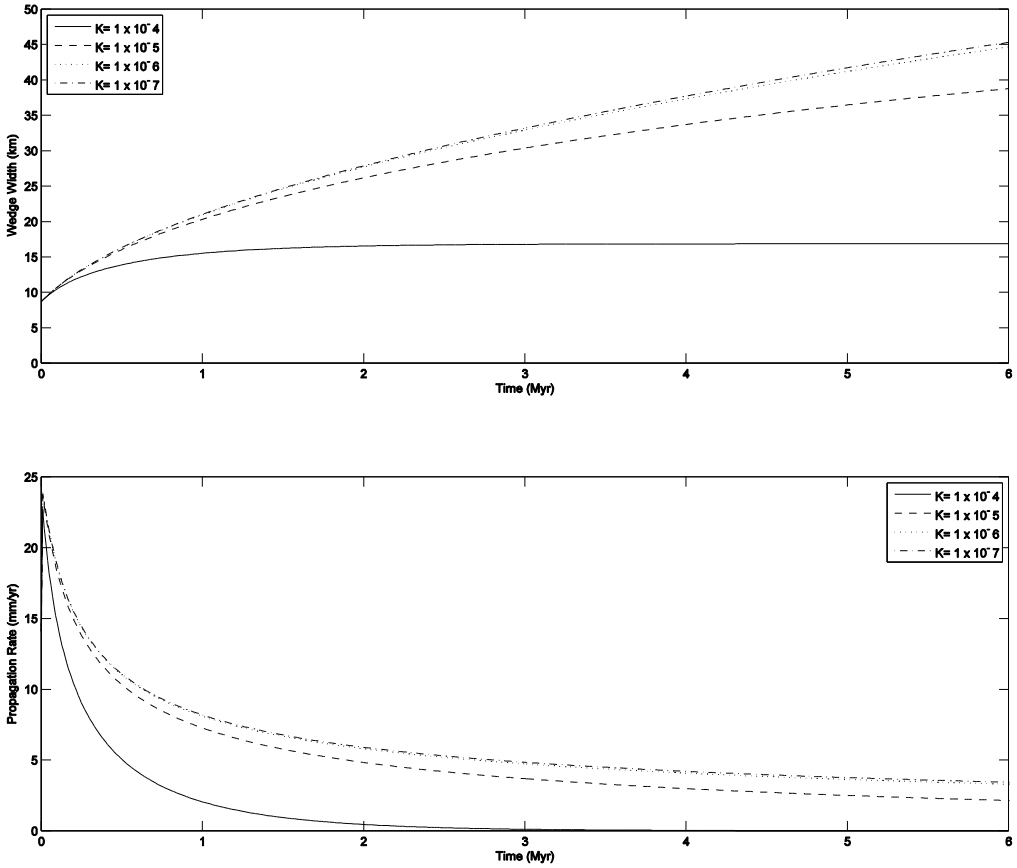

Figure A1: **Effects of varying sole-out depth (D) on (A) wedge width and (B) wedge propagation rate, for D = 4000m.**

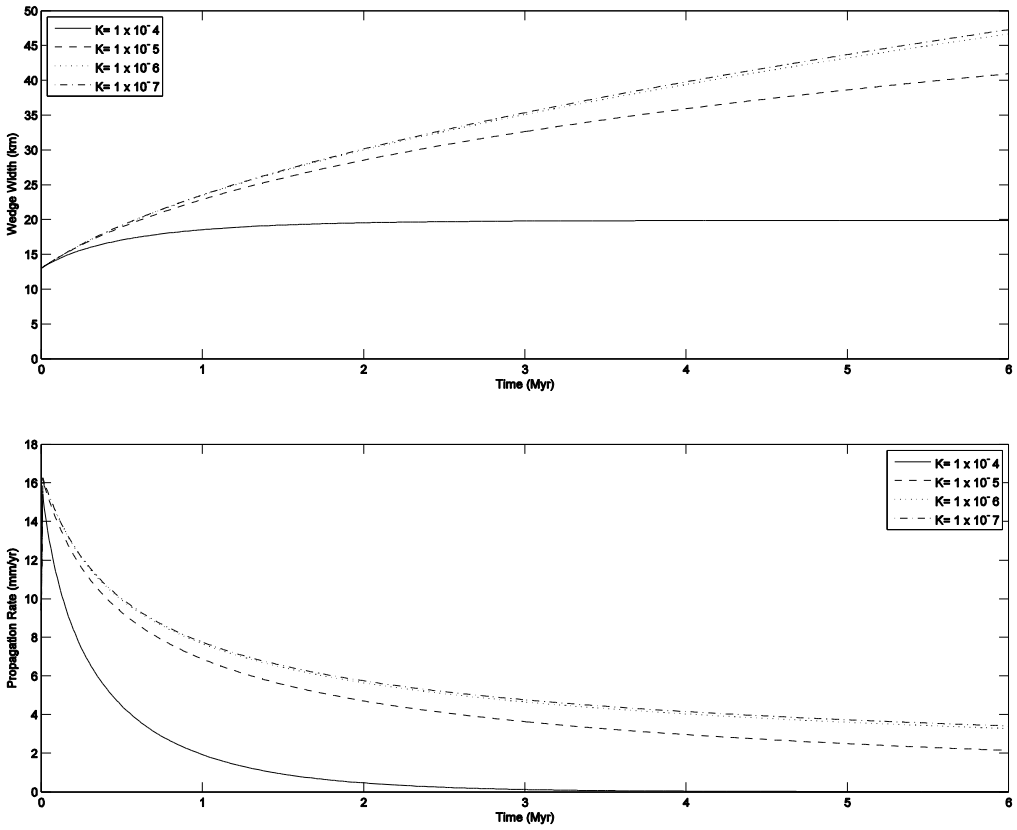

Figure A2: **Effects of varying sole-out depth (D) on wedge width (A) and wedge propagation rate (B), D = 6000m.**

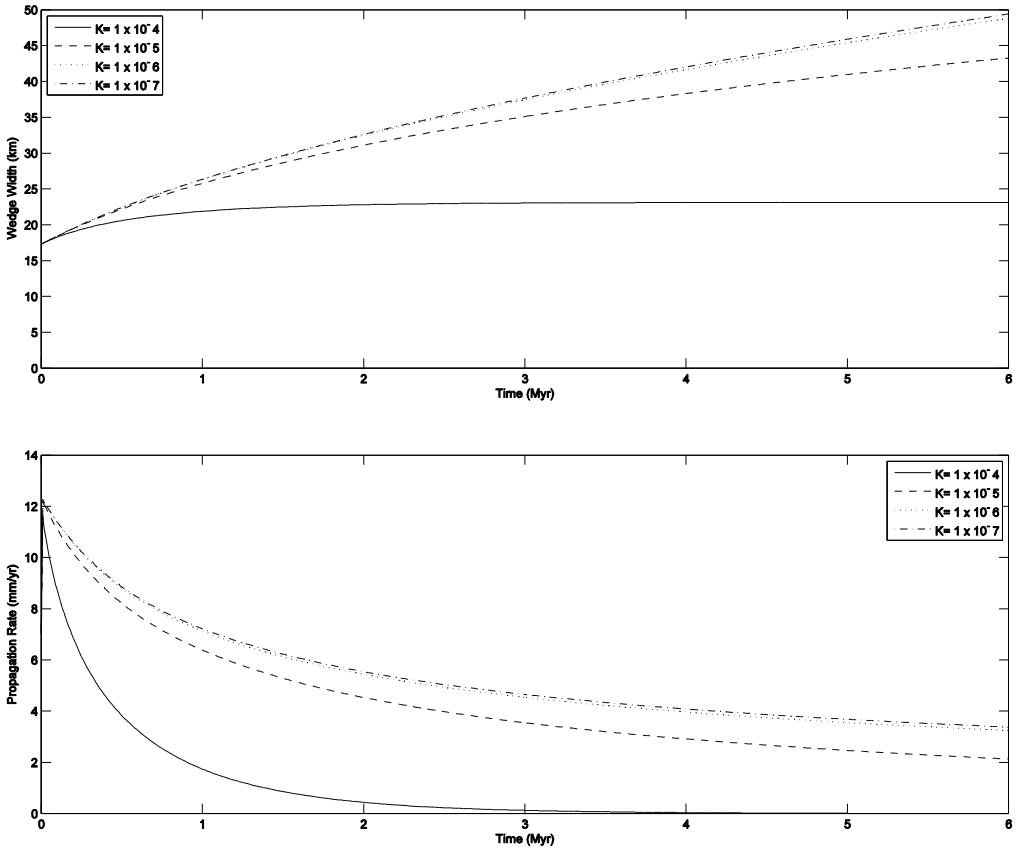

Figure A3: **Effects of varying sole-out depth (D) on wedge width (A) and wedge propagation rate (B), D = 8000m.**

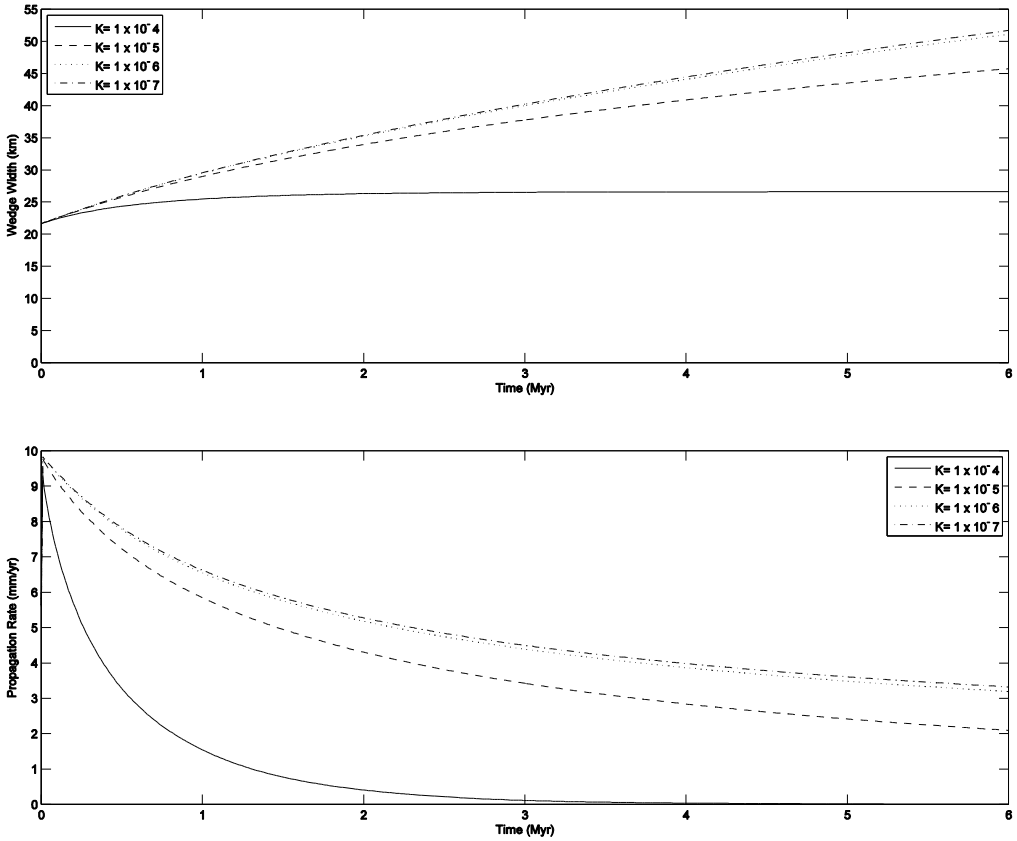

Figure A4: **Effects of varying sole-out depth (D) on wedge width (A) and wedge propagation rate (B), D = 10000m.**

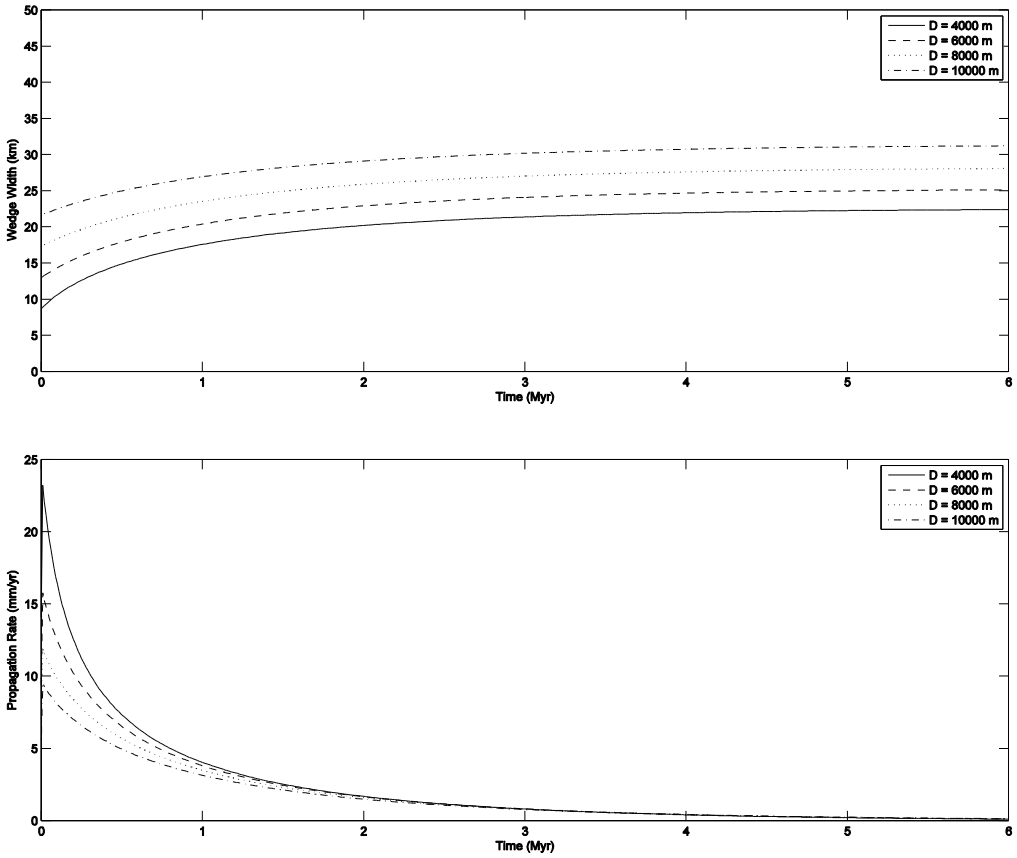

Figure A5: **Effects of varying sole-out depth (D) on wedge width (A) and wedge propagation rate (B), K = 5×10^{-5}.**

Variation in Sediment Thickness (T)

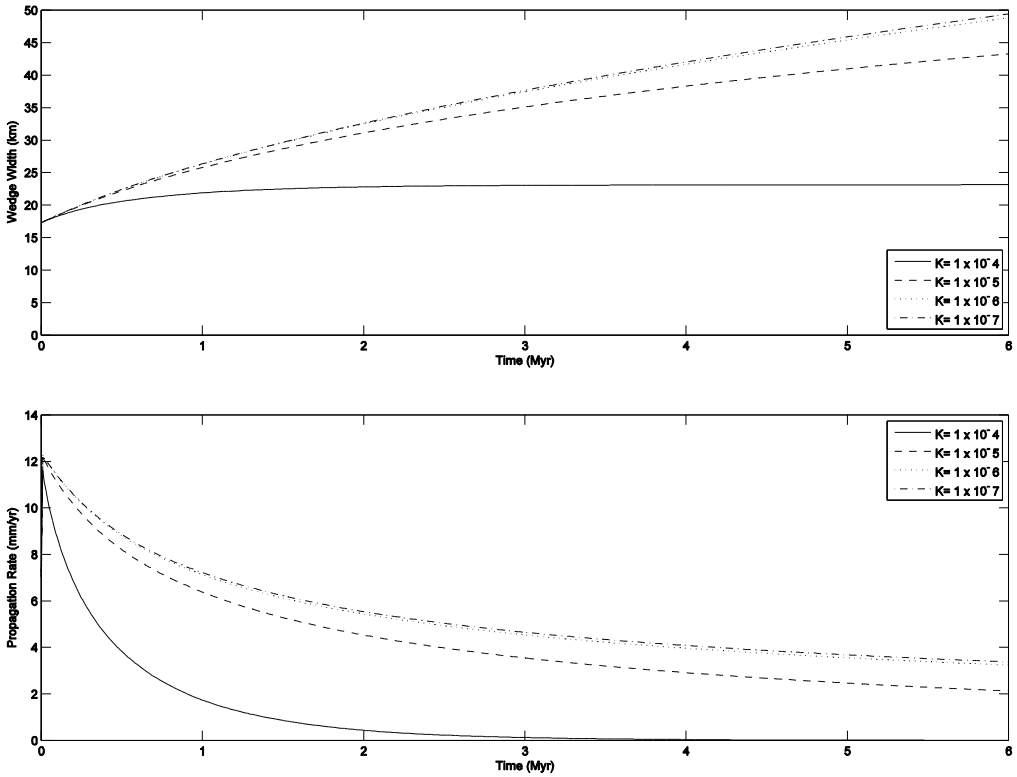

Figure A6: **Effect of varying sediment thickness (*T*) on wedge width (A) and wedge propagation rate (B), T = 2000 m, *v* = 0.025 m/yr.**

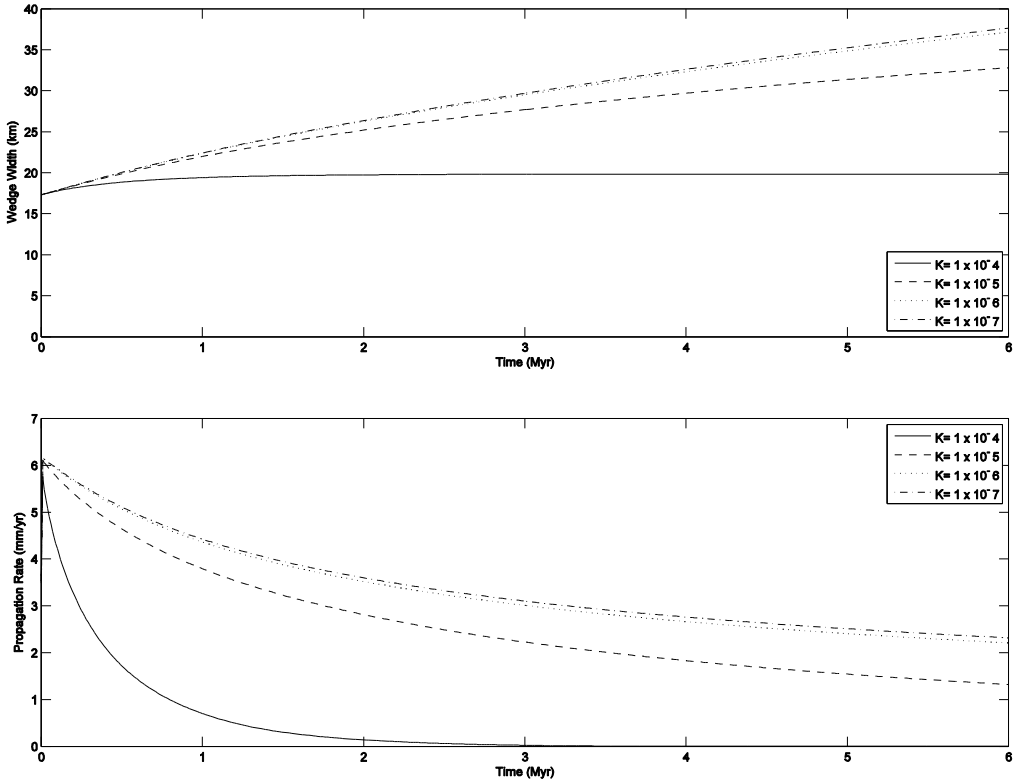

Figure A7: **Effect of varying sediment thickness (*T*) on wedge width (A) and wedge propagation rate (B), *T* = 2000 m, *v* = 0.0125 m/yr.**

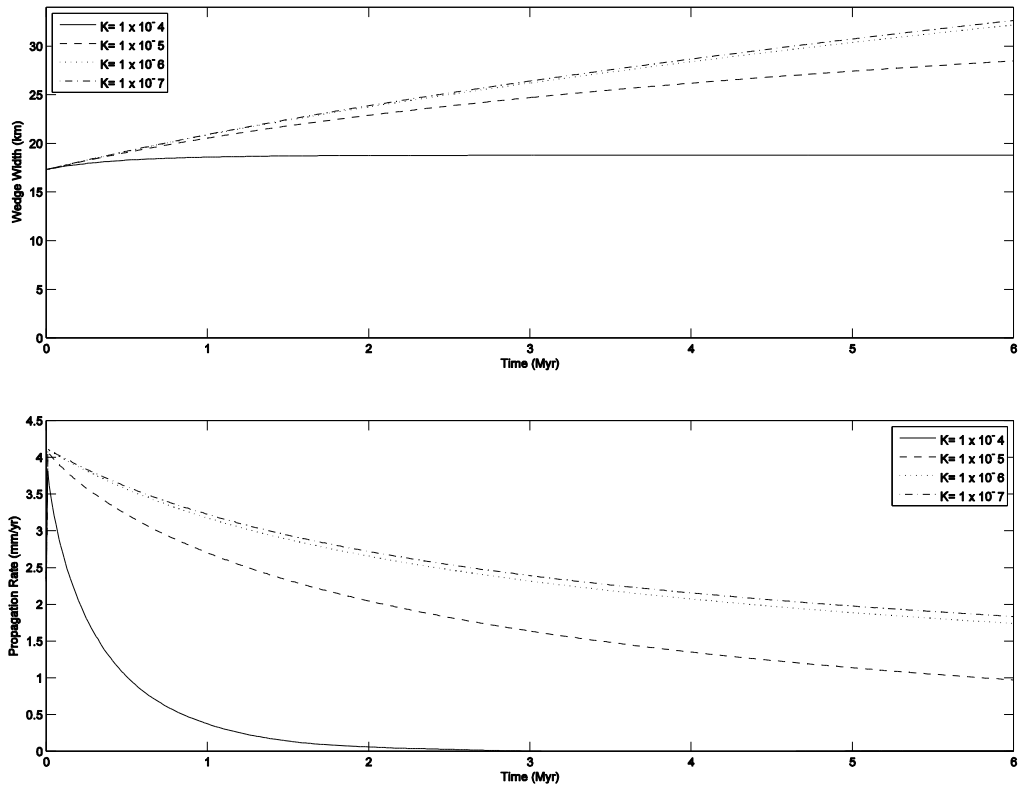

Figure A8: **Effect of varying sediment thickness (*T*) on wedge width (A) and wedge propagation rate (B), *T* = 2000 m, v = 0.0083 m/yr.**

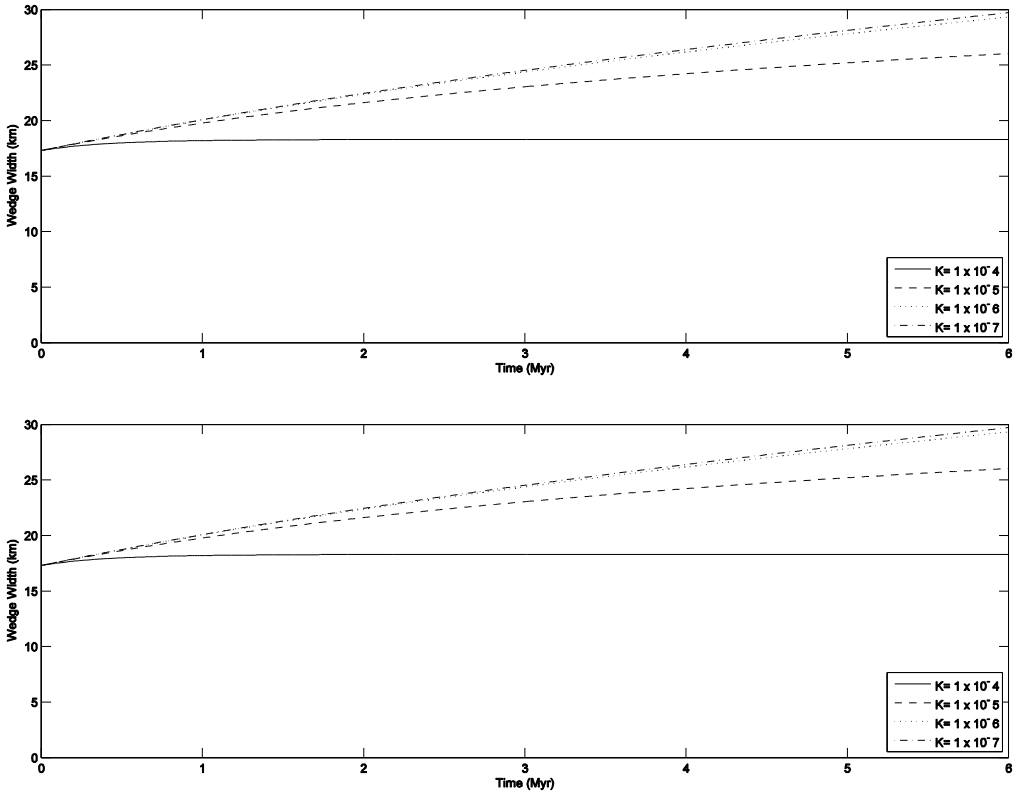

Figure A9: **Effect of varying sediment thickness (*T*) on wedge width (A) and wedge propagation rate (B), *T* = 2000 m, *v* = 0.00625 m/yr.**

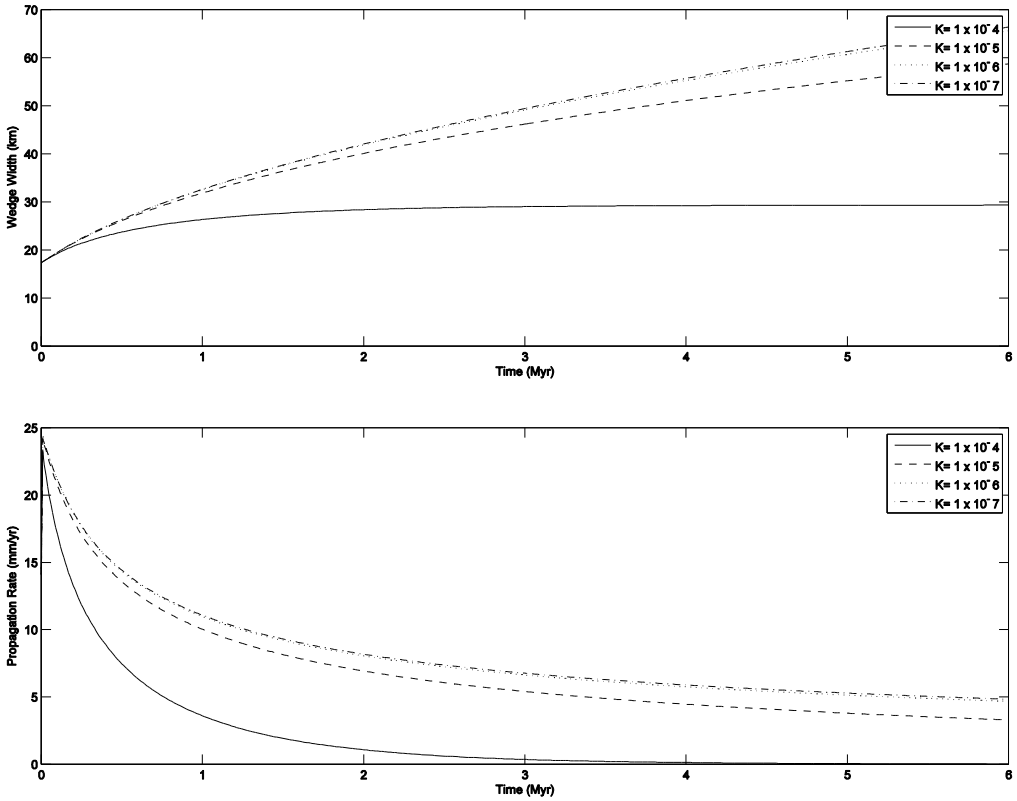

Figure A10: **Effect of varying sediment thickness (*T*) on wedge width (A) and wedge propagation rate (B), *T* = 4000 m, *v* = 0.025 m/yr.**

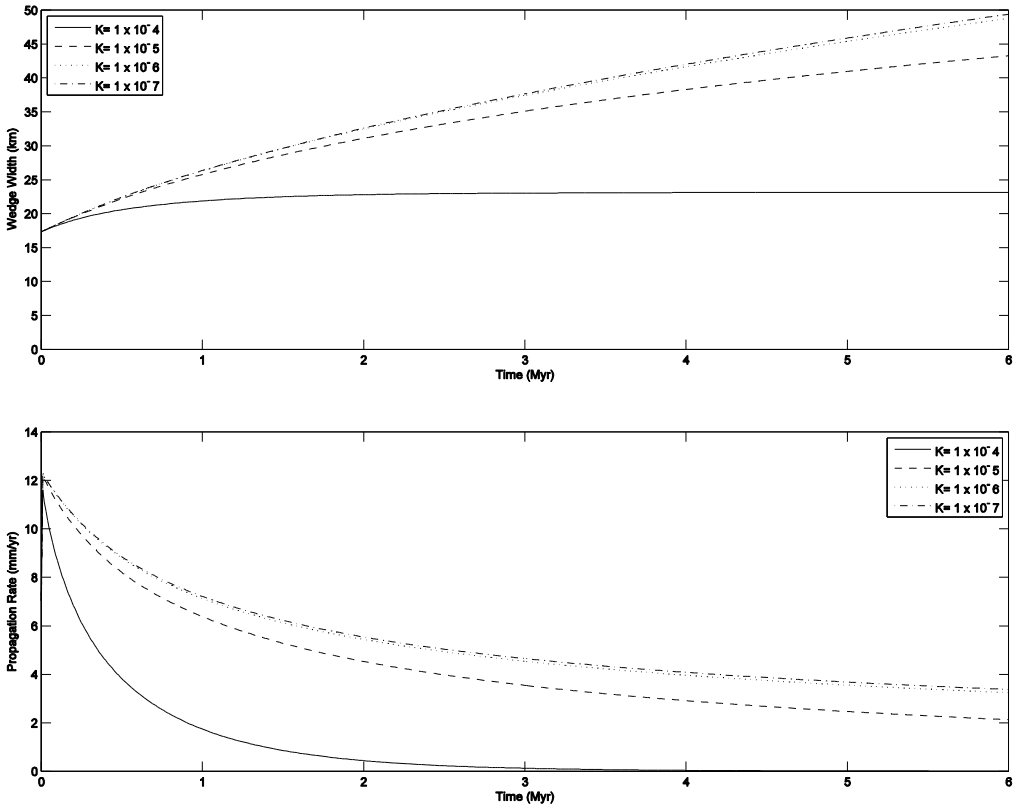

Figure A11: **Effect of varying sediment thickness (*T*) on wedge width (A) and wedge propagation rate (B), *T* = 4000 m, *v* = 0.0125 m/yr.**

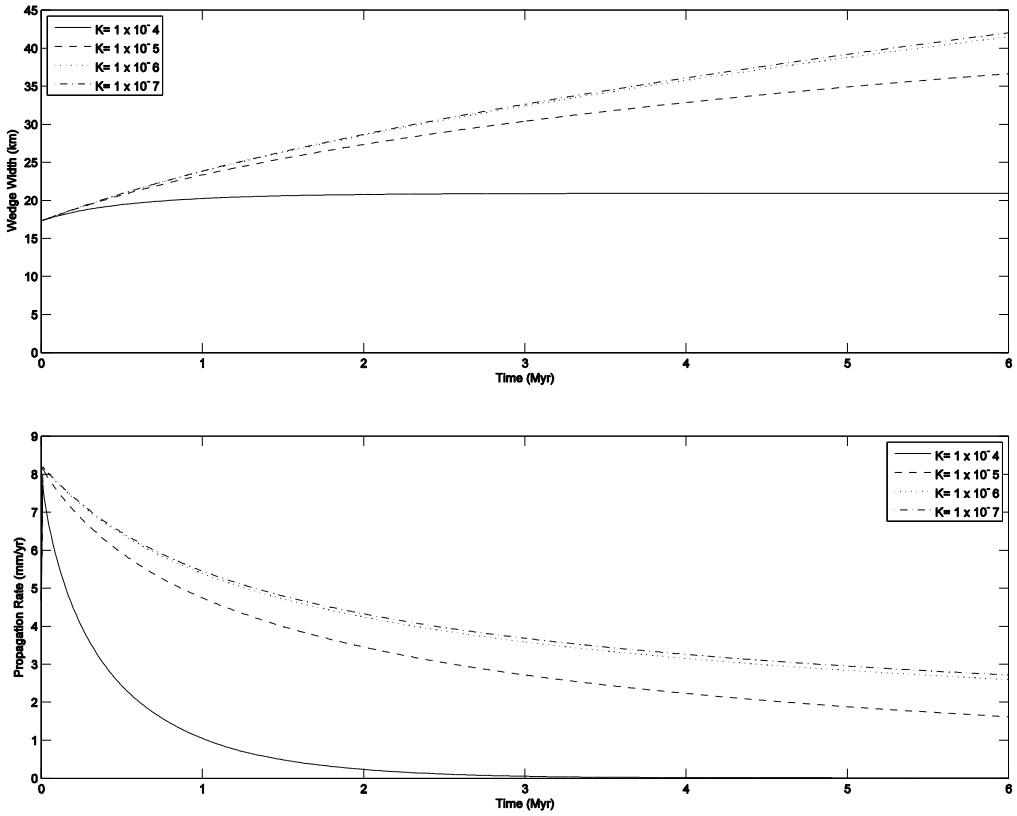

Figure A12: **Effect of varying sediment thickness (*T*) on wedge width (A) and wedge propagation rate (B), *T* = 4000 m, *v* = 0.0083 m/yr.**

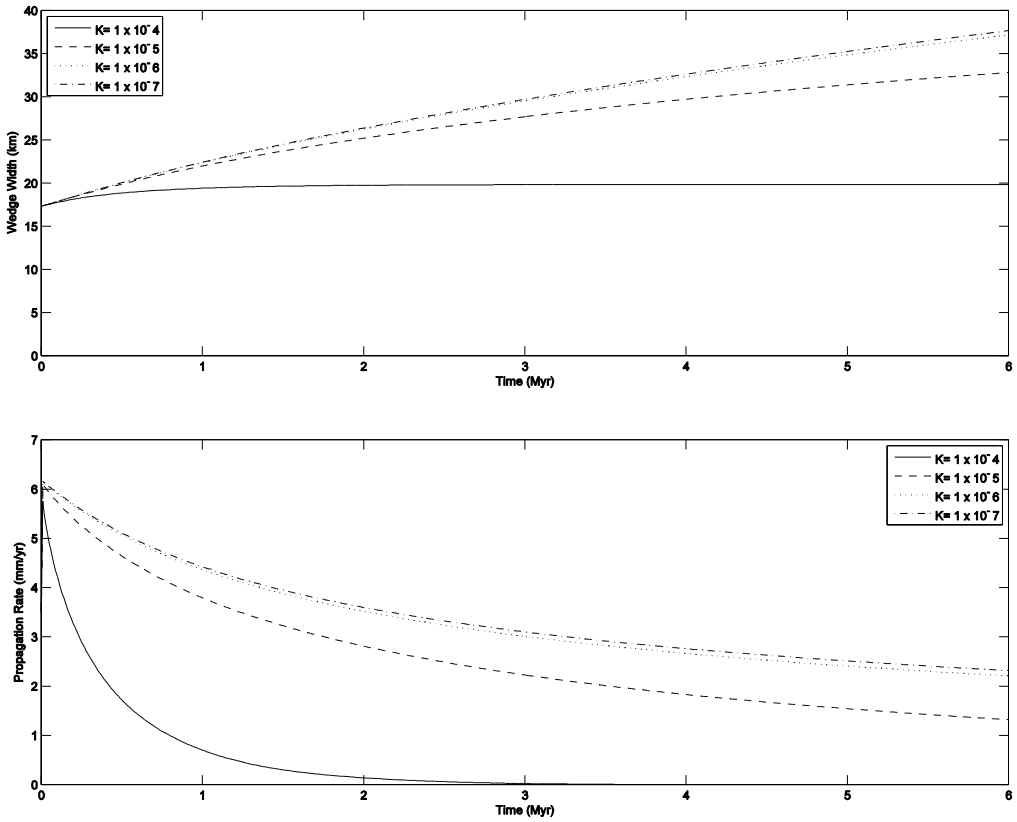

Figure A13: **Effect of varying sediment thickness (*T*) on wedge width (A) and wedge propagation rate (B), *T* = 4000 m, *v* = 0.00625.**

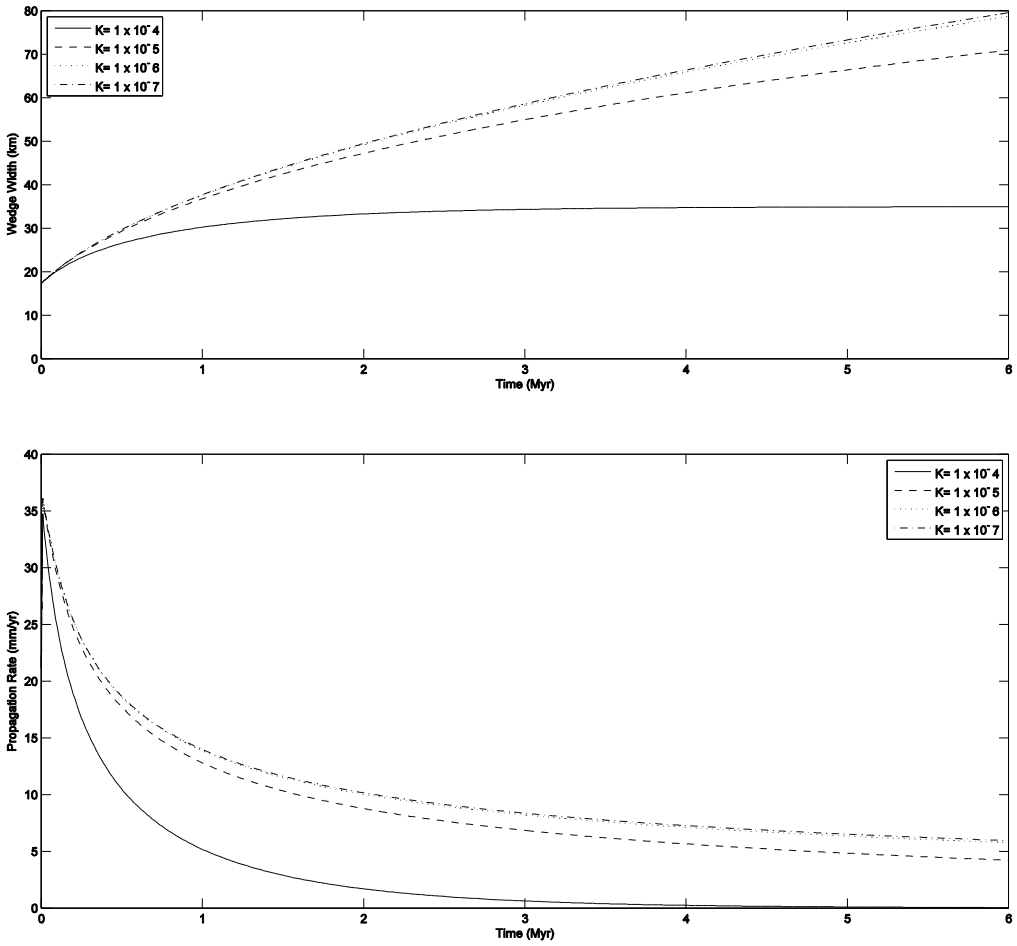

Figure A14: **Effect of varying sediment thickness (*T*) on wedge width (A) and wedge propagation rate (B), *T* = 6000 m, *v* = 0.025 m/yr.**

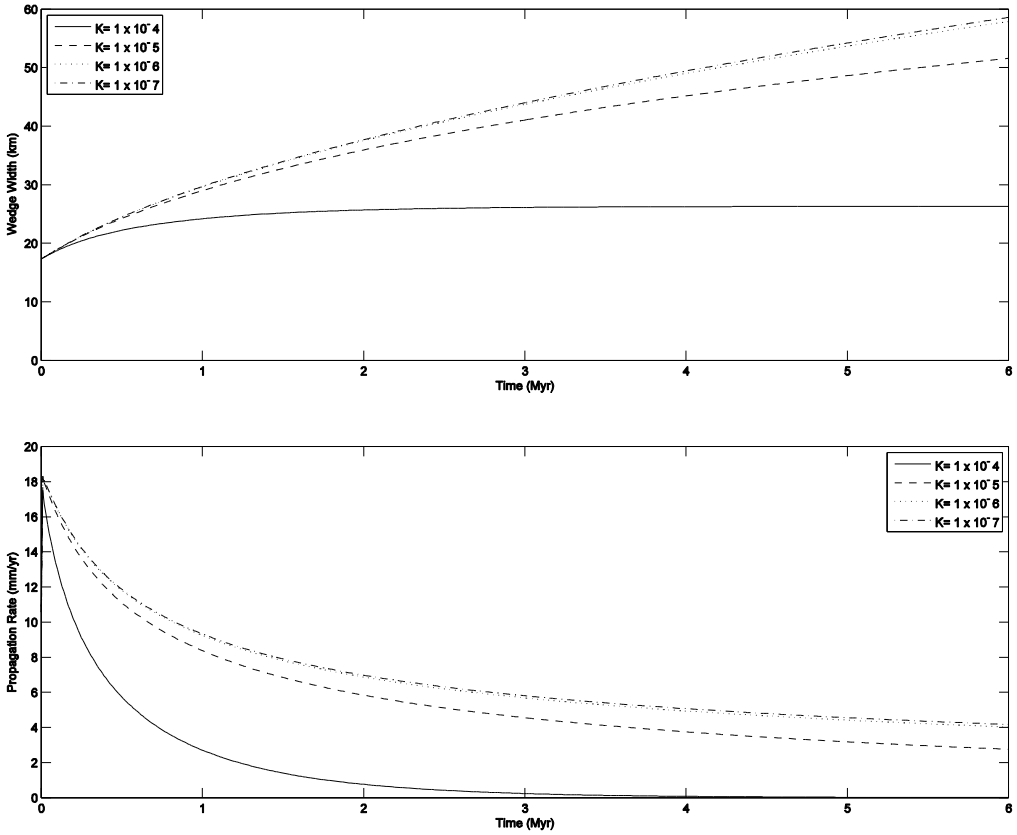

Figure A15: **Effect of varying sediment thickness (*T*) on wedge width (A) and wedge propagation rate (B), *T* = 6000 m, *v* = 0.00125 m/yr.**

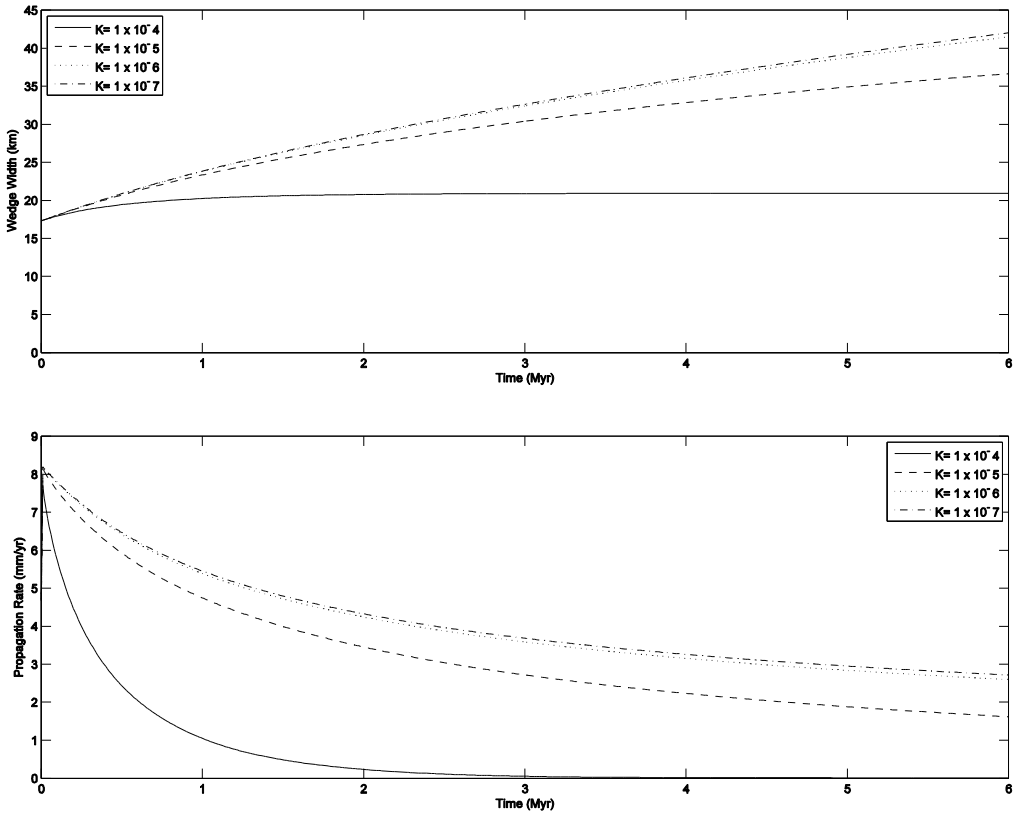

Figure A16: **Effect of varying sediment thickness (*T*) on wedge width (A) and wedge propagation rate (B), *T* = 6000 m, *v* = 0.0083 m/yr.**

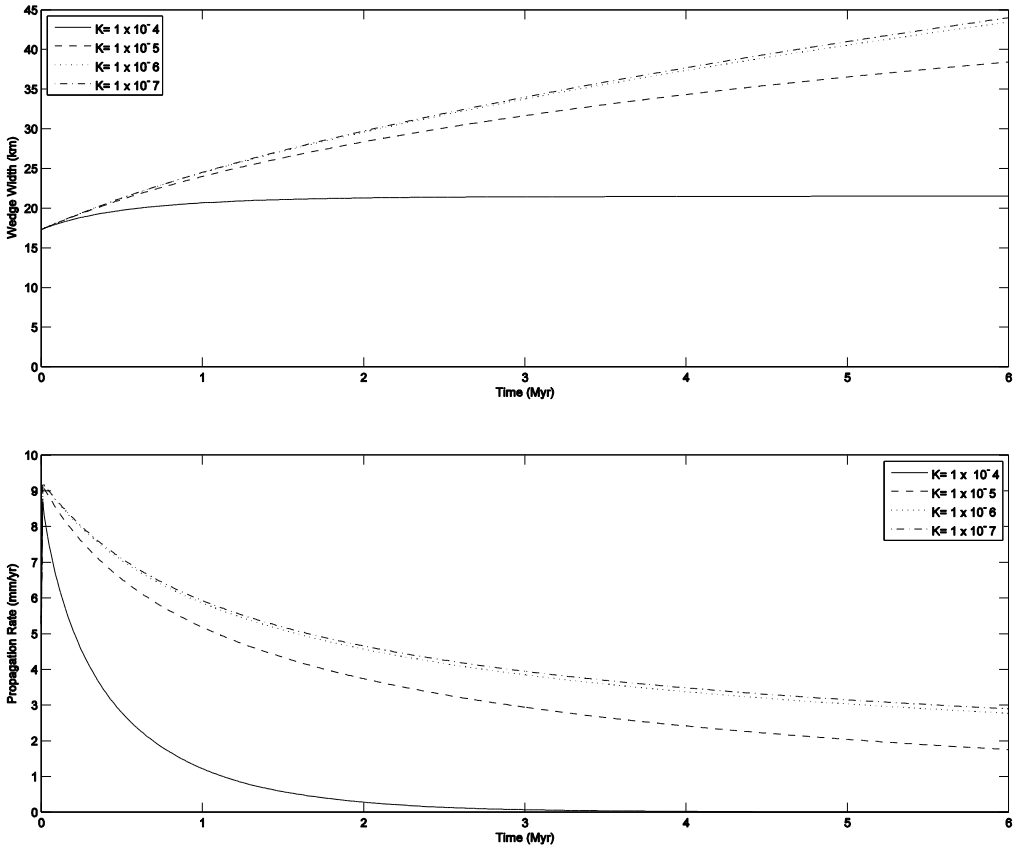

Figure A17: **Effect of varying sediment thickness (*T*) on wedge width (A) and wedge propagation rate (B), *T* = 6000 m, *v* = 0.00625 m/yr.**

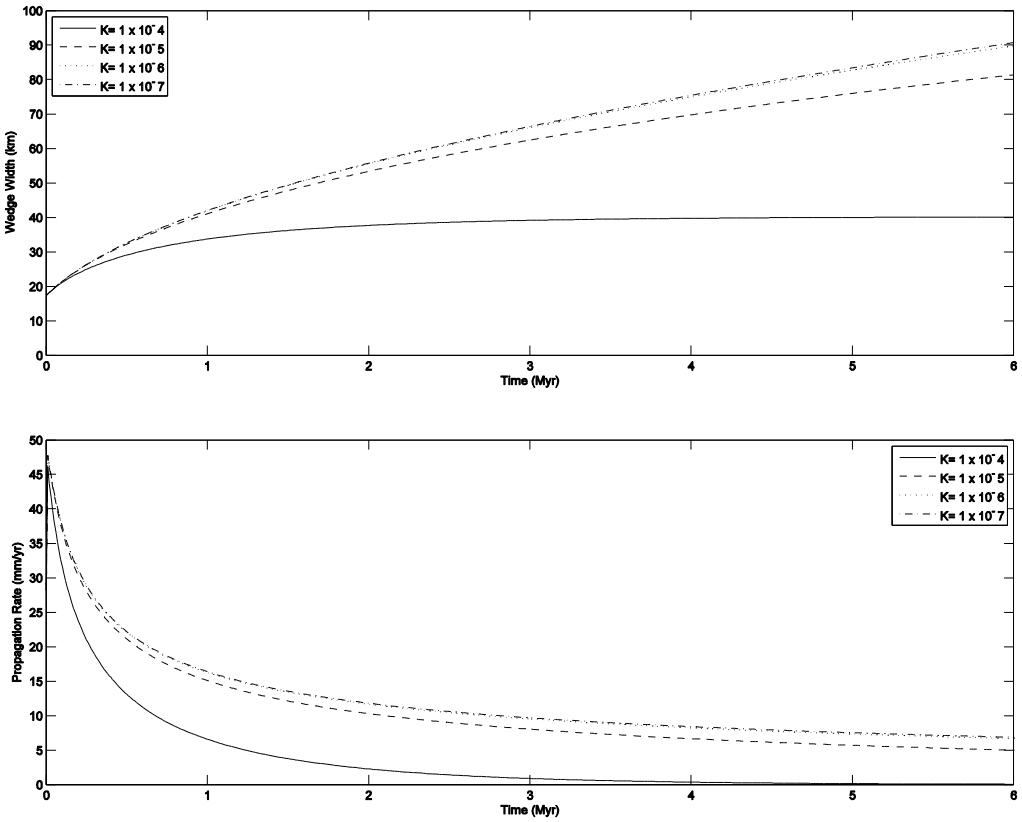

Figure A18 **Effect of varying sediment thickness (*T*) on wedge width (A) and wedge propagation rate (B), *T* = 8000 m, *v* = 0.025 m/yr.**

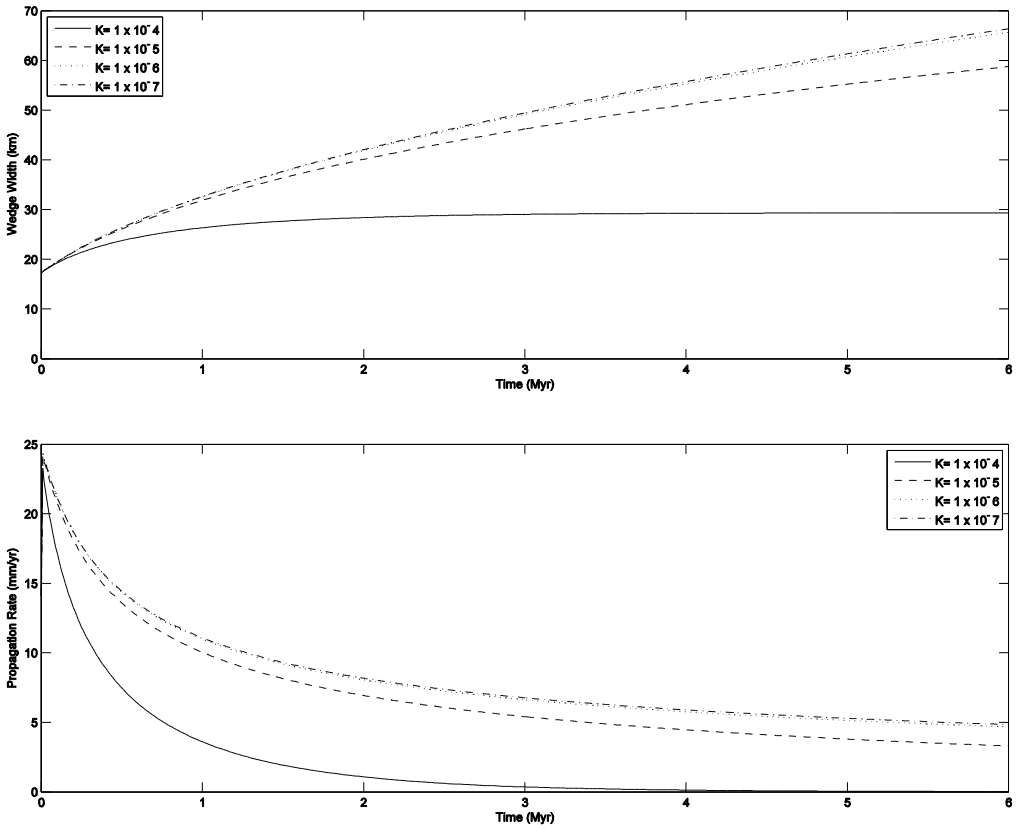

Figure A19**: Effect of varying sediment thickness (*T*) on wedge width (A) and wedge propagation rate (B), *T* = 8000 m, *v* = 0.0125 m/yr.**

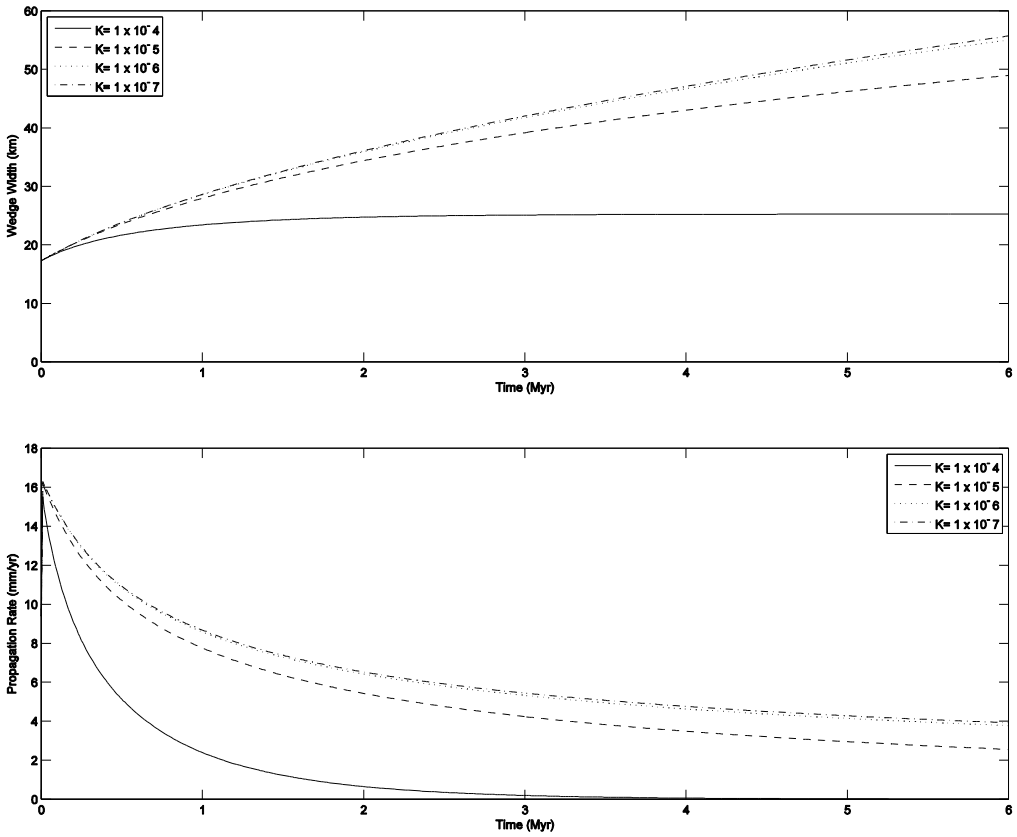

Figure A20: **Effect of varying sediment thickness (*T*) on wedge width (A) and wedge propagation rate (B), *T* = 8000 m, *v* = 0.0083 m/yr.**

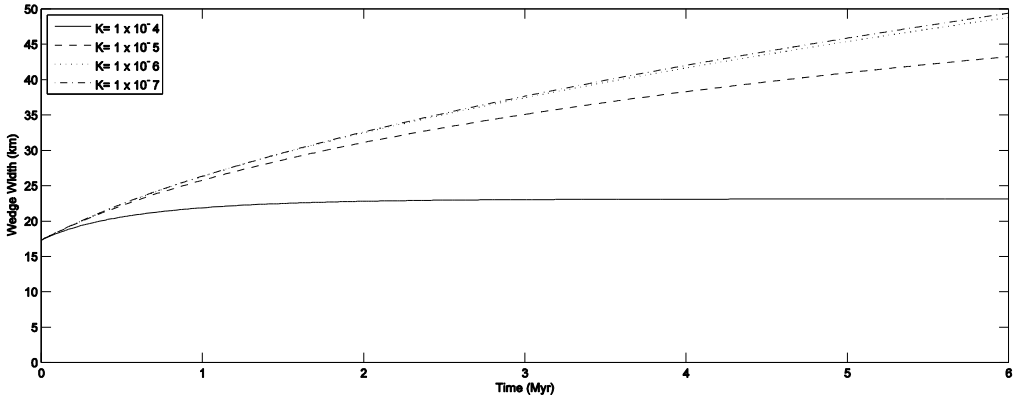

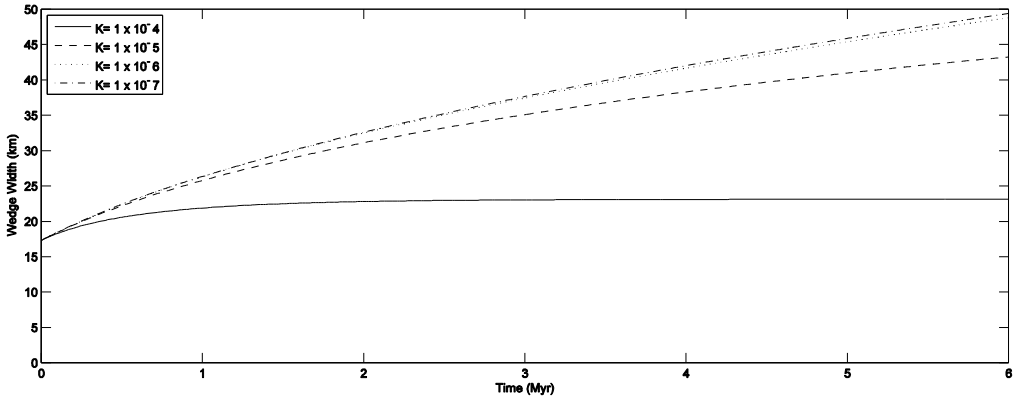

Figure A21: **Effect of varying sediment thickness (*T*) on wedge width (A) and wedge propagation rate (B), *T* = 8000 m, *v* = 0.00625 m/yr.**

Variation in Accretion Flux (vT)

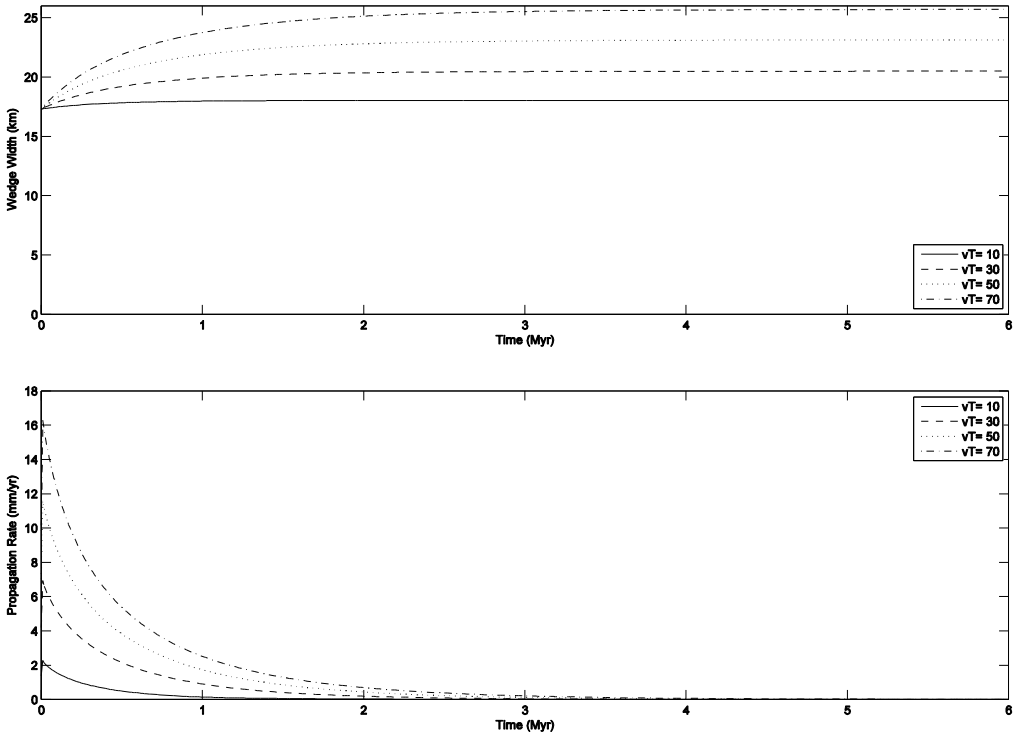

Figure A.22: **Effects of varying accretion flux (*vT*) on wedge width (A) and wedge propagation rate (B), *K* = 1.0×10^{-4}.**

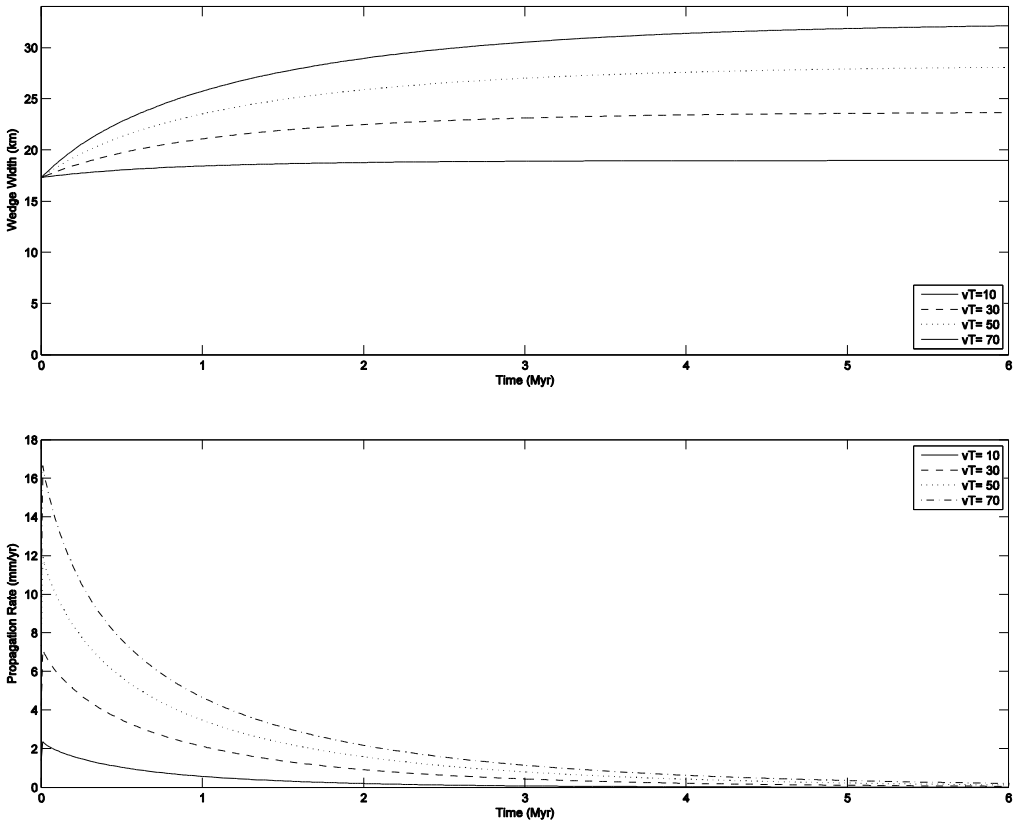

Figure A23: **Effects of varying accretion flux (*vT*) on wedge width (A) and wedge propagation rate (B), $K = 5\times10^{-5}$.**

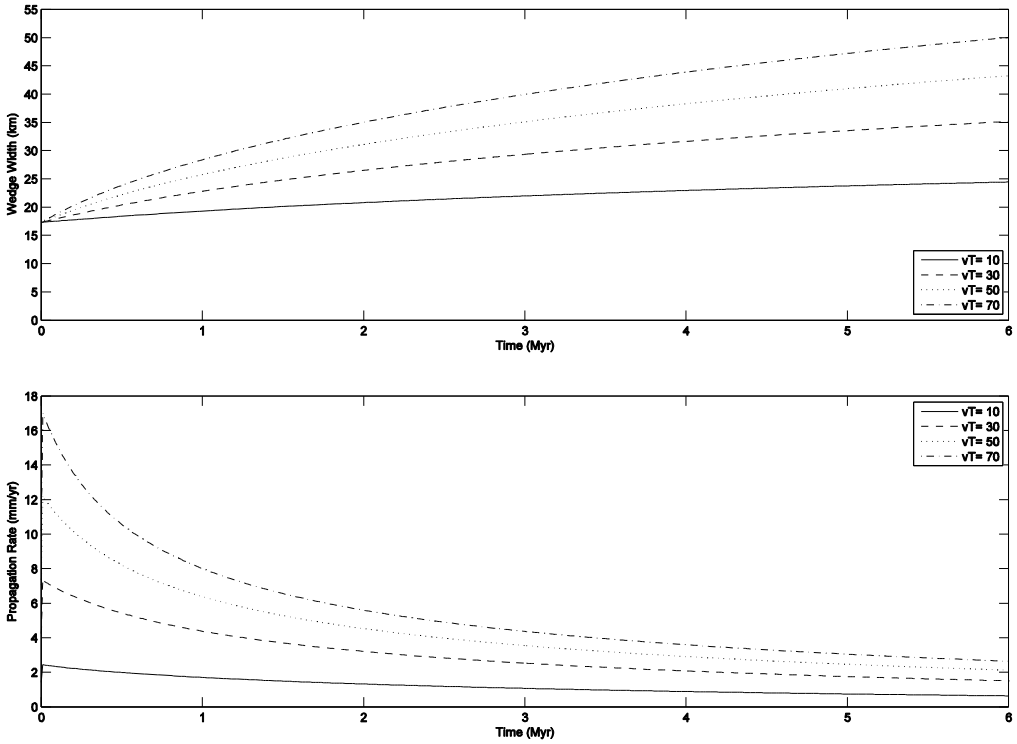

Figure A24: **Effects of varying accretion flux (*vT*) on wedge width (A) and wedge propagation rate (B), $K = 1.0\times10^{-6}$.**

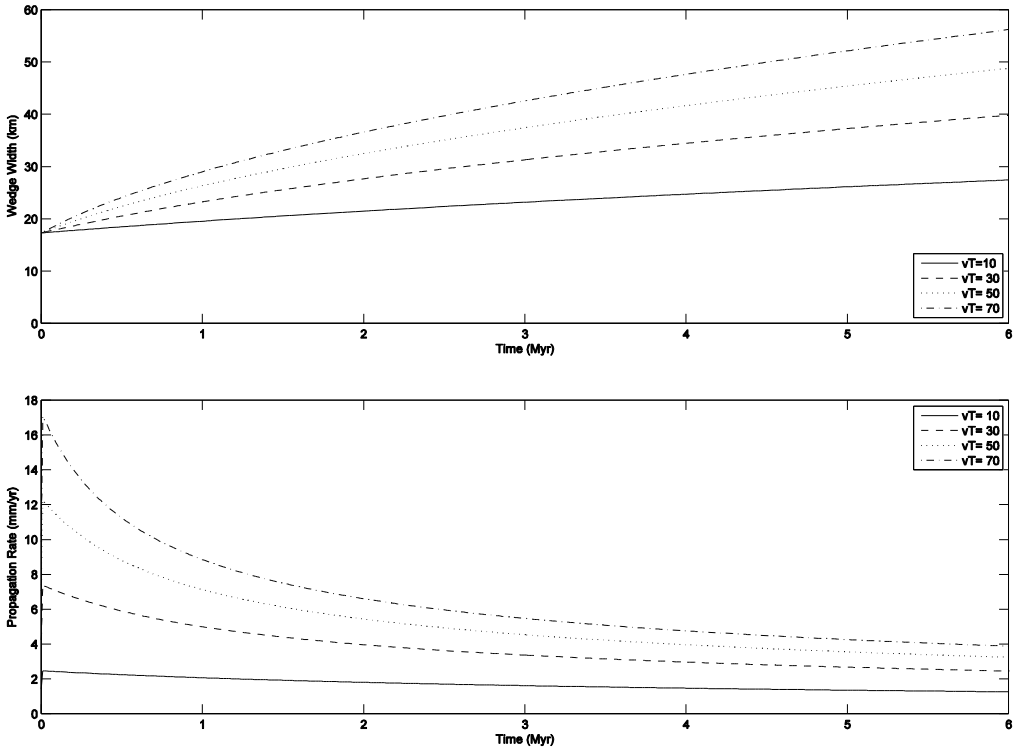

Figure A25: **Effects of varying accretion flux (*vT*) on wedge width (A) and wedge propagation rate (B), $K = 1.0\times10^{-6}$.**

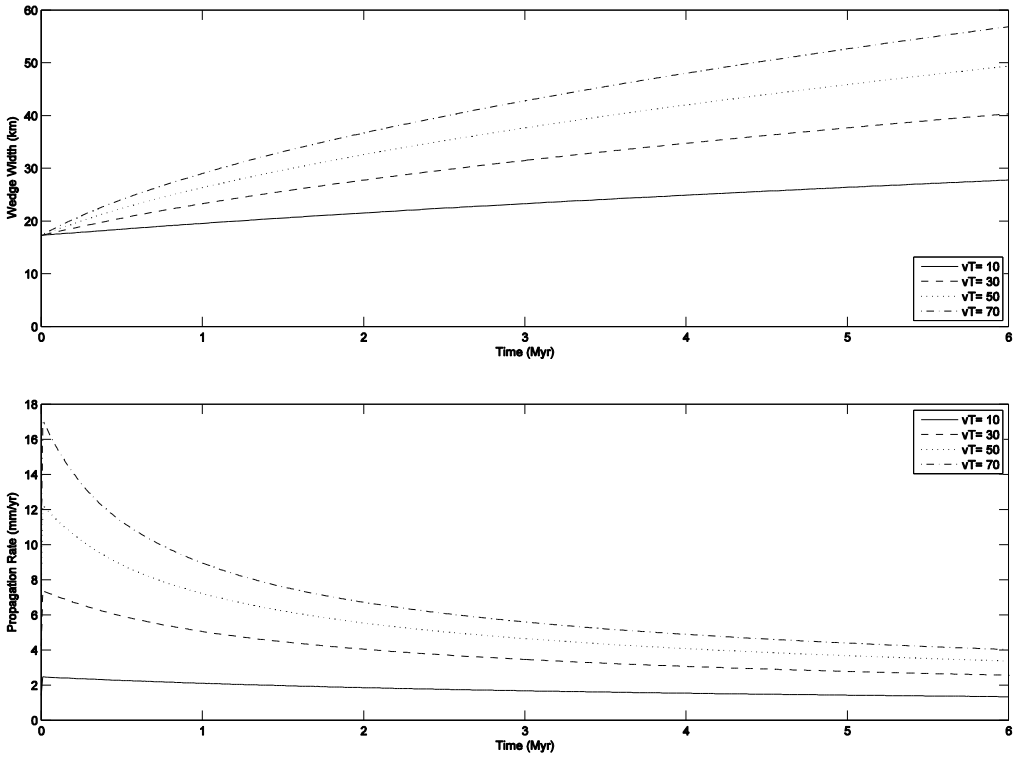

Figure A26: **Effects of varying accretion flux (*vT*) on wedge width (A) and wedge propagation rate (B), $K = 1.0\times10^{-7}$.**

Appendix B: Experiments for ka = 9.4, h = 1.65

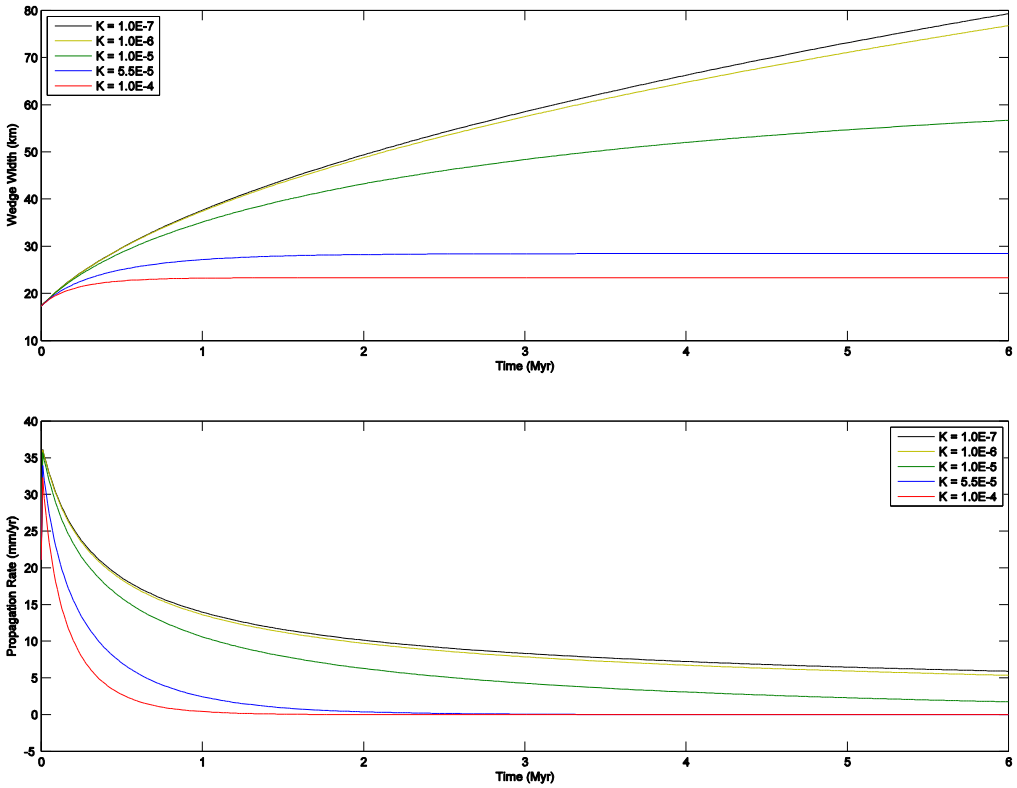

Figure B1: **Effects of varying K on wedge width (A) and wedge propagation rate (B), D = 8000 m, T = 6000 m, v = 0.025 m/yr.**

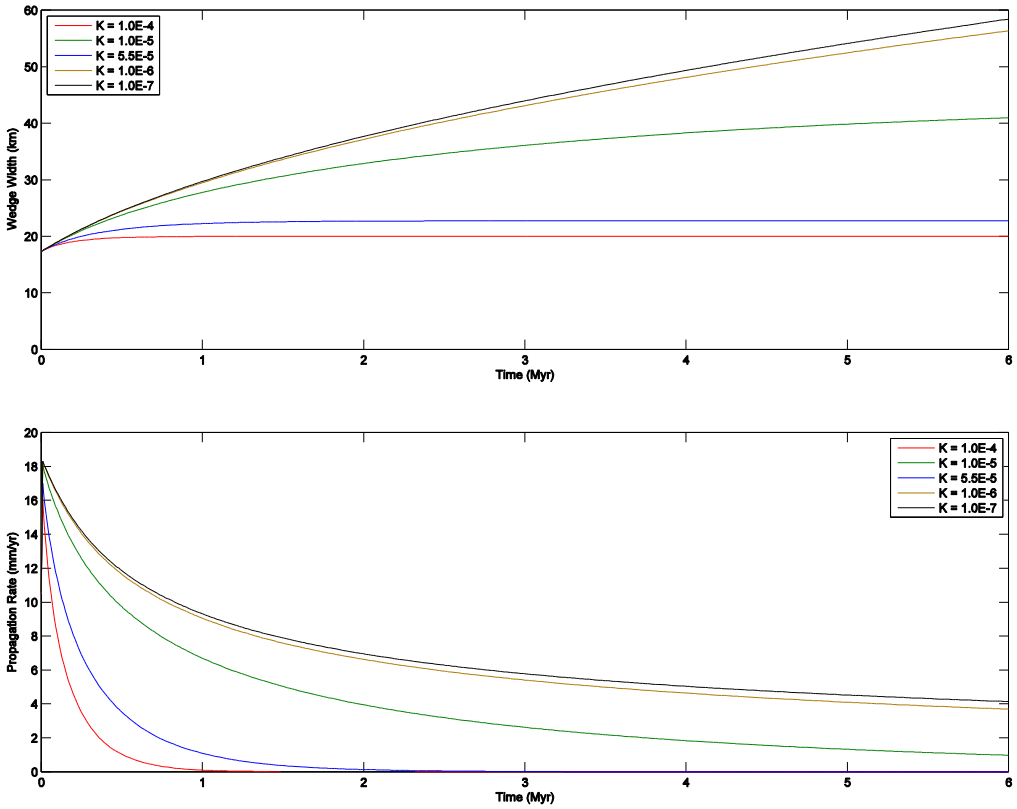

Figure B2: **Effects of varying K on wedge width (A) and wedge propagation rate (B), D = 8000 m, T = 6000 m, v = 0.0125 m/yr.**

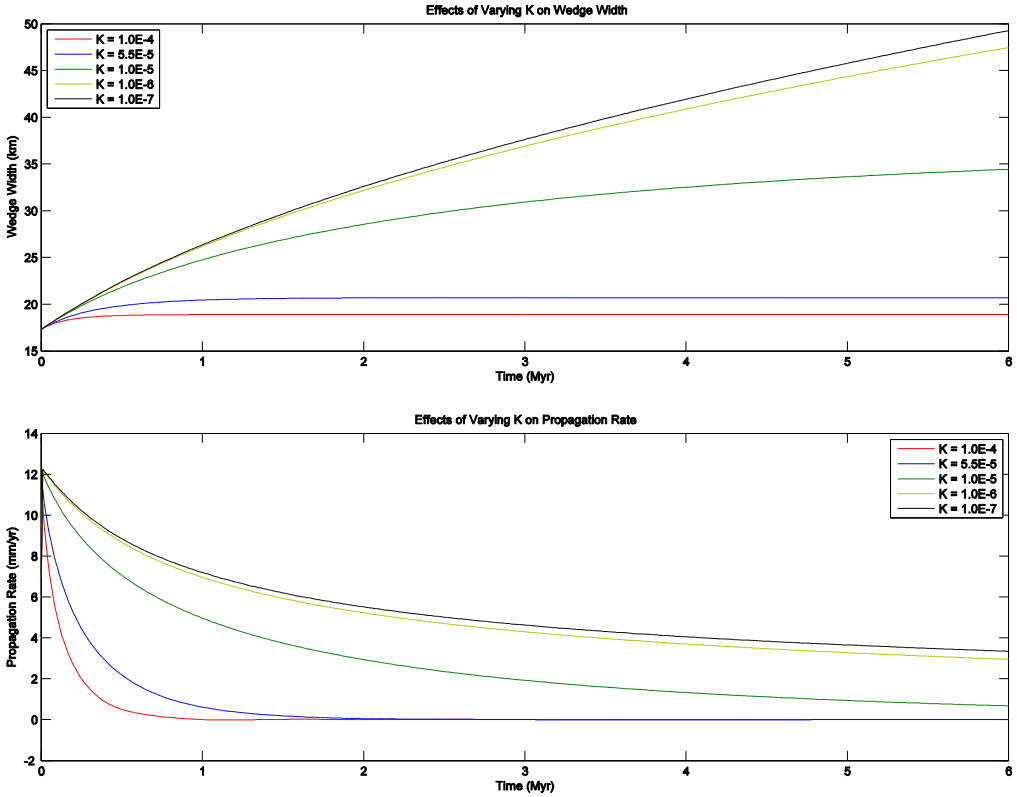

Figure B3: **Effects of varying K on wedge width (A) and wedge propagation rate (B), D = 8000 m, T = 6000 m, v = 0.0083 m/yr.**

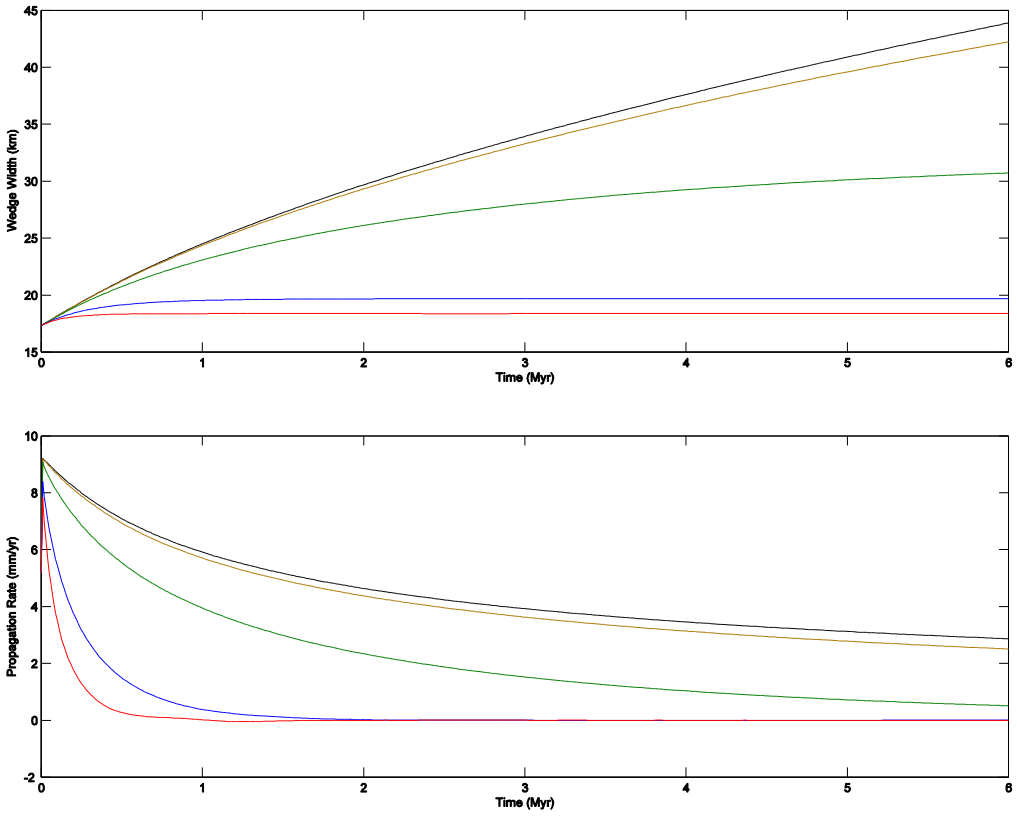

Figure B4: **Effects of varying K on wedge width (A) and wedge propagation rate (B), D = 8000 m, T = 6000 m, v = 0.00625 m/yr.**

Appendix C: Experiments for Calculating vT/K

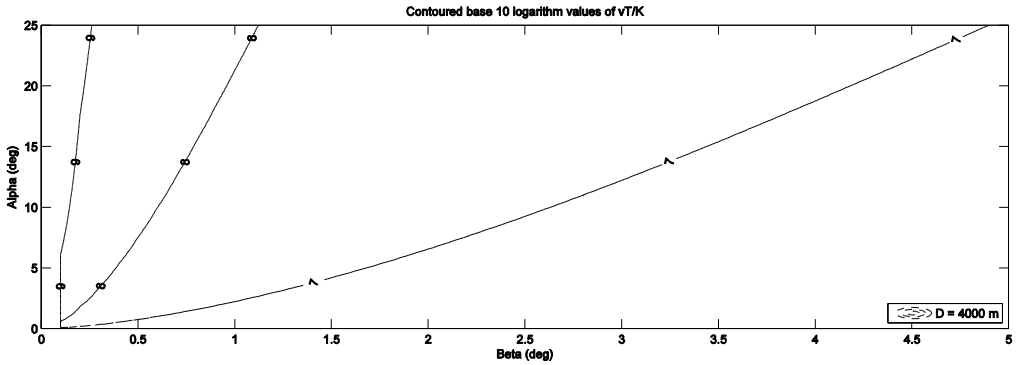

Figure C1: ***vT/K* contours for *D* = 4000 m, k_a = 4, *h* = 1.4**

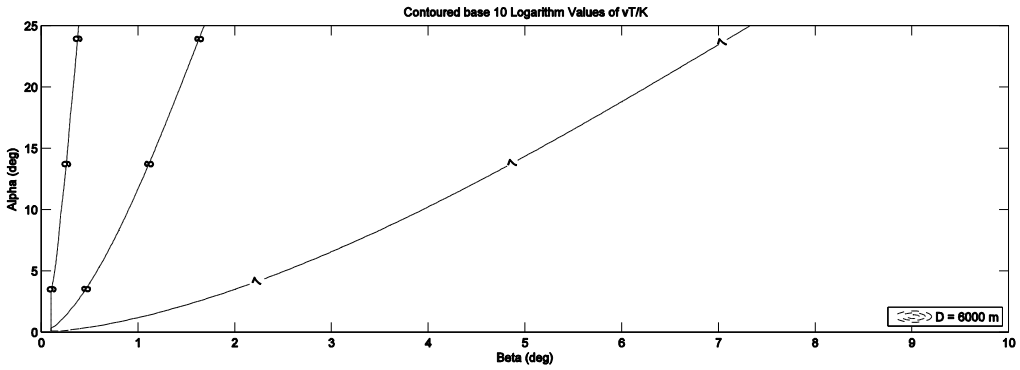

Figure C2: ***vT/K* contours for *D* = 6000 m, k_a = 4, *h* = 1.4**

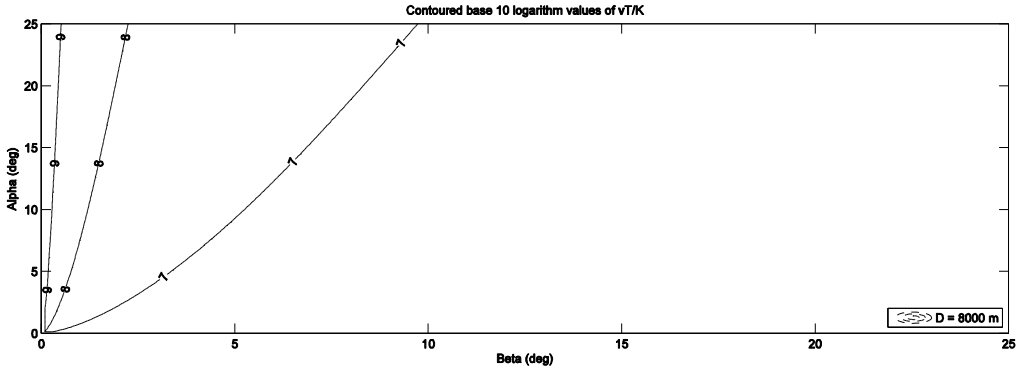

Figure C3: ***vT/K* contours for *D* = 8000 m, k_a = 4, *h* = 1.4**

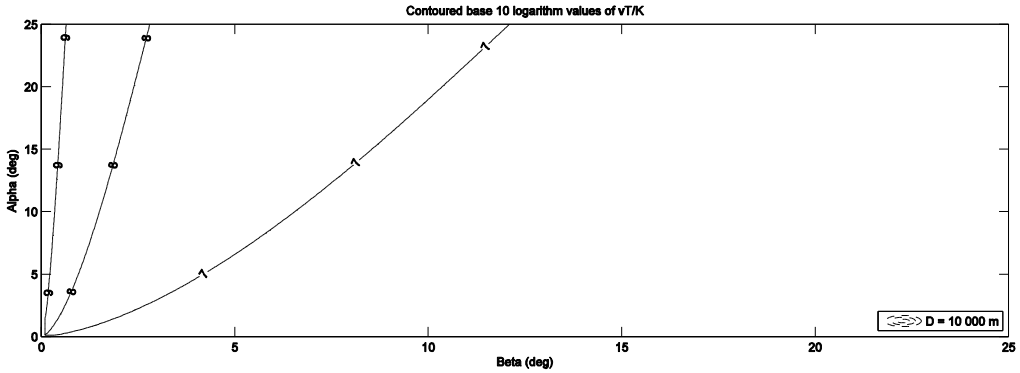

Figure C4: ***vT/K* contours for *D* = 10000 m, k_a = 4, *h* = 1.4**

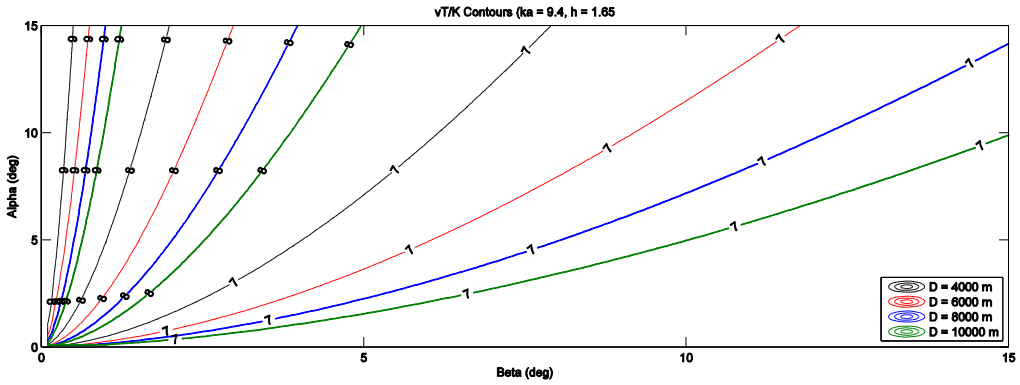

Figure C5: ***vT/K* contours, D = 6000 m, k_a = 9.4, h = 1.65**